Simulations of the collapse dynamics of a single polymer chain: Influence of hydrodynamic interactions, quench depth and chain sequence

A THESIS
SUBMITTED FOR THE DEGREE OF DOCTOR OF PHILOSOPHY

by
Tri Thanh Pham

Department of Chemical Engineering
Monash University
Clayton, Australia

June 9, 2009

This thesis, contains no material which has been accepted for the award of any other degree or diploma in any university or other institution. I affirm that, to the best of my knowledge, the thesis contains no material previously published or written by another person, except where due reference is made in the text of the thesis.

Tri Thanh Pham

To my family, and my grandparents

Acknowledgements

First of all, I would like to thank my undergraduate research supervisor Dr. Gerald G. Pereira for introducing me to the world of polymer science. Without Gerald, I would not have continued my further study into this fascinating field.

The work presented in this thesis was carried out under the direct supervision of Dr. J. Ravi Prakash. I express my sincere gratitude to Ravi for his guidance and constant encouragement during the last four years. I have also benefited greatly from his extreme precaution in aiming at only accurate and high quality work. I thank him further for his guidance in writing this thesis.

My limited understanding of the area of dilute polymer solutions would not have been further enhanced without the extra guidance through detailed course materials and helpful suggestions from Prof. Burkhard Dünweg at the Max Planck Institute for Polymer Research. I shall forever owe Burkhard a debt of gratitude for sharing his deep knowledge and insight in the area of soft matter physics. I further thank Burkhard for his warm hospitality, which certainly made my stay at the Max Planck Institute much more productive and enjoyable.

I would like to thank all the former and current members of the molecular rheology group at Monash, specially Sunthar, Prabhakar, Sudip Pattanayek, Jaroslaw Bosko and Mohit Bajaj for many stimulating technical discussions. It is a pleasure to thank my colleagues Pradipto Bhattacharjee, Xiangnan Ye, Duc At Nguyen, Mohini Acharya, Debadi Chakraborty, Nipen Shah, Jenny Ho, Michelle Yoo, Saptarshi Kar and Kamlesh Patel for all the fun that made my PhD life less stressful. I would like to thank the theory group at the Max Planck Institute for Polymer Research for their help in making my stay at the Institute a life time experience. I thank particularly Ulf D. Schiller for his help in using the lattice Boltzmann code. I would also like to thank two of my childhood friends Minh and Hoc for their support and encouragement throughout my Ph.D.

I am grateful to the staff in the Department of Chemical Engineering, in particular Lilyanne Price, Jill Crisfield, Garry Thunder, Judy Lawlor, Terri Wall, Wren Schoppe and Kate Malcolm for their help and advice on administrative matters, and Roy Harrip for his help in various technical issues. I am also thankful to the staff members, especially Doris Kirsch at the Max Planck Institute for Polymer Research for their help during my stay.

My work would not have been possible without the scholarships from the Department of Chemical Engineering at Monash University. I would like to thank the International Max Planck Research School for providing me a scholarship for my visit to the Max Planck Institute in Mainz, Germany. Travel grants provided by the MRGS and the Max Planck Institute also enabled me to present my work at conferences in Italy and Sweden.

I would like to thank the Australian Partnership for Advanced Computing (APAC) (Canberra, Australia), Victorian Partnership for Advanced Computing (VPAC) (Melbourne, Australia) and the Monash Sun Grid Cluster for the allocation of computing time on their supercomputing facilities.

Abstract

The central aim of this thesis is to examine the collapse dynamics of a polymer chain in a poor solvent, using the technique of Brownian dynamics (BD) simulations. Motivated by the protein folding problem, BD simulations of a nonlinear bead-spring chain model incorporating implicit fluctuating hydrodynamic interactions (HI) are used to investigate the role of the solvent in mediating the dynamics of the collapse of a single polymer chain, when the solvent quality is suddenly quenched from good to poor. Effects of HI, which has been found to play a key role in assisting the collapse, are incorporated via the Rotne-Prager-Yamakawa tensor.

In addition to this principal goal, this thesis also examines two aspects of the BD simulations technique itself. The first is an examination of the accuracy of using a bead-spring chain model for a polymer versus the use of a bead-rod model in the simulations. The second aspect is the comparison of the BD simulation technique with another recently introduced and popular mesoscopic simulation technique, namely, the lattice Boltzmann (LB) method. Each of these evaluations of the BD method are carried out in a variety of contexts, such as the static and dynamic properties of equilibrium polymer solutions, and their rheological behaviour in far from equilibrium viscometric flows. Given the diverse nature of the problems examined here, a summary of the principal results in each case is given separately under each of the headings below:

1. *Comparison of bead-spring and bead-rod chains*:

In general, the bead-rod model is assumed to be the most accurate representation for describing the actual dynamics of polymer molecules. The number of Kuhn steps N_k in this model is an experimentally measured quantity and fixed for a given polymer. On the other hand, predictions of bead-spring models are strong functions of the number of beads N. In almost all studies in the literature, N has been chosen arbitrarily to fit experimental results. As justification for using the coarse-grained

bead-spring chain model in this work to study the collapse transition of a single polymer chain, we show that predictions obtained from BD simulations of a bead-rod model can be reproduced from BD simulations of a bead-spring chain model using the recently developed successive fine graining (SFG) scheme [R. Prabhakar, J. R. Prakash, and T. Sridhar, J. Rheol., 48, 1251-1278, 2004]. In the SFG scheme, results of bead-spring chain simulations are extrapolated to the limit where the number of springs (N_s) approaches the number of rods (equal to the number of Kuhn steps, N_k) in a bead-rod model. It is found that in the absence of excluded volume (EV) and HI, the analytical results for linear viscoelastic properties obtained using the bead-spring model with the SFG scheme are in complete agreement with the infinitely stiff Fraenkel spring results. The numerical computations of linear viscoelastic properties in the presence of HI are found to be in good agreement with the results of the bead-rod model. In shear flow, the SFG results show excellent agreement with bead-rod results for a range of shear rates both in the absence and presence of HI and EV. In the limit $N_\mathrm{s} \to N_\mathrm{k}$, the numerical and analytical results obtained using the SFG scheme are found to be independent of the choice of spring force law.

2. *Comparative evaluation of the BD and LB methods*:

Since HI plays a key role in all of our simulations, an important question to address is which is the most efficient mesoscopic simulation technique to capture the effects of HI in a dilute solution. An important and popular new technique is the LB method. In this segment of the thesis, the difference between using an implicit solvent model (BD) versus an explicit solvent model (LB) is evaluated by comparing their predictions of static and dynamic properties of dilute polymer solutions. The LB method used here is the recently established hybrid algorithm based upon dissipative coupling between Molecular Dynamics and lattice Boltzmann (LB) introduced by Ahlrichs and Dünweg [P. Ahlrichs and B. Dünweg, J. Chem. Phys., 111, 8225, 1999]. Applying these methods to the same physical system (a single polymer chain in a good solvent in thermal equilibrium) allows us to draw a detailed and quantitative comparison in terms of both accuracy and efficiency. It is found that the static conformations of the LB model are distorted when the box length L is too small compared to the chain size. Furthermore, some dynamic properties of the LB model are subject to an L^{-1} finite size effect, while the BD model directly reproduces the asymptotic $L \to \infty$ behavior. Apart from these finite size effects, it is also found that in order to obtain the correct dynamic properties for the LB simulations, it is crucial to properly thermalize all the kinetic modes. It is only then that these results are in excellent agreement with each other, as expected. Moreover, Brownian Dynamics is found to be much more computationally efficient than lattice Boltzmann as long as the degree of polymerization is not excessively large.

3. *Collapse dynamics of a homopolymer*:

Having established that BD simulations of a bead-spring chain model is probably the most efficient mesoscopic method for studying the collapse problem, simulations have been carried out to study the collapse dynamics of a single polymer chain in a poor solvent. Our simulations suggest that homopolymer collapse takes place via a three-stage mechanism, namely, formation of pearls, coarsening of pearls and the formation of a compact globule. The collapse pathways from a good solvent state to a poor solvent state are found to be independent of hydrodynamic interactions (HI). On the other hand, HI is found to significantly speed up the collapse rate. At large quench depth (the depth of the Lennard Jones potential), independent of the presence of HI, polymer molecules are found to be trapped in metastable states for long periods before acquiring their native globular state. The exponents characterizing the decay of various properties such as the radius of gyration are determined and compared with the values reported in the literature.

4. *Collapse dynamics of a copolymer*:

Although the homopolymer model has been widely used as a prototype to understand the protein folding problem, this model cannot capture all the complex behaviour seen in a protein. For instance, an important example of a missing detail in a homopolymer model is the formation of hydrophobic residues (H) or amino acids in the core and polar residues (P) on the outer surface of a collapsed globule. As an improvement of a homopolymer model, we have used a two-letter code HP model with equal population of H and P type residues to represent a protein chain, i.e, a HP copolymer. Due to the diverse range of chain sequences that a copolymer can have, many interesting behaviours are revealed in the collapse dynamics of copolymers. The presence of HI significantly speeds up the collapse process of all copolymer sequences. It is found that the chain sequence has a strong influence on the kinetics of copolymer collapse as well as on the compactness and energy of its final collapsed state. Our simulations suggest that copolymer collapse takes place via at least two, sometime three stages of collapse in which a rapid formation of clusters is followed by cluster coalescence with the clusters finally rearranging themselves into a compact state. The chain total collapse time is mainly governed by the rate of collapse of the second stage known as the “cluster aggregation” stage, and the rate of collapse of this stage depends on the block size of P type monomers. Furthermore, our results also indicate that the presence of P type monomers in the chain prevents it from being trapped in local wells, i.e., it appears to smooth out the energy landscape for the folding process of copolymers. This in turn pushes the value of quench depth where trapping occurs to a much higher value than that for a homopolymer. It is also found that any chain sequence which consists of short block lengths of P type monomers collapses much faster than chain sequences with long P block lengths.

5. *A polymer chain in a poor solvent subjected to extensional flow*:

When a homopolymer in a poor solvent is subjected to extensional flow, our simulations show that the nondimensional strain rate at which a coil-stretch transition occurs is delayed to a much later extension rate compared to that of a homopolymer in a theta or in a good solvent. Furthermore, it was found that the coil-stretch hysteresis window for a homopolymer in poor solvent is much wider compared to that for a theta or a good solvent. Indeed, the width of the hysteresis window is increased by at least an order of magnitude or more. It is observed that the width of the hysteresis window reduces with increasing solvent quality from poor to good. The simulations results for a diblock copolymer which is composed of one block of P monomers and another block of H monomers subjected to extensional flow shows a dual coil-stretch hysteresis window. Interestingly, it is found that below a critical extensional rate, while the P block has completely gone into a stretched state, the H block still remains in a coiled state. It is only when the extension rate is increased beyond this critical extension rate that the H block starts to unravel, leading to a coil-stretch transition. If the interaction potentials for the two blocks in a copolymer chain are sufficiently different to each other, then one could see a dual coil-stretch hysteresis window. However, if the two potentials are not significantly different, then an overlapping hysteresis window is observed.

Contents

List of Tables

List of Figures

Chapter 1

Introduction

The complexity of protein self-assembly into well-ordered 3-D structures has been a fascinating problem and it has attracted a significant number of researchers world wide. Proteins are polypeptide chains made of twenty different amino acids or residues. During the folding process, a protein molecule has to go through a rugged energy landscape, hoping from one transition state to another while overcoming the free energy barriers along the way. The state of a protein is primarily controlled by the solvent condition that it is subjected to and this condition may be tuned by varying the temperature or by changing the concentration of osmolytes or chemical denaturants in solution [13]. Despite numerous efforts that have been made to understand this folding problem over the past few decades, it still remains one of the challenging unsolved problems in molecular biology [41]. The groundwork for understanding the kinetics of protein folding was laid in the early 1960s when the famous experiment performed by Anfinsen and co-workers [11; 12] first showed that proteins can fold repeatedly and quickly into a unique compact native structure from any denatured state. This result suggests that the native structures of some small globular proteins are thermodynamically stable states, with conformations at a global minimum in the free energy, which are kinetically accessible. However, in the late 1960s, Levinthal argued (later known as ‘Levinthal paradox’) that there were too many possible conformations for proteins to find the native structure in the vast amount of conformational space by random searching, while the biological folding times of a typical protein sequence is in milliseconds to seconds. He suggested that instead, proteins must fold by specific ‘folding pathways’ [47; 124; 210; 217].

Levinthal’s paradox suggests that the protein folding problem can be broken down into two goals - achieving thermodynamic stability and kinetic accessibility. Thermodynamic stability requires that a protein should reach its global minimum energy, and that the native structure should be determined only by the final native conditions and not by the initial denatured states (i.e. folding is pathway independent), but this might take a long time because it requires an extensive search. On the other hand, kinetic accessibility requires that the folding process must happen quickly. In such a situation, the kinetics may become pathway dependent, and as a result, the protein may end up reaching only local optima. The need to satisfy these two requirements has led to a search for folding pathways that avoid local minima and lead directly to the native state. Within this view, it appeared possible that the folding code (or foldable sequences) might be revealed from kinetics experiments if one could observe intermediate states along the folding pathways. This search led to the discovery of two different types of folding intermediates: the on-pathway [205] and the off-pathway [93] intermediates, with the implication that the folding code could only be revealed from the on-pathway intermediates as off-pathway intermediates lead to non-native states. However, this view on the existence of folding pathways is now not in favour due to new detailed observations seen in recent experiments and computer simulations [30; 32; 48; 60; 91; 95; 177; 189; 190].

Experiments on small well characterized fast-folding two-state proteins has shown that these proteins can fold quickly without the guidance of the intermediate states [60; 91; 95; 177; 189; 190]. The new experimental techniques have revealed a rich collection of information about folding kinetics that was not available previously [140]. Advances in experimental methods that give more detailed information at the atomic level and a new conceptual framework revealed from simplified statistical mechanical models has resulted in a ‘New View’ of the kinetics of protein folding [14; 15]. In this new view, the kinetic process of folding a protein can be described as rolling a ball down mountainsides of complex shape rather than water flowing through a single gully. Furthermore, each individual protein molecule follows its own trajectory, which is randomly directed by Brownian forces through the hills and valleys. Thus the new view emphasizes more on ensembles and multiple folding routes rather than specific structures and pathways [48].

The straightforward computational approach to tackle the protein folding problem would appear to be to take a natural amino acid sequence and perform atomistic molecular dynamic (MD) simulations on an exact or simplified model of a protein and hope that it converges to the native 3-D conformation. However, the native structure resulting from the simulations may not be a global or a pronounced local minimum because the simulation model would inevitably use approximate energetic interactions for the set of 20 different amino acids, while the true protein sequence could have been evolutionary designed to fold to its native structure with some ‘exact’ set of potentials [141]. Further, it cannot be guaranteed that any folding algorithm will converge to a native state, which can be distinguished by energy from many other such conformations. Moreover, it is quite difficult to obtain any reliable statistically accurate results from this method because of its large computational cost. Tanaka and Mattice [197] have pointed out that the intense computational cost of studying large-scale properties makes models accounting for atomistic details inappropriate even for short polypeptide chains because reliable results cannot be obtained due to poor statistics.

The computational limitations of models with detailed atomic structure has led to the frequent use of a more coarse grained statistical mechanics model such as the lattice chain model or the bead-spring chain model. Although these models neglect atomic detail, they still preserve the main microscopic ingredients of proteins including: chain connectivity, flexibility, excluded-volume, and sequence-dependent intrachain interactions [30; 32]. Further, the statistical models recognize that macroscopic ‘states’ such as the denatured state, intermediate state, and native state, are ensembles of individual chain conformations rather than specific and unique conformational states. These coarse-grained models have also been extensively used to study various phenomena in polymer solutions for quite some time. The rich variety of conformations which leads to many different intrinsic properties of polymer solutions has continuously drawn considerable interest in soft matter research. Coarse-grained computer modeling is increasingly being used as an integral part of theoretical study, in order to both test existing theories and to trigger the development of new concepts. Furthermore, coarse-grained computer simulations have also become an essential tool in materials research, especially for predicting and understanding the behavior of complex systems, where a complete theory is not available. It has been proven to be an effective and inexpensive way to study these systems.

Even with these simple statistical models, one obtains a great deal of information about the physical processes that trigger the folding of proteins and the effects of physical variables on the kinetics as well as the thermodynamics of folding. The simplest model for protein folding takes into account only two states, the denatured state and the folded state. Many small proteins have been shown to obey this minimal model [94]. Other attempts to try to understand the kinetics of protein folding have often employed a very simple statistical mechanical model, such as a linear chain composed of the same type of beads (known as a ‘homopolymer’) to represent a polypeptide chain, and to study its kinetics of folding or collapse. The conformational changes of this simplified chain are commonly referred to as polymer collapse because of the dramatic change in the size of the polymer molecule which decreases from a swollen state to its native globular state when the solvent conditions are changed from being a good solvent to a poor solvent. Understanding the dynamics of the conformational change of a single polymer, arising due to a change in the solvent quality has also been of interest in its own right for many years [25; 44; 45; 148]. It is believed that understanding the collapse transition of a homopolymer itself will enable us to obtain better insight into the conformational transitions in many complex biological systems, and to understand how other biomolecules such as DNA react to a change in their environment.

Since the folding process of globular proteins to their distinct compact native conformations mostly occurs in an environment surrounded by solvent molecules such as water, the solvent plays an important role in mediating the hydrodynamic interactions between moving residues or amino acids in analogy to hydrodynamic interactions in polymers [106; 215]. Hydrodynamic interactions (HI) is the long-range dynamic correlation between different segments of the chain due to the movement of other parts in the chain that are propagated through the solvent medium. While HI does not affect static properties, it seriously alters the dynamic properties of semidilute and dilute solutions. For instance, a recent study of the diffusion and folding of several model proteins by Frembgen-Kesner and Elcock [66] have shown that molecular simulations which neglect HI are incapable of reproducing the expected experimental translational and rotational diffusion coefficients of folded proteins, and only when HI is included do the predictions of the diffusion coefficients match very well with the expected experimental values. Study of small proteins folding has also revealed that inclusion of HI hastens the folding process by at least two fold [37; 66]. These studies have demonstrated the importance of HI in studying the kinetics of proteins folding.

As a result of numerous such studies in literature, the collapse transition from a coiled state to a globular state has been relatively well described for a homopolymer chain [45; 73; 127]. Although the equilibrium properties of the polymer solution in different solvent quality regimes, namely, good, theta (θ) and poor, are very well understood [44; 50], understanding the kinetics of the collapse is still an emerging field. The kinetics of homopolymer collapse, both in the absence and in the presence of HI has been studied via a variety of different theoretical approaches [2; 25; 45; 80; 104; 107; 114; 160] as well as numerical simulations [2; 26; 33; 103; 104; 123; 151; 162; 163; 164; 197]. A few important issues related to collapse kinetics are that, (i) the comparison of theory and experiments is still in its infancy, (ii) there is no common consensus on the effect of solvent mediated interactions on enhancing the collapse rate, and (iii) there is ambiguity with regards to the scaling laws for the various properties (for instance, the change in the radius of gyration with time as the polymer collapses).

Furthermore, although the homopolymer model has been widely used as a prototype to understand the protein folding problem, this model cannot capture all the complex behavior seen in a protein. For instance, an important example of a missing detail in a homopolymer model is the formation of hydrophobic residues (H) or amino acids in the core and polar residues (P) on the outer surface of a collapsed globule. Moreover, it is believed that the kinetic ability of natural proteins to fold is due to evolutionary selection of their sequence, but how information can be encoded in such a protein sequence is still a puzzle. Certainly, this question cannot be addressed from studying a simple homopolymer model. Beside the encodability of a protein native structure, the degeneracy of a protein sequence is also important because of its unique native structure. This means that the sequences of globular proteins must have very low degeneracies (number of lowest-energy conformations) in general. However, the findings from the kinetics of homopolymer collapse do not provide any information about encodability and degeneracy. This is because the ability to encode structures requires a monomer alphabet containing at least two different types of interactions or letters. Thus the structure of a normal homopolymer without charge in a poor solvent is not encodable, and, it is more appropriate to use a multi-letter code model to study the kinetics of protein folding.

On the forefront of protein modeling using simplified statistical mechanical models with multi-letter codes, the 20-letter code model is probably the closest in representing the interactions between amino acids in a real protein chain, as exemplified by the energy matrices introduced by Miyazawa and Jernigan [141]. However, it has been shown that predictions obtained from some of these energy matrices are not physical and they are quite different to those seen in real proteins, for instance, the burial of charged residues as well as the formation of polar residues in the core for many native structures of designed sequences [1; 76; 77; 199]. Chan and Dill [32] have suggested that models with a 20-letter code are not necessarily better than codes with fewer letters because these models neglect certain important features existing in a real proteins (for instance, correlations among inter-residue interactions) and only focus on maximum compact conformations. Moreover, Go and co-workers have shown that sequences with less correlations are more stable and fold faster [71; 196]. It has also been observed that adding repulsive interactions prevents trapping in local minima [77; 188] and leads to more sequences folding uniquely and with more designable folds [32], which are the bottlenecks in many lattice folding models [27; 31; 183; 199].

For convenience as well as efficiency in numerical calculations, we choose to use a simple two-letter code to study the kinetics of the protein folding problem. Such models have been referred to as prototeins [81]. In this model, a chain is represented by a binary sequences of H (hydrophobic) and P (polar) monomers, and has been widely used in literature to study heteropolymers or copolymers. Although the HP model has been widely used to study the protein folding problem as well as heteropolymers in general, almost all the results are obtained from predictions on discrete lattice models. Only a very limited number of HP models have been investigated via continuous models [40]. Surprisingly, even with this simple HP approach in lattice models, certain features of protein folding can be observed. For example, the model predicts that only a small fraction of sequences fold uniquely and not all structures can be encoded [32; 122]. In addition, a folding sequence is most likely to have only a single native conformation [122].

Due to the astronomically large number of sequences and folding conformations that are possible for a chain composed of N beads with arbitrary combinations of H and P block sizes, it is inappropriate to investigate all these conformations and sequences because the computational cost is way beyond the limit of our patience and lifespan, especially for $N \geq 20$ chains [81; 122]. Thus one has to try to narrow down the search in order to obtain some useful information about the kinetics of folding. Since roughly half of the naturally occurring amino acids are hydrophobic

[211], it follows that on average a random protein sequence should have a ratio of $N_H/N \simeq 0.5$, where N_H is the number of hydrophobic monomers. The predicted results reported by Camacho and Thirumalai [28] suggest that the search for the foldable sequences should only focused on searching among a subclass of compact structures, especially those which have minimum energy because this criterion would salsify the low degeneracy requirement in a globular protein. In fact, their results indicate that the chain sequence should consist of half H type and half P type monomers because this ratio is not only very convenient to stabilize proteins in solution [47], but it is also close to the optimum ratio required to achieve the fewest number of minimum energy compact structures or minimum degeneracy. Although the kinetics of collapse of copolymers with such a ratio have also been reported in the literature [40; 102], it is still not known which features in a sequence of a copolymer chain directly affect its dynamics of folding and how exactly these features control the speed of folding as well as the compactness of the final equilibrium state. Further, it remains to be seen whether the order of collapse amongst the various copolymers is independent of chain length and HI.

As a starting point to study the protein folding problem, a Brownian dynamics simulation of bead-spring chains has been used to investigate the influence of implicit hydrodynamic interactions and quench depths on the dynamics of collapse as well as their effects on the kinetics pathways of a homopolymer chain. In addition, a bead-spring chain composed of 50% hydrophobic H type beads and 50% polar P type beads has been used to investigate the effect of chain sequence on copolymer collapse. In particular, the aim is to determine the effects of block length on the kinetics of folding and the compactness of the final collapsed state in the presence of HI (which are incorporated implicitly through the Rotne-Prager-Yamakawa (RPY) tensor), for three different types of copolymers. The identification of the exact features of a sequence that directly governs the chain's kinetics of collapse and its final equilibrium size will be attempted. The influence of HI on the dynamics of folding is investigated by comparing the values of various dynamic quantities for cases with and without HI. Further, effects of HI and chain length on the order of collapse amongst the various copolymers is also examined. To the best of my knowledge, the combined effects of HI and chain sequence on collapse kinetics within the framework of BD simulations has not been reported previously in the literature.

Although Brownian dynamics simulations of bead-spring chains has been used extensively to study various phenomenon in polymer solutions due to its low computational requirements, there are other issues for this model that have not been resolved. Firstly, the bead-spring model is not the most accurate coarse-grained description of a flexible polymer molecule of N_k Kuhn segments. There are no systematic ways of choosing the input parameters for the bead-spring chain models with $N_\mathrm{s} < N_\mathrm{k}$ springs to obtain predictions that match with experimental results [88; 90; 96; 120; 125; 126]. In this work, predictions from the Brownian dynamics simulations of a bead-spring chain model using the recently developed successive fine graining (SFG) scheme [166] are examined to see whether this model is capable of reproducing the widely accepted bead-rod results. Secondly, since HI has been shown to facilitate the folding process by speeding it up significantly [33; 37; 66; 103; 158], it is crucial to use a simulation technique that accurately and effectively captures the role of HI. However, it is still unclear which is the most efficient mesoscopic simulation technique to capture HI in a dilute solution. Further, the difference between using an implicit solvent model which includes fluctuating HI such as our BD model versus an explicit solvent model has not been solidly established in the literature. An important and popular new technique amongst explicit solvent models is the lattice Boltzmann (LB) method, which has been shown to be a promising candidate to replace the traditional computationally intensive MD simulations [7]. Detailed quantitative comparison on the predicted static and dynamic properties of dilute polymer solutions, in terms of both accuracy and efficiency, for both simulation techniques has been carried out for a system made up of a single polymer chain in a good solvent in thermal equilibrium. The LB method used here is the recently established hybrid algorithm based upon dissipative coupling between Molecular Dynamics (MD) and lattice Boltzmann (LB) introduced by Ahlrichs and Dünweg [7].

Apart from the collapse dynamics problem, the effects of solvent quality and chain sequence on the coil-stretch conformational hysteresis phenomena observed in polymer solutions when subjected to extensional flow is also of equal interest, especially in a poor solvent regime as these have not been reported in literature. Understanding single molecule conformations in a flow field is essential in order to effectively design and manufacture microfluidics and micro total analysis systems [49]. In 1974, using an approximate model, de Gennes [43] and Hinch [83] have independently shown that the coupling of flow field with the hydrodynamic drag for long-flexible polymer molecules in dilute solution could create kinetically frozen states, leading to a coil-stretch hysteresis. Since then, there has been a long debate about the validity of such hysteretic effects in bulk properties of dilute polymer solutions. However, researchers world wide have now conclusively confirmed the existence of this phenomenon with both experiments and numerical calculations [18; 68; 84; 89; 132; 179; 180; 191; 198]. Since the central aim of this thesis is to study the dynamics of collapse of homopolymers and various types of copolymers when the solvent quality is suddenly quenched from good to poor, we have obtained a wealth of information on the equilibrium configurations of these chains in both good and poor solvent conditions. These configurations can be used directly as the initially coiled chains for the hysteresis study in various solvent conditions. Thus, this thesis includes a study of the effects of solvent quality (or quench depth) and chain sequence on the conformational hysteresis window for the listed polymers.

This thesis is organized as follows. A brief description of the bead-spring chain model and the computer simulation methods used to study implicit and explicit solvent models are given in Chapter 2. This is followed by the validation of the successive fine graining scheme in Chapter 3. A detailed and quantitative comparison in terms of both accuracy and efficiency between the results predicted by the LB and the BD simulations are presented in Chapter 4. Chapter 5 discusses the effects of HI and quench depth on the dynamics of collapse and the kinetics pathways of a homopolymer, while the effects of chain sequence on the total collapse time and the compactness of the final collapsed state are explored in Chapter 6. Chapter 7 discusses the effects of solvent quality and chain sequence on the coil-stretch hysteresis window of a polymer chain subjected to extensional flow. The major conclusions of this work are finally summarized in Chapter 8.

Chapter 2

Molecular model and simulation methods

This chapter briefly describes the bead-spring chain model and the two simulations methods that have been used in this work to study static and dynamic properties of dilute polymer solutions, namely, the Brownian dynamics (BD) and the lattice Boltzmann (BD) methods. The set of governing equations for a bead-spring chain model with a non-linear spring force, and with hydrodynamic and excluded volume interactions incorporated, are presented for both methods.

Since inter- and intra-molecular interactions are ultimately responsible for the behavior of any material observed at macroscopic scales, one would expect that accurate prediction of properties of polymer solutions would require computer simulations of detailed molecular models of these systems. However, such detailed simulations are computationally very expensive to perform. In spite of their diversity due to the tremendous variety in polymer molecules and their solvents, the macroscopic properties of large classes of polymeric materials share common features, and appear to depend only on a small set of parameters. It has been found that the experimental data for different polymer-solvent systems can be collapsed on to universal master plots. In the words of Doi and Edwards [50], "the ability of such superposition indicates the existence of an inherent simplicity hidden behind the apparent complexity of the polymer systems". Since universal features of macroscopic behavior for different polymer systems within any single class of polymeric materials are the same, their universal properties must be independent of the details of polymer/solvent chemistry. Furthermore, the fact that master plots can be obtained by rescaling raw experimental data with a few well defined parameters means that all chemistry dependence has been absorbed into those parameters.

A recent review by Keunings [100] has described the number of levels of modeling of polymer solutions, such as quantum mechanics, atomistic modeling, kinetic theory and continuum mechanics, which can be used for their description. However, the chosen level of sophistication is primarily governed by its analytical tractability and computational efficiency. While the use of a quantum level description is out-of-question due to the requirements of excessive computational resources, atomistic modeling (molecular dynamics (MD) simulation) has been used to some extent to predict rheological properties in simple flows. However, the intense computational requirement makes such techniques inappropriate for large polymer systems. An alternative and efficient method to represent the fluid is the kinetic theory based fluid description, which is sufficient to accurately capture large-scale properties of many polymer systems.

For the representation of polymer chain itself, there are a number of ways in which a polymer can be represented within the framework of kinetic theory, based on coarse-grained micro-mechanical molecular models such as bead-rod, bead-spring, and dumbbell models. These models provides a good description of the polymer conformation (e.g., stretch and orientation), and they can incorporate important physics such as the finite extensibility of the polymer molecules and the presence of solvent mediated interactions such as hydrodynamic (HI) and excluded volume (EV) interactions between parts of the polymer chain. The incorporation of these effects is necessary to explain many experimentally observed features such as scaling laws, shear thinning and bounded extensional viscosity in homogeneous flows of dilute polymer solutions [21; 22; 51; 90; 112; 153; 165; 166; 168; 176; 218]. The inclusion of HI is also shown to be extremely important in explaining various experimentally observed dynamic scaling laws, and transport coefficients (e.g., diffusivity) [38; 44; 90; 108; 120; 121; 132; 152; 193; 195].

As has been pointed out in Chapter 1, the bead-rod model is assumed to be the most accurate representation for capturing the behavior of real polymer molecules in solution. However, its application to represent typical polymer molecules encountered in experiment is still beyond available computational resources. Although a dumbbell model is the simplest and most computationally efficient method to represent a polymer molecule, it does not accurately predict quantitative features and some qualitative features for the collapse dynamics problem such as the kinetic pathways and cluster formation because it does not have enough number of degrees of freedom. Thus a bead-spring model appears to be the most appropriate model to represent a polymer molecule due to its computational efficiency over the bead-rod model and its ability to accurately capture qualitative and quantitative behavior of a polymer system. Using kinetic theory, the probability density function describing the probability of finding a bead-spring chain with a given configuration can be obtained from the diffusion or Fokker-Plank equation, which is a partial differential equation. The solution to the Fokker-Plank equation is the probability density function, which can be used to evaluate macroscopic properties of interest such as the elastic stress. However, the Fokker-Plank equation is analytically intractable for non-linear bead-spring chains. Alternatively, BD simulations or stochastic simulations based on the Itô stochastic differential equation (SDE) which is equivalent to the Fokker-Plank equation, are widely used to solve for the configuration of bead-spring chains without even solving for the probability density function. Configurational averages can then be subsequently used to evaluate the elastic stress and other macroscopic properties.

2.1 Molecular model

For major parts in this work, a polymer molecule is represented by a conventional bead-spring chain model, which consists of N beads that are connected via $N-1$ finitely extensible nonlinear elastic (FENE) massless springs. The springs are chosen such that their force-extension behavior mimics the response of the polymer to an imposed extension at its ends. The Lennard-Jones potential, which acts between all monomers, is often used to model the excluded volume (EV) effect. The two potentials V_{Spr} and V_{EV} are given by the expressions

$$\begin{aligned} V_{\text{Spr}} &= -\frac{HQ_0^2}{2}\ln\left(1-\left(\frac{\mathbf{Q}_{\mu\nu}}{Q_0}\right)^2\right), && (2.1)\\ V_{\text{EV}} &= 4\epsilon_{\text{LJ}}\left(\frac{\sigma^{12}}{r_{\mu\nu}^{12}}-\frac{\sigma^6}{r_{\mu\nu}^6}+\frac{1}{4}\right), \quad r_{\mu\nu}\leq 2^{1/6}\sigma, && (2.2)\end{aligned}$$

where H is the Hookean spring constant (also referred to as FENE spring constant in some literature), Q_0 the maximum extension of a single spring, $\mathbf{Q}_{\mu\nu}$ and $r_{\mu\nu}$ are the connector vector and the distance from bead μ to bead ν, respectively. $\epsilon_{\rm LJ}$ and σ are the energy and length parameters of the Lennard-Jones potential, respectively.

As will be elaborated in subsequent chapters, in individual circumstance, we have used variations of the basic LJ potential and spring force law depending in the context in which they are employed.

2.2 Brownian dynamics (BD) simulations

The instantaneous configuration of a bead-spring chain is specified by the set of position vectors $\mathbf{r}_\mu$ $(\mu = 1, \dots N)$. The evolution of the configurational probability distribution $\Psi(\mathbf{r}_1, \dots, \mathbf{r}_N)$ is governed by the Fokker-Planck equation [22; 155], which in dimensionless form is given by

$$\frac{\partial \Psi}{\partial t^*} = -\sum_{\mu=1}^{N} \frac{\partial}{\partial \mathbf{r}^*_\mu} \cdot \left\{ \boldsymbol{\kappa}^* \cdot \mathbf{r}^*_\mu + \frac{1}{4} \sum_{\nu} \mathbf{D}_{\mu\nu} \cdot \left(\mathbf{F}^{\rm s}_{\nu}{}^{*} + \mathbf{F}^{\rm int^*}_{\nu} \right) \right\} \Psi + \frac{1}{4} \sum_{\mu,\nu=1}^{N} \frac{\partial}{\partial \mathbf{r}^*_\mu} \cdot \mathbf{D}_{\mu\nu} \cdot \frac{\partial}{\partial \mathbf{r}^*_\nu}, \tag{2.3}$$

where $l_H = \sqrt{k_{\rm B}T/H}$ and $\lambda_H = \zeta/4H$ are used as the length scale and time scale, respectively [165; 194]. $k_{\rm B}$ is Boltzmann's constant, T is the temperature, ζ ($\zeta = 6\pi\eta_{\rm s}d$, where $\eta_{\rm s}$ is the solvent viscosity) is the Stokes friction coefficient of a spherical bead of radius d, $t^* = t/\lambda_H$ is the dimensionless time. $\boldsymbol{\kappa}^*$ is a time-dependent, homogeneous, dimensionless velocity gradient. $\mathbf{D}_{\mu\nu}$ is the diffusion tensor representing the effect of the motion of a bead μ on another bead ν and is defined as $\mathbf{D}_{\mu\nu} = \delta_{\mu\nu}\boldsymbol{\delta} + \boldsymbol{\Omega}_{\mu\nu}$, where $\delta_{\mu\nu}$ is the Kronecker delta, $\boldsymbol{\delta}$ is the unit tensor and $\boldsymbol{\Omega}_{\mu\nu}$ is the hydrodynamic interaction tensor. $\mathbf{F}^{\rm s}_{\nu}{}^{*} = -\partial V_{\rm Spr}/\partial \mathbf{r}_\nu$ is the dimensionless spring force, $\mathbf{F}^{\rm int^*}_{\nu} = -\partial V_{\rm EV}/\partial \mathbf{r}_\nu$ is the dimensionless excluded-volume force.

Using polymer kinetic theory and stochastic calculus [22; 155], it can be shown that the time evolution of the configuration of the bead-spring chain is governed by the following dimensionless Itô stochastic differential equation:

$$d\mathbf{r}^*_\mu = \left\{ \boldsymbol{\kappa}^* \cdot \mathbf{r}^*_\mu + \frac{1}{4} \sum_{\nu} \mathbf{D}_{\mu\nu} \cdot \left(\mathbf{F}^{\rm s}_{\nu}{}^{*} + \mathbf{F}^{\rm int^*}_{\nu} \right) \right\} \Delta t^* + \frac{1}{\sqrt{2}} \sum_{\nu=1}^{N} \mathbf{B}_{\mu\nu} \cdot d\mathbf{W}_\nu, \tag{2.4}$$

where for all $\nu = 1, \dots, N$, $\mathbf{W}_\nu$ is a non-dimensional Wiener process and the components of $\mathbf{B}_{\mu\nu}$ are related to the HI tensor such that $\mathbf{D}_{\mu\nu} = \mathbf{B}_{\mu\nu} \cdot \mathbf{B}^{\rm T}_{\mu\nu}$ [155].

The regularized Rotne-Prager-Yamakawa (RPY) tensor is used in this work to incorporate hydrodynamic interactions [173; 213]. Note that the same HI tensor is used by Petera and Muthukumar [157] and Liu et al. [129] in their bead-rod model and Hsieh et al. [87] in the stiff FENE-Fraenkel spring model. The form of the dimensionless RPY tensor is:

$$\boldsymbol{\Omega}(\mathbf{r}^*) = \left[\Omega_1 \boldsymbol{\delta} + \Omega_2 \frac{\mathbf{r}^* \mathbf{r}^*}{r^{*2}}\right] \tag{2.5}$$

where for $r^* \geq 2\sqrt{\pi} h^*$

$$\Omega_1 = \frac{3\sqrt{\pi}}{4} \frac{h^*}{r^*} \left(1 + \frac{2\pi}{3} \frac{h^{*2}}{r^{*2}}\right); \quad \Omega_2 = \frac{3\sqrt{\pi}}{4} \frac{h^*}{r^*} \left(1 - \frac{2\pi}{3} \frac{h^{*2}}{r^{*2}}\right) \tag{2.6}$$

and for $0 < r^* \leq 2\sqrt{\pi} h^*$

$$\Omega_1 = 1 - \frac{9}{32} \frac{r^*}{h^* \sqrt{\pi}}; \quad \Omega_2 = \frac{3}{32} \frac{r^*}{h^* \sqrt{\pi}} \tag{2.7}$$

Here, h^* is the dimensionless bead radius in the bead-spring model and is defined as $h^* = a / l_H \sqrt{\pi}$.

When there is no flow field present, $\boldsymbol{\kappa}^* = 0$. In the presence of the flow field, the velocity gradient tensors for simple shear (SS) and uniaxial extensional (UA) flow, which are the flows of interest in this work, are given by

$$\boldsymbol{\kappa}^*_{\mathrm{SS}} = \dot{\gamma}^* \begin{pmatrix} 0 & 1 & 0 \\ 0 & 0 & 0 \\ 0 & 0 & 0 \end{pmatrix}, \qquad \boldsymbol{\kappa}^*_{\mathrm{UA}} = \dot{\epsilon}^* \begin{pmatrix} 1 & 0 & 0 \\ 0 & -\frac{1}{2} & 0 \\ 0 & 0 & -\frac{1}{2} \end{pmatrix} \tag{2.8}$$

where $\dot{\gamma}^* = \lambda_H \dot{\gamma}$ and $\dot{\epsilon}^* = \lambda_H \dot{\epsilon}$ are the dimensionless shear, and dimensionless extension rate, respectively. Further details of the model and simulations method can be found in Ref. 165.

The most computationally intensive part in performing BD simulations is to determine the matrix $\mathbf{B}_{\mu\nu}$ in Eq. (2.4) above. Generally, Cholesky decomposition of $\mathbf{D}_{\mu\nu}$ is used to obtain $\mathbf{B}_{\mu\nu}$ as an upper (or lower) triangular matrix and the computational cost for this method scales as N^3 [64]. Fixman made use of the fact that $\mathbf{B}_{\mu\nu}$ can be approximated as the square-root matrix of $\mathbf{D}_{\mu\nu}$, and noting that it is the vector $\mathbf{B}_{\mu\nu} \cdot \Delta \mathbf{W}_\nu$ that is required rather than the matrix $\mathbf{B}_{\mu\nu}$, applied Chebyshev polynomials to obtain $\mathbf{B}_{\mu\nu} \cdot \Delta\mathbf{W}_\nu$ with a lower computational cost, scaling roughly as $N^{2.25}$ [64].

The spatial configuration of the chain, $\mathbf{r}^*_\mu$ at any time t^* is obtained numerically by integrating Eq. (2.4) using a semi-implicit predictor-corrector scheme proposed by Prabhakar and Prakash [165]. The macroscopic properties of the solutions are obtained by simulating a large ensemble of independent trajectories.

2.3 The lattice Boltzmann (LB) method

In this method, the evolution of the LB variables n_i is governed by the following lattice Boltzmann equation [19; 192; Dünweg and Ladd]:

$$\begin{aligned} & n_i(\mathbf{r} + \mathbf{c}_i \Delta\tau, t + \Delta\tau) = n_i(\mathbf{r}, t) \\ + & \sum_{j=1}^{b} L_{ij} \left(n_j(\mathbf{r}, t) - n_j^{\mathrm{eq}}(\rho, \mathbf{u}) \right) + n'_i(\mathbf{r}, t). \end{aligned} \tag{2.9}$$

The variable $n_i(\mathbf{r}, t)$ is the (partial) fluid mass density at grid site $\mathbf{r}$ at time t, corresponding to the discrete velocity $\mathbf{c}_i$. $\Delta\tau$ is the time step, and the lattice spacing is denoted by a. The small set of velocities $\mathbf{c}_i$ ($i = 1, \ldots, b$, where the value of b depends on the details of the model) is chosen such that $\mathbf{c}_i \Delta\tau$ is a vector leading to the ith neighbor on the grid. L_{ij} is a collision operator for dissipation due to fluid particle collisions, such that the populations always relax toward the local pseudo-equilibrium distribution n_j^{eq} that depends on the local hydrodynamic variables $\rho = \sum_i n_i$ (the total mass density) and $\mathbf{u} = \sum_i n_i \mathbf{c}_i / \sum_i n_i$ (the local flow velocity). The collision process is constructed in such a way that it conserves both ρ and $\mathbf{u}$. $n'_i(\mathbf{r}, t)$ is the stochastic term, which is essential in order to simulate thermal fluctuations that drive Brownian motion.

The local pseudo-equilibrium distribution can be represented as a second-order expansion of the Maxwell-Boltzmann distribution, given by [192]

$$n_i^{\mathrm{eq}}(\rho, \mathbf{u}) = \rho w_{c_i} \left(1 + \frac{\mathbf{c}_i \cdot \mathbf{u}}{c_{\mathrm{s}}^2} + \frac{(\mathbf{c}_i \cdot \mathbf{u})^2}{2c_{\mathrm{s}}^4} - \frac{u^2}{2c_{\mathrm{s}}^2} \right), \tag{2.10}$$

where w_{c_i} are a set of weight factors, which depend on the sublattice i (i. e. the magnitude of $\mathbf{c}_i$) and $c_{\mathrm{s}} = \sqrt{1/3}(a/\Delta\tau)$ is the speed of sound. In this work, we have used the algorithm proposed in Ref. [7], however, with the modification that the original 18-velocity model (D3Q18) was replaced by the D3Q19 19-velocity model [192]. The set of $\mathbf{c}_i$ consists of the particle being at rest, the 6 nearest and 12 next-nearest neighbors on a simple cubic lattice. The magnitudes of the velocities corresponding to these three sets of particles are $c_i = |\mathbf{c}_i| = 0, a/\Delta\tau$, and $\sqrt{2}a/\Delta\tau$, respectively. The weight factors for the D3Q19 model are $w_0 = 1/3$, $w_1 = 1/18$ and $w_{\sqrt{2}} = 1/36$.

2.4 Conclusions

In this chapter the governing equations for the general molecular model and two simulation methods have been presented. The Brownian dynamics simulations method is the main simulations technique used in this thesis and it has been employed in all the following chapters: Chapter 3 to validate the successive fine graining scheme, Chapter 4 to compare BD predictions with LB results, Chapters 5 and 6 to study the dynamics of collapse of polymers, and Chapter 7 to explore the effects of solvent quality on the hysteresis window. The lattice Boltzmann simulation technique is only used in Chapter 4 to compare LB predictions with BD results.

Chapter 3

Validation of the successive fine graining (SFG) scheme

3.1 Introduction

The measurement and prediction of the properties of dilute polymer solutions has been of interest for decades. While polymer solutions used in commercial applications are mostly nondilute, dilute polymer solutions are frequently studied theoretically to understand the relationship between the dynamics of individual polymer molecules and the viscoelastic behavior of their solutions. The Brownian dynamics simulation (BDS) method with a coarse grained representation of linear polymer molecules has proved to be the most suitable method to theoretically predict the behavior of dilute polymer solutions. The most accurate coarse grained model proposed in the literature to model a flexible polymer molecule is the freely-jointed chain, in which a chain of beads is connected by freely-jointed links. This model is usually implemented in terms of the bead-rod model. However, a stiff Fraenkel spring between the beads has also been used to simulate freely-jointed chains. In the bead-rod model proposed by Kramers [110], a polymer molecule is modeled as a chains of beads connected by rigid links with a fixed length. The length of each link is equal to the Kuhn length (l). An alternative and computationally more efficient way of simulating polymer molecules is the bead-spring chain model, which is a coarse-grained version of the bead-rod model. In the bead-spring chain model, N beads are connected by entropic springs representing an ensemble of links (Kuhn steps) in the bead-rod model. The springs are chosen such that their force-extension behavior mimics the response of the polymer to an imposed extension at its ends. Both the bead-spring and bead-rod models have been used extensively in the literature and have been shown to be in quantitative agreement with experimental results [119; 186] when the essential physics such as the finite extensibility of the molecules and solvent mediated interactions such as excluded volume (EV) and hydrodynamic interactions (HI), are incorporated in the models [22; 90; 96; 119; 120; 166; 186; 194].

While the bead-rod model is assumed to be an accurate representation for describing the actual dynamics of polymer molecules, the computational efficiency of this model has largely restricted its use and development. The routine simulation of bead-rod chains is currently beyond the available computational resources particularly for long molecules with $N_\mathrm{k} \geq 10^3$. Larson [119] and Hsieh et al. [87] have pointed out that apart from computational requirements, there are other issues such as the equilibrium distribution function of the bead-rod model being different from the random walk distribution and the need for carefully addressing the proper treatment of constraints on fixed rod length etc. [22; 61; 110]. Different algorithms have been developed in the last decade to address these issues [9; 52; 61; 85; 87; 92; 110; 130; 142; 154]. Inclusion of HI and EV introduce further complexity and ambiguity in the bead-rod model formulation and implementation [4; 5; 131; 147; 154]. Predictions of rheological properties in shear and elongational flows from the bead-rod model with the inclusion of both EV and HI has also been reported recently by Muthukumar and coworkers [129; 157].

The complications introduced by the bead-rod model are particularly responsible for the development and frequent use of coarse-grained bead-spring chain models. While the number of Kuhn steps N_k in a bead rod model is an experimentally measured quantity and fixed for a given polymer, the use of a bead spring model introduces an additional parameter, N_s ($N_\mathrm{s} = N-1$). Although it is very well known that the predictions of bead spring models are strong functions of N, in almost all studies in the literature, the number of beads N has been chosen arbitrarily to fit experimental results [88; 90; 96; 120; 125; 126]. The exceptions are the recent work by Hsieh et al. [87], Prabhakar et al. [166] and Sunthar and Prakash [194]. While Hsieh et al. [87] introduced the use of stiff FENE-Fraenkel springs within the framework of the bead spring model, Prabhakar et al. [166] and Sunthar and Prakash [194] developed a scheme called *successive fine graining* (SFG). Both the use of stiff FENE-Fraenkel springs and SFG eliminates the arbitrariness of the number of beads.

The idea of stiff FENE-Fraenkel springs is based on the fact that the springs in the bead-spring model can be stiff enough to keep its length constant and thus behave like a rigid rod in the freely-jointed chain. The arbitrariness in the number of springs is eliminated by using as many springs as the number of rods in a bead-rod model. With the use of stiff FENE-Fraenkel springs, Hsieh et al. [87] were able to reproduce the viscosity data predicted by the bead-rod model using Liu's BDS algorithm [130] in simple shear flow and in the absence of HI. However, when HI was incorporated, a discrepancy was observed between their results and the results reported by Petera and Muthukumar [157], particulary for low values of non-dimensional shear rate. Although the use of the stiff FENE-Fraenkel spring is a promising method to compute freely-jointed chain results with the bead-spring model and hence, overcome various modeling complications associated with the bead-rod model, simulating large polymers ($N_{\mathrm{k}} \geq 10^3$) remains the major concern as the number of springs equals the number of rods. The work by Hsieh et al. [87] also raises an important question about the limiting behavior of conventional bead-spring chain models particularly in the presence of HI. It remains to be seen whether the results of the conventional bead spring chain model in the limit of $N_{\mathrm{s}} \rightarrow N_{\mathrm{k}}$ approaches the bead rod model results or results of the stiff FENE-Fraenkel spring model.

The SFG procedure eliminates the arbitrariness of the number of beads by accumulating results for various values of N where the force law is valid in a conventional bead-spring chain model and subsequently, extrapolating them to the limit $N_{\mathrm{s}} \rightarrow N_{\mathrm{k}}$. The central hypothesis of the SFG scheme is to keep certain static properties of the actual polymer molecule invariant, such as its end-to-end distance and contour length so that the same polymer molecule is represented at any level of fine graining. The strength of hydrodynamic interactions are also kept the same at the bead level. In the limit of extrapolation $N_{\mathrm{s}} \rightarrow N_{\mathrm{k}}$, the bead-spring chain with the SFG scheme would have the same static properties as well as it would feel the same drag force as that of the actual polymer molecule of N_{k} Kuhn segments. Since increasing values of N represent more fine-grained versions of the underlying chain, the procedure is called "successive fine graining". In contrast to the bead-rod and stiff FENE-Fraenkel spring models, the SFG is computationally efficient as $N_{\mathrm{S}} << N_{\mathrm{k}}$. Previous work has shown the predictions of SFG to be in excellent agreement with experimental data for dilute DNA and polystyrene solutions in extensional flow [166; 194]. Another interesting feature of SFG is the systematic treatment of hydrodynamic and excluded volume interactions which leads to parameter free predictions of experimental data [166; 194].

While the SFG procedure undoubtedly leads to an improved understanding of the choice of parameter values and increased computational efficiency specially for larger $N_{\rm k}$, there has been no direct verification so far of the SFG procedure by comparison with exact bead-rod results. The comparison of SFG results with bead-rod results can be useful in understanding the limiting behavior of the conventional bead-spring chain model. Before the SFG procedure is carried out, it is important to investigate the limit on the number of springs, beyond which SFG is no longer valid since spring force laws break down when the bead-spring chain is fine grained excessively [194; 206]. We denote the number of springs at which a particular spring force law breaks down by $N_{\rm c}$. Note that $N_{\rm c} < N_{\rm k}$. One might argue, for instance, that the bead-spring chain model is only valid for $N_{\rm s} < N_{\rm c}$, and legitimately, extrapolations should not be carried out beyond this value of $N_{\rm s}$. On the other hand, the value $N_{\rm k}$ is fundamentally built into the SFG procedure as the degree of flexibility of the underlying chain. So perhaps the extrapolation should be carried out to $N_{\rm k}$, i.e. $N_{\rm s} \to N_{\rm k}$. This subtle issue has not been resolved in the previous work by Prabhakar et al. [166] and Sunthar and Prakash [194]. This is partly because, for a large molecular weight polymer chain (i.e. large $N_{\rm k}$) simulated by Prabhakar et al. [166] and Sunthar and Prakash [194], it is not possible to distinguish the difference between the $N_{\rm k}$ and $N_{\rm c}$ limits due to the very small difference between $1/\sqrt{N_{\rm c}}$ and $1/\sqrt{N_{\rm k}}$ (the coordinates in which SFG extrapolation is carried out).

3.2 Models

In this work, three most commonly used spring force laws, namely, the finitely extensible nonlinear elastic (FENE) spring [209], the inverse Langevin chain (ILC) [39], and the wormlike chain (WLC) [134], are employed to account for the finite extensibility of the molecule. The use of three different finitely extensible spring (FES) force laws is based on the argument by Hsieh et al. [87] that the behavior of infinitely stiff springs is close to that of freely-jointed chains independent of the choice of spring force laws. As discussed by Prabhakar et al. [166], since successive fine graining leads to infinitely stiff springs (which represents the limit $b \to 0$), one anticipates that SFG results should be independent of the spring force law. The force laws used here can be represented in a general form consisting of a Hookean part and a nonlinear part f by

$$\mathbf{F}^{\mathrm{s}\,*}_{\nu}(\mathbf{Q}^*_{\nu}) = \mathbf{Q}^*_{\nu} f(Q^*/\sqrt{b}) \tag{3.1}$$

where $\mathbf{F}^*_{\nu}$ is the connecter force in the spring whose end-to-end vector is specified by the connector vector $\mathbf{Q}^*_{\nu} = \mathbf{r}^*_{\nu+1} - \mathbf{r}^*_{\nu}$. Q^* is the dimensionless length of the spring and $\sqrt{b} = Q_0/l_H$ is the dimensionless maximum stretchable length of a single spring. The non-Hookean part $f(Q^*/\sqrt{b})$ for various spring forces is

$$f_{\mathrm{FENE}} = \frac{1}{1-q^2}; \quad f_{\mathrm{ILC}} = \frac{3-q^2}{3(1-q^2)}; \quad f_{\mathrm{WLC}} = \frac{1}{6q}\left(4q + \frac{1}{(1-q)^2} - 1\right) \tag{3.2}$$

where $q = Q^*/\sqrt{b}$. As the aim of this chapter is to compare predictions of bead-spring models with bead-rod models, we have employed the same EV force (derived from the purely repulsive Lennard Jones potential) that has been used by Petera and Muthukumar [157] and Liu et al. [129]. However, due to the differences in the length and time scales used in the bead-rod and bead-spring models, the excluded volume force used in Refs. 157 and 129 is renondimensionalised by using l_H and λ_H. The following form of the EV force is used in our simulations:

$$\mathbf{F}^*_{\mu} = \frac{\mathbf{F}_{\mu}}{\sqrt{H k_{\mathrm{B}} T}} = \sum_{\mu \neq \nu} \frac{p\bar{A}(2\bar{R}_{\mathrm{ex}} l_R)^p / l_H^p}{\left(r^*_{\mu\nu}/l_H\right)^{p+2}} \frac{\mathbf{r}^*_{\mu\nu}}{l_H} = \sum_{\nu \neq \mu} \frac{p\bar{A}(2\bar{R}_{\mathrm{ex}} l_R / l_H)^p}{\left(r^*_{\mu\nu}\right)^{p+2}} \mathbf{r}^*_{\mu\nu} \tag{3.3}$$

In the above equation, $l_R = l$ and $\lambda_R = l^2 \zeta / k_{\mathrm{B}} T$ are, respectively, the length and time scales used in bead-rod model [129; 157]. Here, $p = 12$, $\bar{A}$ is the strength of excluded volume interaction and $\bar{R}_{\mathrm{ex}}$ is the dimensionless excluded volume radius of bead in the bead-rod model. Note that this is not the same as the dimensionless bead radius in the bead-rod model, $\bar{R}_{\mathrm{hyd}}$ ($\bar{R}_{\mathrm{hyd}} = R_{\mathrm{hyd}}/l_{\mathrm{R}}$) [157]. In the rest of the chapter, the "*" superscript is used to indicate that the parameters are non-dimensionalized by l_H and λ_H, while "-" denotes a non-dimensionalization by l_R and λ_R.

In order to predict the rheological properties of a polymer solution, we use Kramers expression for the stress tensor $\boldsymbol{\tau}_{\mathrm{p}}$ [22]. The dimensionless form of Kramers expression is given by

$$\boldsymbol{\tau}_{\mathrm{p}}^{*} = \frac{\boldsymbol{\tau}_{\mathrm{p}}}{n_{\mathrm{p}} k_{\mathrm{B}} T} = (N-1)\boldsymbol{\delta} + \sum_{\nu=1}^{N} \left\langle \mathbf{R}_{\nu}^{*} \mathbf{F}_{\nu}^{\phi *} \right\rangle \tag{3.4}$$

where n_{p} is the number density of polymer, $\mathbf{R}_{\nu}^{*} = \mathbf{r}_{\nu}^{*} - \mathbf{r}_{\mathrm{c}}^{*}$ is the position vector of the bead with respect to the center-of-mass $\mathbf{r}_{\mathrm{c}}^{*}$ and $\mathbf{F}_{\nu}^{\phi *} = \mathbf{F}_{\nu}^{\mathrm{s}\,*} + \mathbf{F}_{\nu}^{\mathrm{int}*}$. The angular bracket represents an ensemble average with respect to the configurational distribution function of the chain [22].

In this work, we have computed the zero-shear rate polymer viscosity ($\eta_{\mathrm{p},0}$) and the zero-shear rate first normal stress difference coefficient ($\Psi_{1,0}$).

In the absence of EV and HI, both $\eta_{\mathrm{p},0}$ and $\Psi_{1,0}$ are known analytically for the bead-spring and the infinitely stiff Fraenkel spring models. The dimensionless zero-shear rate viscosity ($\eta_{\mathrm{p},0}^{*}$) for a free draining bead-spring model derived using a retarded motion expansion is given by [167; 194]

$$\eta_{\mathrm{p},0}^{*} = \frac{\eta_0 - \eta_{\mathrm{s}}}{n_{\mathrm{p}} k_{\mathrm{B}} T \lambda_H} = \frac{2N}{3} \left\langle R_g^{*2} \right\rangle_{\mathrm{eq}} = \frac{N^2 - 1}{3} \chi^2(b) \tag{3.5}$$

where $\left\langle R_g^{*2} \right\rangle_{\mathrm{eq}}$ is the dimensionless equilibrium mean square radius of gyration, $\chi^2(b) = \left\langle Q^{*2} \right\rangle / 3$ is the mean square equilibrium length of a spring in the FES chain non-dimensionalised by the root mean square equilibrium length of a Hookean spring [194] and η_0 is the solution viscosity. Similarly, for the infinitely stiff Fraenkel spring model, the dimensionless zero-shear rate polymer viscosity ($\bar{\eta}_{\mathrm{p},0}$) is given by [22]:

$$\bar{\eta}_{\mathrm{p},0} = \frac{\eta_0 - \eta_{\mathrm{s}}}{n_{\mathrm{p}} k_{\mathrm{B}} T \lambda_R} = \frac{N_{\mathrm{k}}(N_{\mathrm{k}} + 2)}{36} \tag{3.6}$$

Note that the above expression also valid for the Kramers bead-rod chain [22; 110].

For bead-spring chains, the dimensionless zero-shear rate first normal stress coefficient (${\Psi^S_{1,0}}^*$) is given by [206]

$$
\begin{aligned}
{\Psi^S_{1,0}}^* = \frac{\Psi^S_{1,0}}{n_\mathrm{p} k_\mathrm{B} T \lambda_H^2} = \left(\frac{4}{15}\right) \Bigg[& \left(\frac{\left\langle Q^{*4} \right\rangle_\mathrm{eq}}{15} - \frac{\left\langle Q^{*2} \right\rangle_\mathrm{eq}^2}{9} \right) \left(\frac{N^4 - 1}{N} \right) \\
& + \left(\frac{\left\langle Q^{*2} \right\rangle_\mathrm{eq}^2}{9} \right) \left(\frac{(N^2-1)(2N^2+7)}{6} \right) \Bigg]
\end{aligned}
\tag{3.7}
$$

and for the infinitely stiff Fraenkel spring, the analytical expression for the dimensionless zero-shear rate first normal stress difference coefficient $\bar{\Psi}^F_{1,0}$ is [22]

$$
\bar{\Psi}^F_{1,0} = \frac{\Psi^F_{1,0} k_\mathrm{B} T}{n_\mathrm{p} \zeta^2 l^4} = \frac{\Psi^F_{1,0}}{n_\mathrm{p} k_\mathrm{B} T \lambda_R^2} = \frac{N_\mathrm{k}(N_\mathrm{k}+2)(10N_\mathrm{k}^3 + 18N_\mathrm{k}^2 + 41N_\mathrm{k} + 21)}{16200(N_\mathrm{k}+1)} \tag{3.8}
$$

where l is the length of the stiff spring (the same as the length of a rod in the bead-rod model). To our knowledge, an analytical expression for the first normal stress difference coefficient for the bead-rod model with an arbitrary number of beads is not available in the literature (even when EV and HI are absent). Equation (3.7), where $\left\langle Q^{*2} \right\rangle_\mathrm{eq}$ and $\left\langle Q^{*4} \right\rangle_\mathrm{eq}$ are respectively, the non-dimensional equilibrium averages of the second and fourth moment of the connector vector of a spring, are valid for any spring force law.

In the presence of HI, however, analytical expressions for $\eta_{\mathrm{p},0}$ cannot be derived and hence, a Green-Kubo formula is used. The Green-Kubo formula relates the autocorrelation function C_s with $\eta^*_{\mathrm{p},0}$ as [193]

$$
\eta^*_{\mathrm{p},0} = \int_0^\infty C_s(t)\, dt \tag{3.9}
$$

The autocorrelation function $C_s(t)$ is related, for instance in a dumbbell, to the equilibrium autocorrelation of the quantity $S_{xy} = Q_x \partial U / \partial Q_y$ (where, Q_x is the x-component of the connector vector $\mathbf{Q}$ and U is the potential energy of the bead-spring chain) by,

$$
C_s(t) = \left\langle S_{xy}(t)\, S_{xy}(0) \right\rangle_\mathrm{eq} \tag{3.10}
$$

Further details on the autocorrelation function for bead-spring chains can be found in Sunthar et al. [193].

3.3 Choice of value for the hydrodynamic interaction parameter

The strength of HI is governed by the non-draining parameter h [88; 90; 194; 213; 215]. For the bead-rod model, $h \equiv h_R = h_k^* \sqrt{N_\mathrm{k}+1}$, where $h_k^* = \sqrt{3/\pi}\bar{R}_\mathrm{hyd}$ is the HI parameter used by Petera and Muthukumar [157]. Sunthar and Prakash [194] have shown that for FES chains, the strength of HI is given by $h \equiv h_S = \tilde{h}^* \sqrt{N}$, where $\tilde{h}^* = h^*/\chi$ and h^* is the hydrodynamic interaction parameter for chains with Hookean springs. Here, we choose to impose three different choices for $\tilde{h}^*$ in order to investigate the convergence behavior of the extrapolation process in the SFG scheme in the presence of HI.

3.3.1 Case 1

In this case, $\tilde{h}^*$ is chosen to have a constant value in the SFG scheme [166; 194]. As a result, $\tilde{h}^* = h_k^*$. With this value of $\tilde{h}^*$, both the bead-rod and bead-spring models have the same value of h in the limit $N_\mathrm{s} \to N_\mathrm{k}$.

3.3.2 Case 2

In the second case, $\tilde{h}^*$ is assumed to have a constant value such that both the bead-rod and bead-springs models have the same value of h in the limit of $N_\mathrm{s} \to N_\mathrm{c}$. In other words, we set $h_S = h_R$ at $N_\mathrm{s} = N_\mathrm{c}$. With this choice of h_S, $\tilde{h}^* = h_k^* \sqrt{(N_\mathrm{k}+1)/(N_\mathrm{c}+1)}$ Note that in both of these cases, the non-draining parameter h_S changes with N as the fine-graining procedure is carried out, and is equal to h_R in the extrapolation limit. The value of N_c for various force laws is discussed shortly.

3.3.3 Case 3

Here, $\tilde{h}^*$ is chosen such that at any fine graining level, the bead-spring model has the same value of h as the bead-rod model. This implies that the strength of HI is kept invariant as fine-graining is carried out. This ensures $h_S = h_R$ for all values of N. In this case, $\tilde{h}^* = h_k^* \sqrt{(N_\mathrm{k}+1)/N}$. For the special case, $N = N_\mathrm{c}$, $\tilde{h}^*$ in case 3, has the same value as in case 2. In other words, simulations (with all other parameters kept the same) at $N = N_\mathrm{c}$ are identical in both cases 2 and 3.

3.4 Results and discussion

The numerical computations are performed with the same set of non-dimensional parameters ($\bar{A} = 1$, $\bar{R}_{\text{hyd}} = 0.5$ and $\bar{R}_{\text{ex}} = 0.4$) as was used by Petera and Muthukumar [157], except for the time step, Δt^*. For linear viscoelastic properties, a time step size of $\Delta t^* = 0.01$ was used which yielded a time converged solution for an ensemble average of 3×10^5 trajectories. For shear flow, different values of time step size, depending upon the flow strength ($\dot{\gamma}^*$), are used to obtain the ensemble averages over 10^5 independent trajectories. In shear flow, we have used the same set of time steps as used by Hsieh et al. [87]. Computations with a smaller set of time steps were also carried out to ensure the time step convergence of our results. The convention used to represent our results is similar to that used by Petera and Muthukumar [157]; +EV/-EV indicates whether excluded volume is present or not and +HI/-HI indicates whether hydrodynamic interactions are present or not.

3.4.1 Upper bound on the number of beads in the bead-spring model

As the SFG results may be extrapolated to a limit where $N_{\text{s}} \rightarrow N_{\text{k}}$ or $N_{\text{s}} \rightarrow N_{\text{c}}$, it is important to investigate the limit of N beyond which the different force laws used in this study are no longer valid.

In the SFG procedure, certain static properties are kept invariant, such as the square end-to-end vector R_{e}^2 and maximum stretch length L_{max} of polymer molecule, as they do not depend on N [166; 194]. For the bead-spring models, $R_{\text{e,S}}^2 = 3\chi^2 l_H^2 (N-1)$ and $L_{\text{max,S}} = (N-1)\sqrt{b}\, l_H$, and for the bead-rod model $R_{\text{e,R}}^2 = l_R^2 N_{\text{k}}$ and $L_{\text{max,R}} = l_R N_{\text{k}}$ [22; 194].

By equating the ratios of $R_{\text{e}}^2 / L_{\text{max}}$ obtained from the bead-rod and bead-spring models, it is possible to relate the spring force parameters with N_{k} and N as [166; 194]

$$\frac{1}{N_{\text{k}}} = \frac{3\chi^2(b)}{b(N-1)} \tag{3.11}$$

Also the ratio of $L_{\text{max,R}} / L_{\text{max,S}}$ gives l_R / l_H as

$$\frac{l_R}{l_H} = \frac{(N-1)\sqrt{b}}{N_{\text{k}}} \tag{3.12}$$

The term χ^2 in Eq. (3.11), which is a function of b, depends upon the spring force law. Since it is related to $\langle Q^{*2} \rangle$, the equilibrium distribution function ψ_{eq} is used to evaluate χ^2 [22]. The equilibrium average of the second moment of the connector vector is given by

$$\langle \mathbf{Q}^{*2} \rangle = \langle Q^{*2} \rangle = \frac{\int_0^{\sqrt{b}} Q^{*4} e^{-\phi/k_{\text{B}}T} dQ^*}{\int_0^{\sqrt{b}} Q^{*2} e^{-\phi/k_{\text{B}}T} dQ^*} \tag{3.13}$$

where the spring potential ϕ is related to the spring force by $\mathbf{F}^{\text{s}} = \partial\phi/\partial\mathbf{Q}$. The dimensionless spring potentials, $\phi^* = \phi/k_{\text{B}}T$ for three force laws, used in this work, are given by

$$\phi^*_{\text{ILC}} = \frac{b}{6}q^2 - \frac{b}{3}\ln\left(1-q^2\right);\ \phi^*_{\text{FENE}} = -\frac{b}{2}\ln\left(1-q^2\right);\ \phi^*_{\text{WLC}} = \frac{b}{6}\left[2q^2 + \frac{1}{(1-q)} - q\right] \tag{3.14}$$

For the FENE force law, χ^2 can be evaluated analytically as:

$$\chi^2 = \frac{b}{b+5} \tag{3.15}$$

Combining Eqs. 3.11 and 3.13 gives,

$$(N-1)/N_{\text{k}} = \frac{\int_0^1 q^4 e^{-\phi^*} dq}{\int_0^1 q^2 e^{-\phi^*} dq} \tag{3.16}$$

As $b > 0$, the above equation imposes an upper bound on N that can be used in bead-spring models for a given value of N_{k}. If $N_{\text{s}} = N_{\text{c}}$ for $b = 0$, then, since $\phi^* \to 0$, as $b \to 0$, for all force laws

$$N_{\text{c}} = \frac{3N_{\text{k}}}{5} \tag{3.17}$$

The above equation implies that as $b \to 0$, the value of N_{c} is the same for all different force laws used in this work.

From Eq. 3.11, to obtain the value of b for a particular N_{k} value at each level of fine graining N, an expression for χ as a function of b or N is required.

Since analytical expressions for χ for ILC and WLC force laws cannot be derived, χ is evaluated numerically by using a Gauss quadrature integration formula [194].

Figure 3.1 shows the values of $b/3\chi^2(b)$ as a function of b for different force laws. $b/3\chi^2(b)$ is evaluated for a given N_{k} and N from Eq. (3.11). A fitting procedure proposed by Sunthar and Prakash [194] is used to fit the data for ILC and WLC

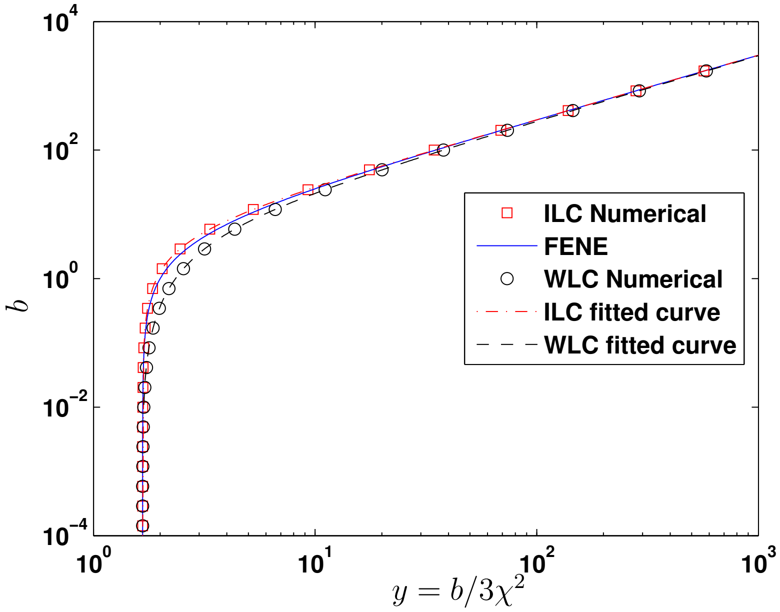

Figure 3.1: The mean square dimensionless maximum stretching length of a spring for a range of $N_\mathrm{k}/N_\mathrm{s}$ ratios (i.e y) for all the three force laws.

Table 3.1: The values of the coefficients for the series approximation, which accurately fit the obtained numerical values of the ILC and WLC force laws.

Type	c_1	c_2	c_3	c_4	c_5	c_6
ILC	0.0002	-1.1144	0.0108	-0.7707	-0.6125	0.5210
WLC	-0.6137	-0.7207	-0.5490	-1.6144	1.6788	1.2590

force laws. The following series is used to represent the data in Fig. 3.1

$$b = 3y\left[1 + \frac{c_1}{\sqrt{y}} + \frac{c_2}{y} + \frac{c_3}{\sqrt{y^3}} + \frac{c_4}{y^2} + \frac{c_5}{\sqrt{y^5}} + \frac{c_6}{y^3}\right] \tag{3.18}$$

where $y = b/3\chi^2(b)$. The values of various parameters $(c_1, \ldots, c_6)$ for the ILC and WLC force laws are presented in Table 3.1. These values have been obtained by a nonlinear least-squares regression fit of the numerical data in the b vs y space. Thus for any given values of N_k and N, b can be determined via y from Fig. 3.1 or Eq. 3.18, and subsequently, $\chi(b)$ can be obtained. While Sunthar and Prakash [194] have performed a similar fitting procedure for the WLC force law, it is extended here to the limit $b \to 0$.

3.4.2 Linear viscoelastic properties

In this section we present the analytical and numerical results for linear viscoelastic properties obtained using the SFG method. The analytical calculations are carried out for the case where both HI and EV interactions are absent. Most of the previous results derived in the literature for the linear viscoelastic properties for free draining bead-spring chains without EV are the functions of the spring parameters and the number of beads and hence, cannot be used directly to compare with results for Kramers bead-rod chains [22; 167; 206] (the exception are the results of infinitely stiff Fraenkel spring [22; 206]). In our work, we have used expressions for the zero-shear rate viscosity and zero-shear rate first normal stress coefficient which, in literature, are expressed in term of the beads N, the second moment $\left\langle Q^{*2}\right\rangle_{\text{eq}}$ and the fourth moment $\left\langle Q^{*4}\right\rangle_{\text{eq}}$ of the end-to-end vector given in Refs. 22; 167; 206 to derive expressions which can be directly compared to the bead-rod results.

3.4.2.1 SFG - Validation from kinetic theory for free-draining chains without EV

The dimensionless zero-shear rate viscosity and zero-shear rate first normal stress difference coefficient predicted by the bead-spring model non-dimensionalised by the time scale of the bead-rod model are

$$\bar{\eta}_{S,0} \equiv \eta^{*}_{\text{p},0}\frac{\lambda_H}{\lambda_R}; \quad \bar{\Psi}^{S}_{1,0} \equiv {\Psi^{S}_{1,0}}^{*}\frac{\lambda_H^2}{\lambda_R^2} \tag{3.19}$$

Equation (3.19) can be used to compare the results of the bead-spring chain model directly with the bead-rod model as they are based on the same length and time scales. The ratio λ_H/λ_R depends on the coarse graining procedure adopted for evaluating the friction coefficient. Here, for the free-draining case without EV, two different values of friction coefficients are chosen to study the convergence behavior of the results and to show that SFG extrapolations are independent of these choices.

For the first case, denoted as case (a), the total friction on the bead-spring chain is kept the same as that of the bead-rod chain at any level of fine graining. By equating the total friction on the chain in the two models, the ratio of bead friction coefficients can be determined

$$\zeta_R(N_\mathrm{k}+1)=\zeta_S N \qquad \Rightarrow \qquad \frac{\zeta_R}{\zeta_S}=\frac{N}{N_\mathrm{k}+1} \tag{3.20}$$

where ζ_R and ζ_S are the bead friction coefficients in the bead-rod and bead-spring models, respectively. The ratio λ_R/λ_H for this case is

$$\frac{\lambda_R}{\lambda_H}=\frac{\zeta_R l_R^2}{k_\mathrm{B}T}\frac{4k_\mathrm{B}T}{l_H^2\zeta_S}=\frac{4N}{(N_\mathrm{k}+1)}\frac{l_R^2}{l_H^2}=\frac{4bN(N-1)^2}{N_\mathrm{k}^2(N_\mathrm{k}+1)} \tag{3.21}$$

From Eqs. (3.5), (3.7), (3.19) and (3.21)

$$\bar{\eta}_{S_a,0}=\frac{\chi^2}{b}\frac{N_\mathrm{k}^2(N_\mathrm{k}+1)^2}{12N(N-1)} \tag{3.22}$$

$$\bar{\Psi}_{1,0}^{S_a}=\frac{{\Psi_{1,0}^{S}}^*}{b^2}\frac{N_\mathrm{k}^4(N_\mathrm{k}+1)^2}{16N^2(N-1)^4} \tag{3.23}$$

In case (b), the bead friction coefficient in the bead-spring model is kept the equal to that of the bead-rod model at each level of fine graining, i.e. $\zeta_R=\zeta_S$. This implies that both the bead-rod and bead-spring models have the same total friction coefficient in the limit of $N_\mathrm{s}\to N_\mathrm{k}$. The ratio λ_R/λ_H for this case is

$$\frac{\lambda_R}{\lambda_H}=\frac{\zeta_R l_R^2}{k_\mathrm{B}T}\frac{4k_\mathrm{B}T}{l_H^2\zeta_S}=\frac{4l_R^2}{l_H^2}=\frac{4b(N-1)^2}{N_\mathrm{k}^2} \tag{3.24}$$

From Eq. (3.5), (3.7) (3.19) and (3.24)

$$\bar{\eta}_{S_b,0}=\frac{\chi^2}{b}\frac{N_\mathrm{k}^2(N+1)}{12(N-1)} \tag{3.25}$$

$$\bar{\Psi}_{1,0}^{S_b}=\frac{\Psi_1^{S*}}{b^2}\frac{N_\mathrm{k}^4}{16(N-1)^4} \tag{3.26}$$

The terms χ^2/b (and hence, $\left\langle Q^{*2}\right\rangle/b$) and $\left\langle Q^{*4}\right\rangle/b^2$ are required in Eqs. (3.22), (3.23), (3.25) and (3.26). While these terms are analytically known for the FENE force [22], there are no closed-form expressions for the ILC and the WLC force laws, and have to be computed numerically.

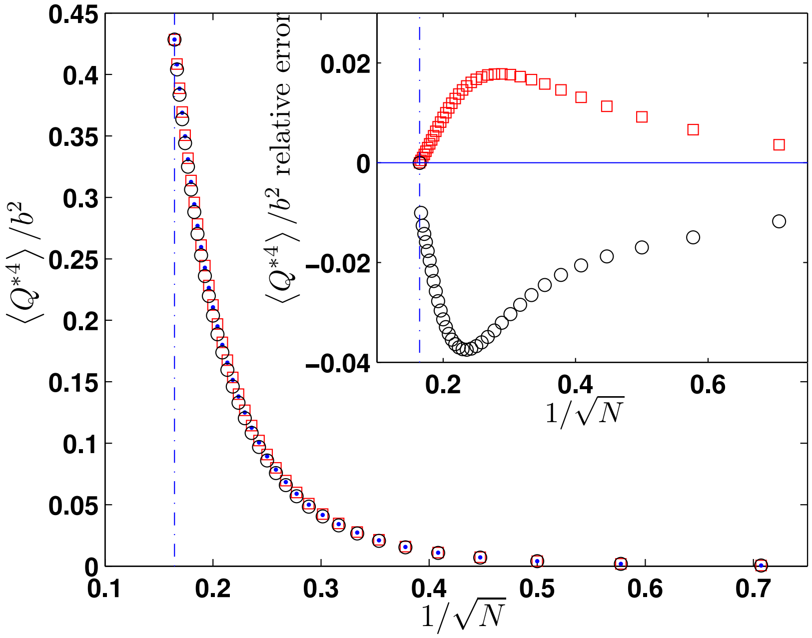

Figure 3.2: The equilibrium average of the fourth moment of the connector vector of a spring divided by b^2 ($\langle Q^{*4} \rangle /b^2$) for $N_\mathrm{k} = 60$ at various $N \leq N_\mathrm{c}$(dash-dot line) values for FENE ($\cdot$), ILC ($\Box$) and WLC ($\circ$). Inset shows the relative error in $\langle Q^{*4} \rangle /b^2$ for ILC and WLC force laws at each level of fine graining. Relative error is defined as Relative Error $= \dfrac{(\langle Q^{*4} \rangle /b^2)_\mathrm{FENE} - (\langle Q^{*4} \rangle /b^2)_\mathrm{ILC\ or\ WLC}}{(\langle Q^{*4} \rangle /b^2)_\mathrm{FENE}}$

From Eq. (3.11), $\langle Q^{*2} \rangle /b$ is

$$\frac{\langle Q^{*2} \rangle}{b} = \frac{3\chi^2}{b} = \frac{N-1}{N_\mathrm{k}} \tag{3.27}$$

The above equation in independent of the choice of spring force law. For a FENE spring, $\langle Q^{*4} \rangle_\mathrm{eq}$ is given by [22]

$$\langle Q^{*4} \rangle_\mathrm{eq} = \frac{15b^2}{(b+5)(b+7)} \tag{3.28}$$

Figure (3.2) shows the numerical results for $\langle Q^{*4} \rangle_\mathrm{eq} /b^2$ for the ILC and WLC force laws together with the analytical result for the FENE spring force law. Since the maximum deviation in $\langle Q^{*4} \rangle_\mathrm{eq} /b^2$ for ILC and WLC force laws is between 2 to 4% compared to the FENE force law for a given value of N_k, it is reasonable to assume that $\left\langle Q^{*4}\right\rangle_{\rm eq}/b^2$ is independent of the choice of force law for all values of N and hence, Eq. (3.28) can be used for ILC and WLC as well. Note that deviation in the results for ILC and WLC force laws occur only for the intermediate values of b. Analytically, the independence of $\left\langle Q^{*4}\right\rangle_{\rm eq}/b^2$ with respect of the nature of the force law in the limit of large b ($b \rightarrow \infty$) and small b ($b \rightarrow 0$) can be seen from the following expression:

$$\left\langle Q^{*4}\right\rangle/b^2 = \frac{\int_0^1 q^6 e^{-\phi^*} dq}{\int_0^1 q^2 e^{-\phi^*} dq} \tag{3.29}$$

For $b \rightarrow 0$, $\phi^* \rightarrow 0$ and hence, $\left\langle Q^{*4}\right\rangle/b^2$ is independent of choice of the force law. For $b \rightarrow \infty$, all finitely extensible force laws reduce to the Hookean force law which implies $\left\langle Q^{*4}\right\rangle/b^2$ is independent of force law. The difference for intermediate values of b is depicted in Fig. 3.2.

Substituting Eq. (3.27) into Eqs. (3.22) and (3.25)

$$\bar{\eta}_{S_a,0} = \frac{N_{\rm k}(N_{\rm k}+1)(N+1)}{36N}; \quad \bar{\eta}_{S_b,0} = \frac{N_{\rm k}(N+1)}{36} \tag{3.30}$$

From Eqs. (3.11), (3.15), (3.23), (3.26) and (3.28)

$$\begin{aligned} \bar{\Psi}^{S_a}_{1,0} &= \left(\frac{N_{\rm k}^3(N_{\rm k}+1)^2(N+1)}{180N^3(N-1)}\right)\left[\frac{N^2+1}{3N_{\rm k}+2(N-1)} + \frac{2N^3-6N^2+7N-6}{18N_{\rm k}}\right] \\ \bar{\Psi}^{S_b}_{1,0} &= \left(\frac{N_{\rm k}^3(N+1)}{180N(N-1)}\right)\left[\frac{N^2+1}{3N_{\rm k}+2(N-1)} + \frac{2N^3-6N^2+7N-6}{18N_{\rm k}}\right] \end{aligned} \tag{3.31}$$

In the limit $N_{\rm s} \rightarrow N_{\rm k}$,

$$\bar{\eta}_{S,0} = \bar{\eta}_{S_a,0} = \bar{\eta}_{S_b,0} = \frac{N_{\rm k}(N_{\rm k}+2)}{36} \tag{3.32}$$

$$\bar{\Psi}^{S}_{1,0} = \bar{\Psi}^{S_a}_{1,0} = \bar{\Psi}^{S_b}_{1,0} = \frac{N_{\rm k}(N_{\rm k}+2)(10N_{\rm k}^3+18N_{\rm k}^2+41N_{\rm k}+21)}{16200(N_{\rm k}+1)} \tag{3.33}$$

Although, as $N_{\rm s} \rightarrow N_{\rm k}$, the spring force laws for the FES chain are no longer valid (χ and b do not have any physical meaning) the analytical expressions for the zero-shear rate intrinsic viscosity and the zero-shear rate first normal stress coefficient for the bead-spring models are exactly the same as the known expressions for the random walk chain or the Fraenkel spring with infinite stiffness [Eq. (3.6) and (Eq. (3.8)].

The analytical results for this simple case suggest that the limit of extrapolation for the SFG scheme is N_{k} and not N_{c}.

3.4.2.2 Numerical results

In this section we compare numerical results for linear viscoelastic properties obtained using the SFG scheme with the bead-rod model.

Numerically the zero-shear rate viscosity can be obtained in two different ways. It can either be obtained by accumulating data at various finite shear rates and extrapolating the results to the limit of zero shear rate or by using the Green-Kubo expression. While Petera and Muthukumar [157] used the extrapolation method to obtain the zero-shear rate viscosity with the bead-rod model, we have used the Green-Kubo formulation.

In order to compare $\bar{\eta}_{S,0}$ obtained from the bead-spring model with that of bead-rod model, the ratio λ_R/λ_H is required. For free draining chains, either Eq. (3.21) or (3.24) can be used. In the presence of HI, since $\lambda_R = 6\pi\eta_{\mathrm{s}}\bar{R}_{hyd}l_R^3/k_{\mathrm{B}}T$, and $\lambda_H = (3\eta_{\mathrm{s}}\pi^{3/2}l_H^3h^*)/2k_{\mathrm{B}}T$, the ratio λ_R/λ_H is

$$\frac{\lambda_R}{\lambda_H} = \frac{4\bar{R}_{hyd}}{\sqrt{\pi}h^*}\left(\frac{l_R}{l_H}\right)^3 = \frac{4\bar{R}_{hyd}b^{3/2}(N-1)^3}{\sqrt{\pi}h^*N_{\mathrm{k}}^3} \tag{3.34}$$

Figure 3.3 displays analytical and numerical results computed using the SFG scheme for different force laws and two different values of N_{k} as a function on N. The results in Fig. 3.3 are plotted as a function of $1/N$ because in the absence of HI and EV, the zero-shear rate viscosity is proportional to $1/N$ provided the total friction is kept the same (Eq.3.30). The bead-rod results of Petera and Muthukumar [157] and extrapolated results of the SFG scheme in the limit $N_{\mathrm{s}} \rightarrow N_{\mathrm{k}}$ are also displayed for comparison. The results obtained at the extrapolated limit N_{k} for two different N_{k} values are in excellent agreement with the theoretical values for a random walk chain and also it is clear that N_{k} is in fact the right limit to obtain the extrapolated results. On the other hand, the values reported by Petera and Muthukumar [157] show a discrepancy from analytical results. As Liu [130] have shown that the zero-shear rate viscosity and zero-shear rate first normal stress difference coefficient predicted by the bead-rod model using the mid-point algorithm are in good agreement with random walk results, a possible source for the discrepancy in the results of Petera and Muthukumar [157] could be due to their extrapolation of finite shear rate data

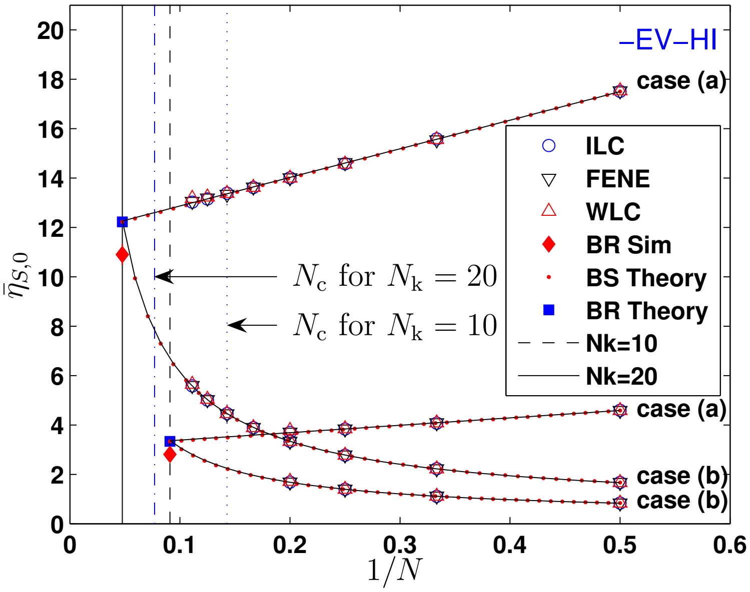

Figure 3.3: Zero-shear rate viscosity for $N_k = 10$ and $N_k = 20$ for the two different approaches. Symbols indicate simulations data obtained at various values of N for ILC (○), FENE(▽) and WLC (△). The error bars are smaller than the size of symbols. 'BR Sim' represents results of Petera and Muthukumar [157]. 'BS Theory' are SFG results evaluated from Eq. (3.30). 'BR Theory' represents the theoretical values for a bead-rod or a random walk chain model (Eq. (3.32)). The case (a) represents the situation where the total friction coefficient on the bead-spring chain is kept the same as that of the bead-rod chain at any level of fine graining and the case (b) represents the situation where the bead friction coefficient on the bead-spring chain is kept the same as that of the bead-rod chain.

to zero-shear. As can be seen from Fig. 3.3, case (a), where the total fiction in the bead-spring chain is kept equal to that the total friction on bead-rod chain, leads to faster convergence of bead-spring results to the bead-rod results.

Similar to the free draining case under θ-conditions, the values of $\bar{\eta}_{S,0}$ in the presence of HI is shown in Fig. 3.4 for the three different choices of HI parameter discussed in section 3.3 and for two N_k values as a function of N. In the presence of HI, Sunthar and Prakash [194] have shown that the leading order correction for any universal ratio is $1/\sqrt{N}$. Since the zero-shear rate viscosity is related to the universal ratio via the radius of gyration of the chain (i.e. $\eta^*_{p,0} \sim U_{\eta R} R_g^{*3}$), it can be shown that the zero-shear rate viscosity is also a function of $1/\sqrt{N}$. Therefore, it is more appropriate to use $1/\sqrt{N}$ in the extrapolation scheme for the cases involving HI. For all three choices of HI parameters, the non-dimensional results vary smoothly

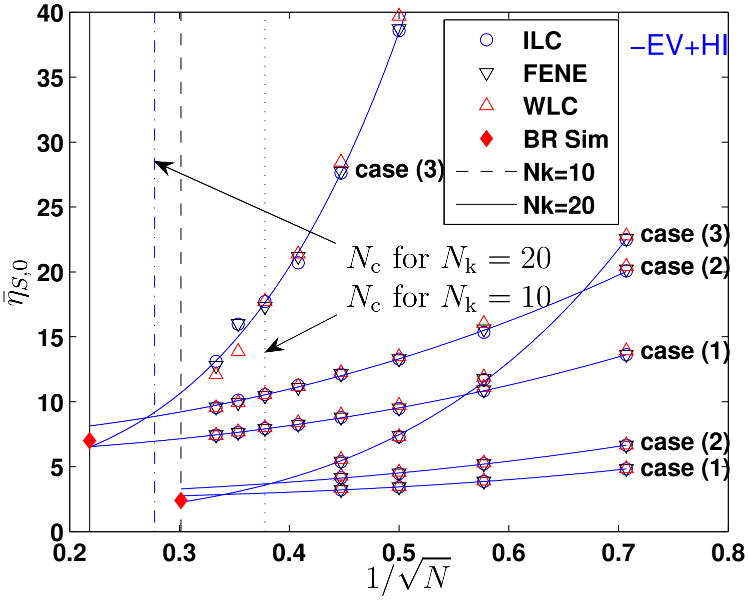

Figure 3.4: Zero-shear rate viscosity for $N_\mathrm{k} = 10$ and $N_\mathrm{k} = 20$ for three different HI parameter choices. The error bars are smaller than the size of symbols. ‘BR Sim’ represents values reported by Petera and Muthukumar [157].

with N, and are independent of the force law. For linear viscoelastic properties, the choice of spring force law appears to be an irrelevant issue. For case 1, it is not clear whether N_c or N_k is the proper limit for both $N_\mathrm{k} = 10$ and 20. The difficulty is further compounded by the fact that Petera and Muthukumar [157] do not report error bars on their values for the case of HI without EV. However, cases 2 and 3 clearly reveal that the limit $N_\mathrm{s} \to N_\mathrm{k}$ is in fact the correct limit. At $N = N_\mathrm{c}$, the value of $\bar{\eta}_{S,0}$ in both the cases 2 and 3 is very different from the bead-rod value. Overall, values obtained in the limit N_k using a bead-spring model with the SFG scheme agree very well with the reported values of Petera and Muthukumar [157].

In the presence of HI, it appears that keeping the hydrodynamic interaction parameter $\tilde{h}^* = h^*_k$ (denoted by case 1) leads to the most rapid convergence to the bead-rod result which is in contrast the free draining case discussed earlier.

3.4.3 Shear properties

In this section SFG results are compared with the results of bead-rod and stiff FENE-Fraenkel spring models in shear flow.

In order to compare the results of different models, it is necessary to make sure

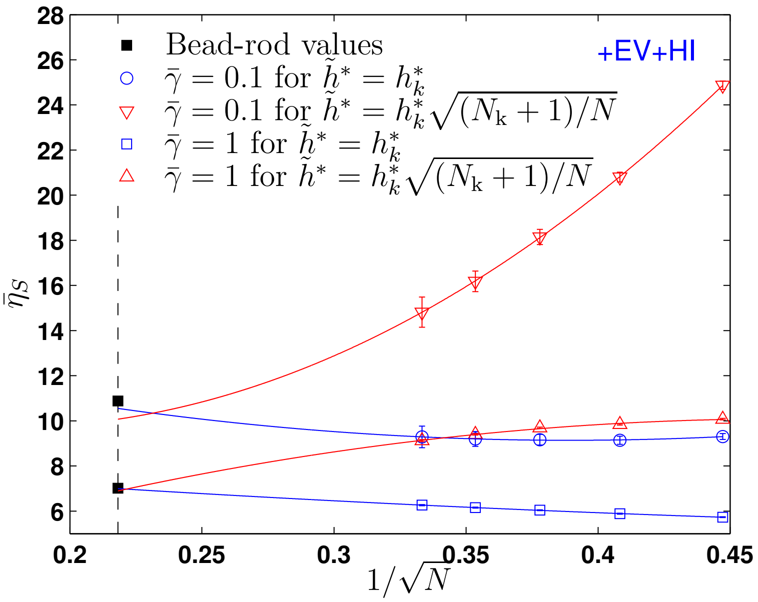

Figure 3.5: The effect of different HI parameter choices on the convergence behavior for the bead-spring model with SFG in the presence of both EV and HI for $N_\mathrm{k} = 20$.

that the chain representing the polymer in different models experiences the same strain rate. Equating the shear rate of the bead-rod and bead-spring model results in $\dot{\gamma}^* = \bar{\gamma}\lambda_H/\lambda_R$, where $\bar{\gamma} = \dot{\gamma}\lambda_R$ is the dimensionless shear rate of the bead-rod model.

Figure 3.5 shows the shear viscosity for two different shear rates as a function of N obtained for bead-spring chains in the presence of both EV and HI. The shear results displayed in Fig. 3.5 further substantiate the earlier result that a choice of $\tilde{h}^* = h_k^*$ leads to faster convergence in the presence of HI.

Since it was shown for linear viscoelastic properties, that keeping the chain total friction [i.e. case (a)] to be the same as that for the bead-rod model in the absence of HI and choosing $\tilde{h}^* = h_k^*$ in the presence of HI leads to rapid convergence of bead-spring results to the bead-rod value, we have chosen these cases to study the validity of SFG in shear flow. Furthermore, only the FENE spring force law is used as it was seen earlier that the results for linear viscoelastic properties are independent of the choice of spring force law. For the purpose of extrapolation of bead-spring results, the TEXTRA program, proposed by Öttinger [155], is used in shear flow. The TEXTRA algorithm is based on the assumption that the various properties are polynomial functions of independent variables. It is clear from Fig. 3.5 that

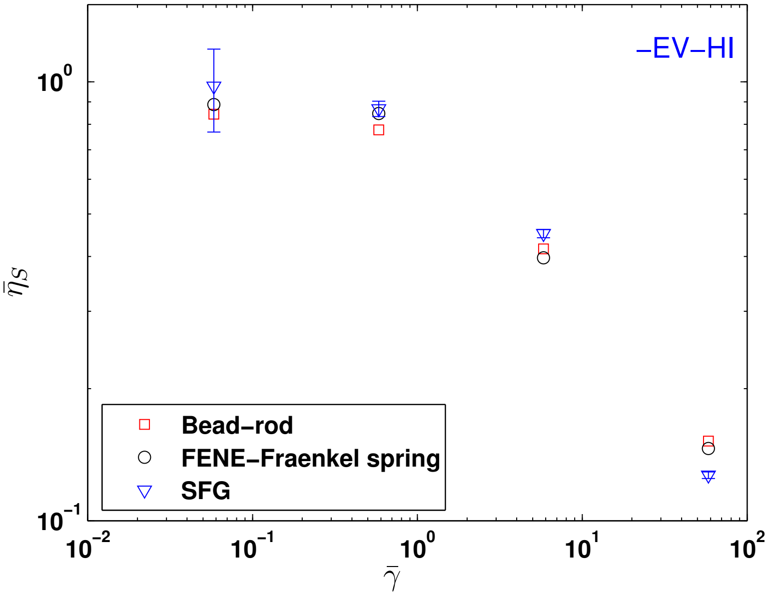

Figure 3.6: Shear viscosity for $N_\mathrm{k} = 10$ in the absence of EV and HI for the bead-rod model, a stiff FENE-Fraenkel spring model and the bead-spring model with SFG.

the extrapolation scheme works very well. The results of extrapolation for all the remaining cases obtained suggest that a quadratic function in $1/\sqrt{N}$ is adequate for fitting purposes.

Figure 3.6 compares the viscosity predicted by three different models for $N_k = 10$ as a function of shear rate in the absence of HI and EV. SFG results agree very well with the results of the bead-rod model as well as the results of FENE-Fraenkel springs up to a shear rate $\bar{\gamma} \sim 50$ and starts to deviate beyond this value. In terms of the reduced shear rate β, which is defined $\beta = \bar{\gamma}\,\bar{\eta}_0$, the value of $\bar{\gamma} \sim 50$ is equivalent to $\beta = 167$ for $N_\mathrm{k} = 10$, which is far greater than values typically encountered in experiments. Ghosh et al. [70] have shown that in a rapid stretching flow, the inverse Langevin force deviates from the force profile of the Kramers chain. This deviation is due to the assumption of local equilibrium for bead-spring chains, which fails in strong flows [22; 52; 87]. The coarse-grained bead-spring model only captures the behavior of the Kramers chain when the product of shear rate and spring relaxation time ($\dot{\gamma}^*$) is of the order of 1 or lower, and it is not realistic to expect SFG to work at very high shear-rates.

Figure 3.7 shows that in the presence of HI, the viscosity data obtained from the stiff FENE-Fraenkel spring model does not coincide with the values of the bead-rod

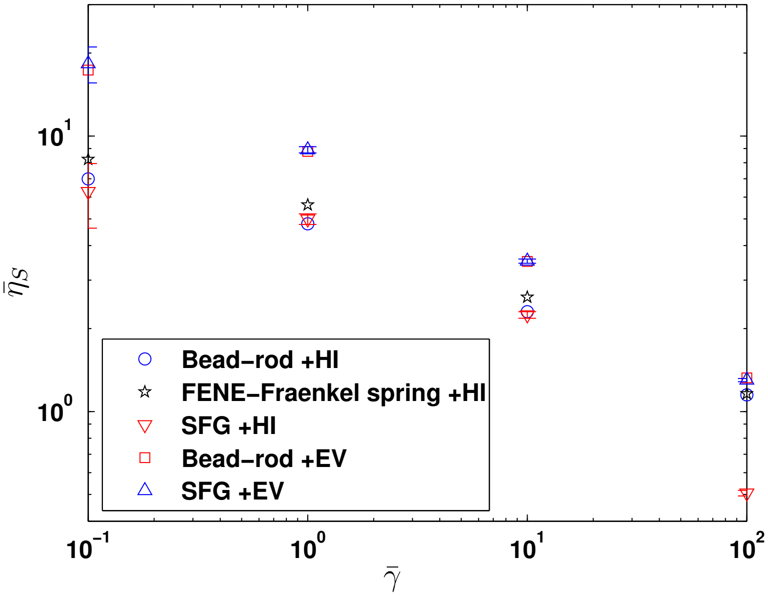

Figure 3.7: The effect of EV and HI on the shear viscosity for $N_{\mathrm{k}} = 20$.

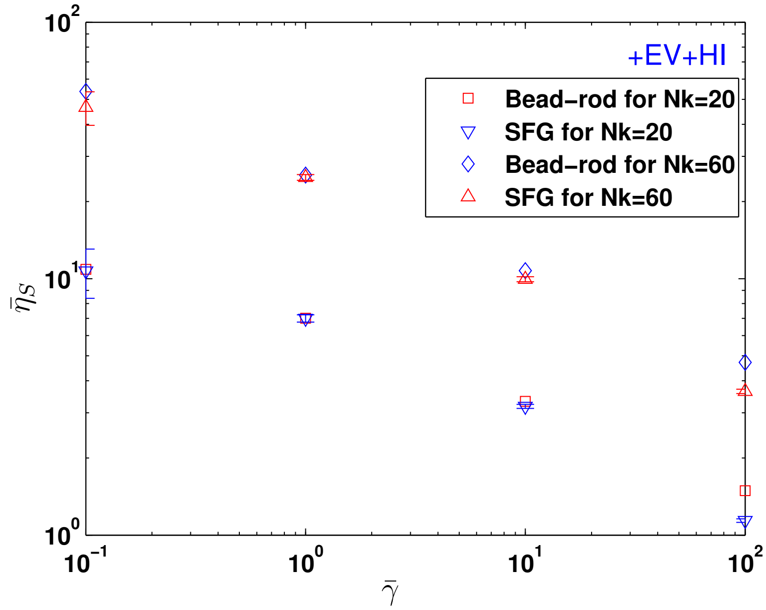

Figure 3.8: Shear viscosity for $N_{\mathrm{k}} = 20$ and $N_{\mathrm{k}} = 60$ in the combined presence of both EV and HI.

model reported by Petera and Muthukumar [157] and the discrepancy is higher at low shear rates. Hsieh et al. [87] have pointed out that this discrepancy is more likely to reside in the code for the bead-rod chain as the bead-rod simulations with HI are complicated to formulate and implement. However, the results obtained from our simulations seem to agree with the results of the bead-rod model rather than the results of stiff FENE-Fraenkel spring model. As in the free draining case, deviations appear at shear rates > 50. In the presence of EV, the viscosity obtained from the SFG method agrees well with the bead-rod values.

The combined effect of both EV and HI on the shear viscosity for $N_k = 20$ and 60 is shown in Fig. 3.8. The results obtained from the SFG method are in excellent agreement with the results of the bead-rod model for both N_k values. Moreover, the deviation at high strain rate values is also observed in this case.

3.5 Conclusions

In this chapter, the successive fine graining scheme (SFG) has been used to investigate the rheological properties of dilute polymer solutions. The validity of the SFG scheme is established by comparing bead-spring chain results with the results of a bead-rod model and a stiff FENE-Fraenkel spring model both in the absence and presence of HI and EV, and in the linear viscoelastic limit and in shear flow. The advantage of SFG is three fold. First, it avoids the complexity introduced by the bead-rod model while preserving the accuracy of computational results. Second, the computational gain, particulary for $N_{\mathrm{k}} \geq 10^3$, is enormous. Third, existing computational algorithm for bead spring chains can be used to obtain bead-rod results with minor changes.

Chapter 4

Implicit and explicit solvent models for the simulation of a single polymer chain in solution: Lattice Boltzmann vs Brownian dynamics

4.1 Introduction

In order to observe large-scale properties, it is crucial to reduce the computational cost by coarse-graining the details of the atomic structure. This is particularly true for polymer systems and studies of their universal static and dynamic properties [44; 50]. In this context, using a conventional bead-spring chain model to represent a polymer molecule in Molecular Dynamics (MD) simulations is usually sufficient [20; 53; 111; 159; 187]. In the case of dilute and semidilute polymer solutions, a correct model also needs to take into account the effect of solvent molecules. This effect is two-fold: On the one hand, the good solvent quality results in swelling of the random coil; on the other, the solvent-mediated long-range dynamic correlations between different segments of the chain, known as hydrodynamic interactions (HI), significantly influence the dynamical behavior [44; 50; 195].

In general, MD simulations are commonly used to simulate polymer solutions.

However, in order to capture hydrodynamic interactions in MD simulations, the solvent particles need to be incorporated explicitly. Typically, the number of solvent particles required for such a model is of the order of thousands even for a short chain. Although such studies are feasible [53], they are rather inefficient, for this reason. Therefore, a more coarse-grained description of the solvent is highly desirable. Two complementary approaches have been developed to do this. "Mesoscopic" methods keep the solvent degrees of freedom, but describe them in a simplified fashion. These include Dissipative Particle Dynamics (DPD) [56; 57; 74; 86; 135; 156; 178], Multi–Particle Collision Dynamics (MPCD) [72; 123; 133], and lattice Boltzmann [3; 6; 7; 19; 34; 54; 116; 117; 118; 192; Dünweg and Ladd]. These approaches are typically one to two orders of magnitude faster than MD [7]. Conversely, Brownian Dynamics (BD) simulations [55; 96; 128; 166; 194] remove the solvent degrees of freedom completely, and take their effect into account via non-trivial long-range dynamic correlations in the stochastic displacements. This is possible due to the time scale separation between the fast solvent motion and the slow conformational polymer degrees of freedom. Since the number of degrees of freedom is reduced drastically, the method has the potential to save CPU time by additional several orders of magnitude, in particular in the dilute limit. However, a simple implementation of the correlations [55] leads to an algorithm which scales like $O(N^3)$, where N is the number of Brownian particles, and therefore becomes infeasible as soon as N exceeds a few hundred [128]. It is therefore very important to treat HI by means of Fixman's algorithm [64] (scaling roughly as $O(N^{2.25})$), which we do in the present study.

Nevertheless, these algorithms are not sufficient to reach $N \sim 10^3 \dots 10^4$; this latter goal is only attainable by the implementation of very recent "superfast" BD algorithms based upon Fast Fourier Transforms [16; 82; 174]. These latter algorithms scale as $N^{1+x} \log N$, where the exponent x depends on the details of the underlying physics, and is usually substantially smaller than unity. These methods require the study of a confined system, and hence are not used in the present study.

While the advantages and disadvantages of the methods are well-known in general terms (and have resulted in differing methodological preferences in different groups of researchers), not much is known *quantitatively* in terms of a clear comparison of computational efficiency. The present work aims at partly filling this gap.

Recently, Dünweg and co-workers [6; 7] has proposed a new mesoscopic method for simulating polymer-solvent systems. The solvent is represented by a fluid on a grid, simulated via the lattice Boltzmann approach, while the motion of the polymer chain is governed by a continuous MD model. The two parts are coupled by a simple dissipative force. The lattice Boltzmann (LB) method was originally developed to simulate hydrodynamics on a grid [19; 34]. It has been shown that the LB method is a fast and effective method for simulating fluid flows, which has the same speed and accuracy as other Navier-Stokes solvers [19; 116; 117; 136]. Ladd [116; 117] successfully applied the LB method to colloidal systems (originally with a *conservative* coupling) and showed that the CPU cost scales linearly with the number of particles. Moreover, he showed how fluctuations can be incorporated into the LB model, which is essential in order to investigate Brownian motion [116]. This procedure has recently been refined and improved [3; 54]. The dissipative coupling method [6; 7] was thoroughly tested by applying it to a single polymer chain in solution, for which the data of a previous MD simulation [53] were available, and whose parameters were used as an input for the mesoscopic model.

In this work, we study the dynamics of a single chain in a solvent to compare the predictions of the explicit solvent model via the LB method with the predictions of the implicit solvent model by BD simulations. We show how to map the input parameters of the hybrid model onto the input values of the BD model to directly compare the predicted quantities.

4.2 Molecular model and simulation methods

This chapter employs the molecular model and simulation techniques described in Chapter 2. However, the early model of Ref. [7] only considered the thermalization of modes related to the viscous stress tensor. It is important to note that even though this procedure is correct in the hydrodynamic limit, it provides poor thermalization on smaller length scales [3]. Adhikari et al. [3] have shown that by applying thermalization to all nonconserved modes one gets a significantly improved numerical behavior at short scales; the theoretical background is now thoroughly understood [54; Dünweg and Ladd]. In this work, we have also investigated the effects of thermalization of the kinetic modes on various dynamic properties.

For these simulations, the parameters ϵ_{LJ}, σ, and τ ($\tau = \sqrt{m\sigma^2/\epsilon_{\mathrm{LJ}}}$, where m is the mass of the monomer) are chosen as the units of energy, length, and time, respectively. The coupling to the beads is done via simple interpolation of the flow velocity from the surrounding sites, and by introducing a phenomenological Stokes friction coefficient ζ_{bare} of the beads. This gives rise to a friction force on the particles, plus a Langevin force that balances the frictional losses. The total momentum is conserved by subtracting the corresponding momentum transfer from the surrounding fluid. It can be shown that this procedure satisfies the fluctuation-dissipation theorem [Dünweg and Ladd]. Further technical details on this method and its theoretical analysis, are given in Ref. [Dünweg and Ladd].

Since the length and time units used for the lattice Boltzmann simulations are different from the ones used in the Brownian dynamics simulations, the EV and FENE forces in the BD simulation have been re-dimensionalised by l_H and λ_H. In the rest of the chapter, the "*" superscript is used to indicate that the parameters are non-dimensionalized by l_H and λ_H, while "-" denotes a non-dimensionalization by σ and τ.

4.2.1 Input parameters for the lattice Boltzmann method

The physical input values for the present model are chosen from the benchmark values developed in Ref. [7], which have been shown to reproduce the results of a typical pure MD simulation [53]. As in the comparison between LB and MD simulations, we study a system of a single polymer chain of length $N = 32$ monomers immersed in a fluid with temperature $k_{\text{B}}T/\epsilon_{\text{LJ}} = 1.2$, density $\bar{\rho} = 0.864$, and kinematic viscosity $\bar{\nu} = 2.8$. The lattice spacing $\bar{a}$ is set to unity, which is roughly identical to the bond length; this is necessary to resolve the hydrodynamic interactions on small length scales with sufficient accuracy. In order to match the value of the monomer diffusion coefficient ($D_0 = k_{\text{B}}T/\zeta_{\text{eff}}$, where ζ_{eff} is the effective friction coefficient) obtained from LB simulations to the known value from MD simulations, Ahlrichs and Dünweg [7] have shown that the effective friction coefficient ζ_{eff} can be determined from the "bare" friction coefficient ζ_{bare} in the LB simulation via

$$\frac{1}{\zeta_{\text{eff}}} = \frac{1}{\zeta_{\text{bare}}} + \frac{1}{g\eta a}, \tag{4.1}$$

where $g \approx 25$, and $\eta = \rho\nu$. Since the MD simulations lead to $\bar{D}_0 = 0.076$, $\bar{\zeta}_{\text{bare}}$ was set to 20.8 to obtain the desired ζ_{eff} value. The values of the FENE spring potential parameters are $\bar{H} = 7$ and $\bar{R}_0 = 2$. The time step size for the polymer (the MD part of the simulations) is set to $\Delta\bar{t} = 0.01$. The value of the time step that updates the fluid should be chosen in a way such that the LB variables n_i do not become negative too often. Here, we choose $\Delta\bar{\tau} = 0.02$, where such a case rarely occurred during the observation time. It is important to mention another free input parameter which governs the time scale for the evolution of hydrodynamic interactions, known as the Schmidt number $Sc = \nu/D_0$. This parameter can be set arbitrarily in the LB method by choosing ν and D_0 (which can be tuned by choosing ζ_{bare}) accordingly. Ideally, the value of Sc should be chosen such that hydrodynamic interaction evolves much faster than the diffusion of a monomer. In our case, we have $Sc \approx 32$, which has been shown to result in Zimm-like behavior [7; 97].

For the LB simulations, the polymer chain moves within a cubic box of length L with periodic boundary conditions, while it is drifting freely in an infinite medium for the BD simulations. In order to accurately compare various properties between the two systems, one must understand the effects of the box length L on any observable of interest in the LB simulations. Thus it is essential to only compare quantities under identical condition (i. e. independent of the box length). Hence various box lengths L ranging from 10 to 35 Lennard-Jones units were investigated.

4.2.2 Mapping the lattice Boltzmann parameters onto Brownian dynamics parameters

In other to compare the results between LB and BD simulations, one has to take into account that the two methods use different unit systems for length and time; therefore the ratios between the elementary scales of the two methods are needed. These ratios can be evaluated by equating the dimensional forms for the FENE spring potentials in the two models, resulting in

$$\frac{\sigma}{l_H} = \left(\frac{\bar{k}_{\text{FENE}}\epsilon}{k_{\text{B}}T}\right)^{1/2}, \tag{4.2}$$

$$\frac{\tau}{\lambda_H} = \frac{4\bar{k}_{\text{FENE}}}{\bar{\zeta}_{\text{eff}}}. \tag{4.3}$$

The value of the maximum stretching length of a spring in the BD model can then be determined from the above result, which leads to $R_0^* = 2(\sigma/l_H)$. Note that the bead friction coefficient ζ in the BD simulations has been set equal to ζ_{eff}.

Since Stokes' law is used in both models, the value of the dimensionless bead radius (h^*) in the BD model can be calculated from the input parameters of the LB model

$$h^* \sqrt{\pi} l_H = d = \frac{\zeta_{\text{eff}}}{6\pi\eta} = \frac{\bar{\zeta}_{\text{eff}}\sigma}{6\pi\bar{\eta}}, \tag{4.4}$$

or

$$h^* = \frac{\bar{\zeta}_{\text{eff}}}{6\pi^{3/2}\bar{\eta}} \left(\frac{\bar{k}_{\text{FENE}}\epsilon}{k_{\text{B}}T} \right)^{1/2}. \tag{4.5}$$

For the BD simulations, the time step size $\Delta t^* = 0.005$ was found to produce accurate results.

In the rest of the chapter, all properties will be presented in LB dimensionless units, regardless of the applied simulation method.

4.3 Results and discussion

4.3.1 Static properties

The mean square radius of gyration and the mean square end-to-end distance are given by

$$\begin{aligned} \left\langle R_{\text{g}}^2 \right\rangle &= \frac{1}{2N^2} \sum_{ij} \left\langle r_{ij}^2 \right\rangle, && (4.6) \\ \left\langle R_{\text{e}}^2 \right\rangle &= \left\langle (\mathbf{r}_N - \mathbf{r}_1)^2 \right\rangle && (4.7) \end{aligned}$$

with $r_{ij} = |\mathbf{r}_i - \mathbf{r}_j|$ being the inter-particle distance.

These two quantities are both related to the number of monomers by the expression

$$\left\langle R_{\text{g}}^2 \right\rangle \propto \left\langle R_{\text{e}}^2 \right\rangle \propto N^{2\nu}, \tag{4.8}$$

where ν is the Flory exponent. For a self-avoiding walk (SAW), the Flory exponent ν is 0.588 [65]. In principle, ν can be obtained from simulations, using the scaling law in Eq. 4.8. However, this method would require simulations for a wide range of

Table 4.1: Properties for a single chain of length $N = 32$ obtained from lattice Boltzmann simulations at various finite box lengths and Brownian dynamics simulations in infinite medium. [a] Exponent obtained by fitting a power law in the sub-diffusive scaling regime of the chain in Lattice Boltzmann simulations, $\bar{t} \in [20:80]$. [b] Exponent obtained from Lattice Boltzmann simulations without thermalization of all the kinetic modes.

	LB			BD
Box length L	10	15	25	∞
Time step	0.02	0.02	0.02	0.005
exponent ν	0.615 ± 0.005	0.617 ± 0.005	0.619 ± 0.005	0.619 ± 0.004
$\left\langle \bar{R}_{\mathrm{e}}^2 \right\rangle$	94.56 ± 1.20	100.05 ± 1.26	100.20 ± 1.28	99.22 ± 1.24
$\left\langle \bar{R}_{\mathrm{g}}^2 \right\rangle$	14.83 ± 0.10	15.31 ± 0.11	15.36 ± 0.11	15.25 ± 0.11
$\left\langle \bar{R}_{\mathrm{H}}^{-1} \right\rangle_\infty$	0.291 ± 0.0005	0.290 ± 0.0005	0.289 ± 0.0005	0.290 ± 0.0005
$\bar{g}_1$-exp.[a]	0.640 ± 0.0005	0.675 ± 0.0005	0.710 ± 0.0005	0.728 ± 0.0006
$\bar{g}_1$-exp.[a,b]	0.645 ± 0.0006	0.684 ± 0.0006	0.714 ± 0.0006	0.728 ± 0.0006
$\bar{g}_3$-exp.[a]	1.008 ± 0.0008	1.020 ± 0.0008	1.050 ± 0.0008	0.995 ± 0.0008
$\bar{D}_{\mathrm{CM}} \times 10^{-3}$	3.914	5.162	6.959	9.843
	$\pm 1 \times 10^{-3}$	$\pm 1 \times 10^{-3}$	$\pm 2 \times 10^{-3}$	$\pm 1 \times 10^{-2}$
$\bar{\tau}_{\mathrm{tr}}$(estimate)	631.36 ± 4.43	492.01 ± 3.56	368.51 ± 2.67	258.28 ± 1.87

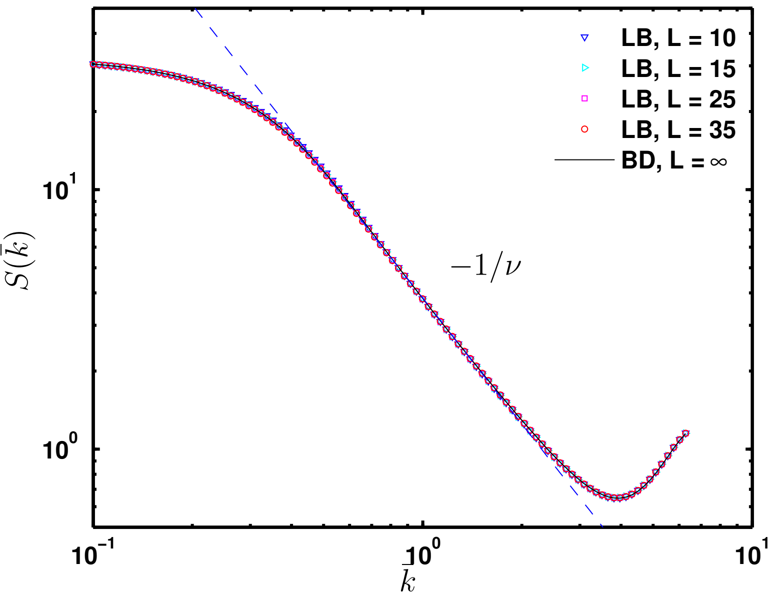

Figure 4.1: The static structure factor for the LB simulations (at various box lengths L) and the BD simulations ($L = \infty$) for a wide range of dimensionless wave vectors $\bar{k}$.

N values. Alternatively, one can use the static structure factor

$$\begin{aligned} S(k) &= \frac{1}{N}\sum_{ij}\langle\exp\left(i\mathbf{k}\cdot\mathbf{r}_{ij}\right)\rangle \\ &= \frac{1}{N}\sum_{ij}\left\langle\frac{\sin(kr_{ij})}{kr_{ij}}\right\rangle \end{aligned} \tag{4.9}$$

to obtain ν much more efficiently.

In the scaling regime $R_{\mathrm{g}}^{-1} \ll k \ll a_0$ (a_0 being a microscopic length of the order of the bond length), a power law relation between the static structure factor and the wave vector k holds:

$$S(k) \propto k^{-1/\nu}. \tag{4.10}$$

Figure 4.1 shows the static structure factor as a function of wave vector k for the LB simulations with the presence of thermalization of all modes, and the BD simulations. It can be clearly seen that the values of the static structure factor obtained from the LB simulations are exactly the same as those obtained from the BD simulations, indicating that they have the same static conformations. From Eq. 4.10, the value of ν can be extracted from the linear region of the log-log plot of $S(k)$ vs k. As expected, the values for ν obtained via this method are the same for both the LB and the BD simulations, as reported in Table 4.1. However, they are approximately 5% higher than the asymptotically correct value, which is a consequence of the finite chain length. The results for the mean square radius of gyration and the mean square end-to-end distance in Table 4.1 further confirm this agreement with regard to static conformations between the two methods. However, at small box length ($L = 10$), the results for these static properties for the LB method deviate from their asymptotic values. The discrepancy observed here always arises when the box length is too small compared to the chain size, where the chain is more likely to wrap over itself (overwrapping) due to spatial restriction and hence alter its static conformations. We also found that the two versions of LB thermalization ("stresses–only" vs "full" thermalization) yield identical results for the chain conformational statistics. In general, we only quote values obtained for full thermalization, unless indicated otherwise.

The hydrodynamic radius for a single chain in an infinite medium is given by

$$\left\langle \frac{1}{R_{\mathrm{H}}} \right\rangle_{\infty} = \frac{1}{N^2} \sum_{i \neq j} \left\langle \frac{1}{r_{ij}} \right\rangle . \tag{4.11}$$

For a chain in a finite box, as is the case here in the LB method, it has been shown that the hydrodynamic interactions of the chain with its periodic image effectively increases R_{H} [7; 53]. In order to account for this finite-size effect, a finite-size correction of order L^{-1} for most dynamic properties, resulting from the slow r^{-1} decay of hydrodynamic interactions, is required [7; 53]. The results for the infinite-box value $\langle R_{\mathrm{H}}^{-1} \rangle_{\infty}$ agree excellently with each other for all simulations (see Table 4.1). Since the overwrapping effect is more sensitive to large inter-particle distances, it turns out that the deviation in the inverse hydrodynamic radius is too small, for the range of box lengths used, for it to be distinguishable. As can be seen in Table 4.1, the deviation is more pronounced for the radius of gyration, and even more for the end-to-end distance.

4.3.2 Dynamic properties

According to dynamic scaling, the longest relaxation time τ_{Z} of the chain is, by order of magnitude, identical to the time that the chain needs to move its own size, i. e.

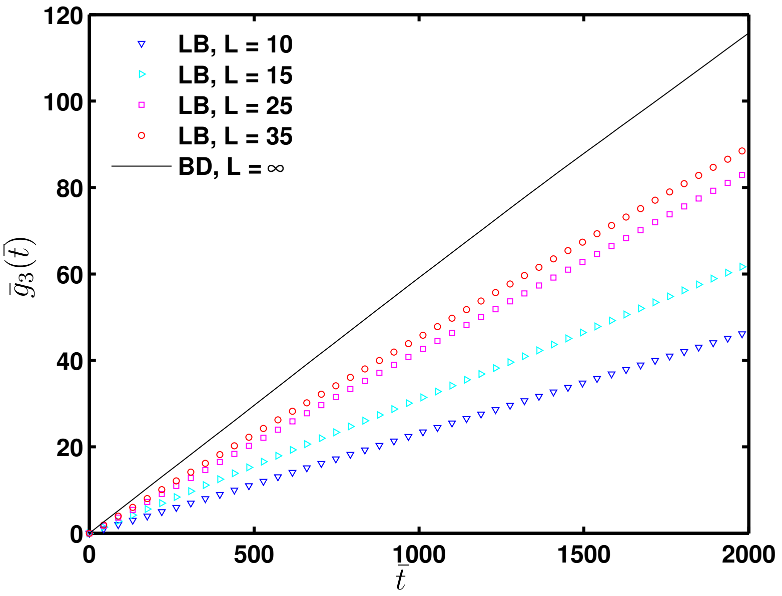

Figure 4.2: The dimensionless mean-square displacement $\bar{g}_3(\bar{t})$ of the chain's center of mass, Eq. 4.12.

$D_{\mathrm{CM}}\tau_{\mathrm{Z}} \sim R_{\mathrm{g}}^2$, where D_{CM} is the diffusion constant of the chain's center of mass. This leads to a dynamic scaling law $\tau_{\mathrm{Z}} \propto R_{\mathrm{g}}^z$, where z is the dynamic scaling exponent. For a chain with hydrodynamic interactions, this relaxation time is known as the Zimm time τ_{Z}. For this case, $D_{\mathrm{CM}} \propto R_{\mathrm{g}}^{-1}$ in the limit of long chains. This implies that $\tau_{\mathrm{Z}} \propto R_{\mathrm{g}}^3$, which gives a dynamic exponent of $z = 3$ for models with HI. For the Rouse model (i. e. chains without hydrodynamic interactions), where $D_{\mathrm{CM}} \propto N^{-1}$, one finds a dynamic exponent of $z = 2 + 1/\nu$. These quantities will be referred to in the discussion below.

The mean-square displacement of the chain's center of mass

$$g_3(t) = \left\langle (\mathbf{R}_{CM}(t_0 + t) - \mathbf{R}_{CM}(t_0))^2 \right\rangle \tag{4.12}$$

for both methods is depicted in Fig. 4.2. From the figure, it can be clearly seen that g_3 strongly depends on the box length L for the LB simulations. Moreover, they seem to converge to the value predicted by the BD simulations ($L = \infty$) in the limit of large L. Effects of thermalization of the kinetic modes in LB simulations on this property will be discussed subsequently. The chain's center of mass diffusion constant D_{CM} can be determined by the slope of the g_3 vs t curve, where the relationship

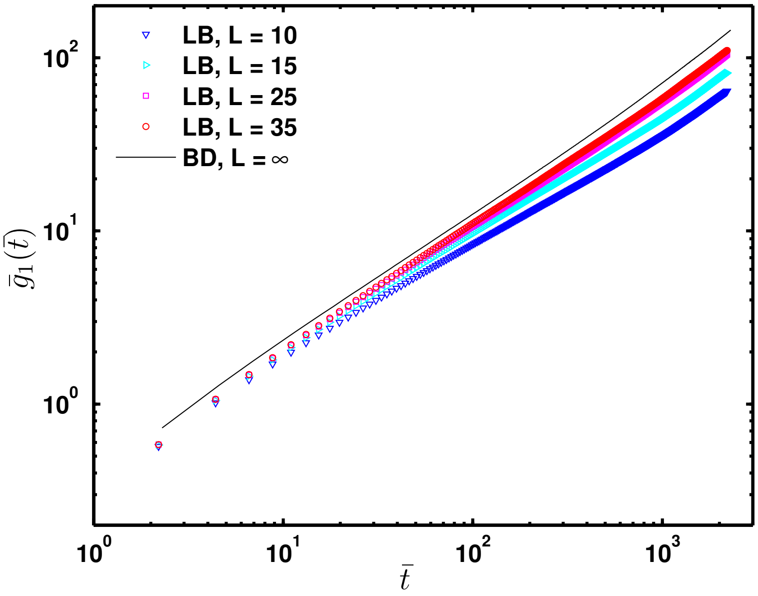

Figure 4.3: The dimensionless mean-square displacement $\bar{g}_1(\bar{t})$ of the central monomer, Eq. 4.13.

$g_3(t) = 6D_{\mathrm{CM}}t$ holds. By fitting a power law to the simulation data, we obtain the exponents and the diffusion constants shown in Table 4.1. These exponents support the prediction of simple diffusive behavior (t^1). Theoretically, one would expect that two diffusive regimes exist: On the one hand, there should be a short-time diffusive regime, corresponding to time scales well below the Zimm time, $t \ll \tau_{\mathrm{Z}}$, but also well above the ballistic regime, $t \gg \tau_0$; note that $\tau_0 > 0$ only in the LB case, since the BD equation of motion is overdamped. On the other hand, there should be free diffusion for times $t \gg \tau_{\mathrm{Z}}$. Both these regimes exhibit t^1 behavior, but with different prefactors, with a smooth crossover around the Zimm time [62; 63; 128]. In principle these two different diffusion constants can be obtained via fits to the corresponding regimes. In practice, however, it turns out that the values are very close to each other, and hence the crossover is very smooth [62; 63; 128]. Therefore its unambiguous identification is very difficult, i. e. impossible within the resolution of our data.

The mean-square displacement of a single monomer i is given by

$$g_1(t) = \left\langle \left(\mathbf{r}_i(t_0 + t) - \mathbf{r}_i(t_0)\right)^2 \right\rangle . \tag{4.13}$$

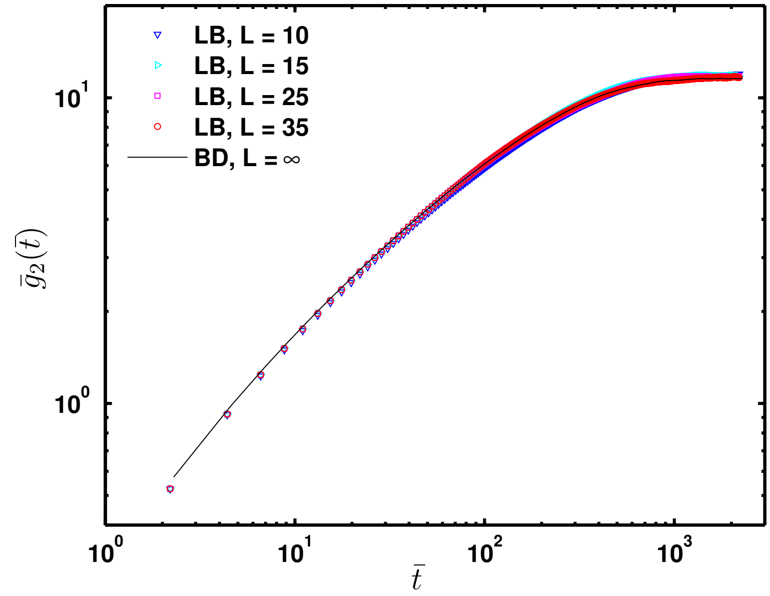

Figure 4.4: The dimensionless mean-square displacement $\bar{g}_2(\bar{t})$ of the central monomer in the chain's center of mass system, Eq. 4.15.

Here, only the two innermost monomers near the center of the chain are evaluated to eliminate end effects; the results are plotted in Fig. 4.3. The values of g_1 behave similarly to those of g_3. In the sub-diffusive time regime, corresponding to the short-time diffusive regime for g_3, here evaluated between $\bar{t} = 20$ and 80, the scaling behavior $g_1(t) \propto t^{2/z}$ is predicted [50]. The corresponding exponents obtained from a power-law fit are listed in Table 4.1 and indicate a value of $z = 2.75$ as $L \to \infty$. Regardless of the finite-size corrections due to the box length and the effects of thermalization, these values clearly favor the Zimm model compared to the Rouse model, which predicts $g_1(t) \propto t^{0.54}$. Moreover, the data also indicate that full thermalization does indeed improve the quality of the results, in the sense that it brings the effective z value somewhat closer to the known asymptotic value 2/3.

Figure 4.4 shows the mean-square displacement of a single monomer in the center of mass system (i. e. the two innermost monomers to eliminate end effects)

$$\begin{aligned} g_2(t) &= \langle([\mathbf{r}_i(t_0+t) - \mathbf{R}_{\mathrm{CM}}(t_0+t)] \\ &- [\mathbf{r}_i(t_0) - \mathbf{R}_{\mathrm{CM}}(t_0)])^2\rangle. \end{aligned} \tag{4.14}$$

Interestingly, when viewed within the center of mass system, all the results lie on top of each other, regardless of the box length L. This result also holds for LB simulations without full thermalization. This shows that the global center-of-mass motion of the chain is actually the primary contribution to the deviations between LB and BD results. In the data of Fig. 4.4 this contribution is suppressed: In terms of Rouse modes, only the internal modes remain. For these modes, however, it has been shown [7] that the HI with the periodic images is much weaker (essentially of dipolar nature), while the leading-order r^{-1} HI cancels out. Therefore, the corresponding finite-size effect scales as L^{-3} instead of L^{-1}, and this is so small that it is invisible in Fig. 4.4.

Theoretically, these data can also be used for estimating the Zimm time as the time where the crossover to the long-time plateau occurs. However, the crossover is quite extended and smooth, making it difficult to extract. We therefore estimated the Zimm time via

$$\tau_{\mathrm{Z}} = \frac{\left\langle R_{\mathrm{g}}^2 \right\rangle}{6 D_{\mathrm{CM}}}. \tag{4.15}$$

Strictly speaking, this definition is only valid for a single chain in an infinite medium, where there is no finite box size effect. In the presence of finite box size, it becomes the definition for the *translational* time (τ_{tr}) rather than the Zimm time: The former is subject to an L^{-1} finite-size effect, due to the strong L-dependence of D_{CM}, while the latter, being defined via the relaxation of internal modes, is only subject to an L^{-3} size effect, as discussed above. The translational times obtained from Eq. 4.15 (as shown in Table 4.1) are indeed different for different box lengths L, as expected. Conversely, the results displayed in Fig. 4.4 indicate that the systems with different box sizes have (essentially) all the same (internal-mode) Zimm time, since their data all lie on top of each other.

Next, we focus on the leading order L^{-1} finite size correction for the long-time diffusion constant of the chain's center of mass, D_{CM}. In principle, a plot of D_{CM} vs L^{-1} should give a straight line for large L, and an extrapolation to the limit $L \to \infty$ should yield the same value as predicted by the BD simulations. Figure 4.5 shows the values of D_{CM} for the LB simulations with and without thermalization of the kinetic modes at various box lengths L plotted together with the value obtained from the BD simulation at $L = \infty$. It is worth mentioning that the BD value of D_{CM} can be obtained from the mean square displacement of the chain center of mass or via Fixman's expression [62]. The latter method has been shown to produce a

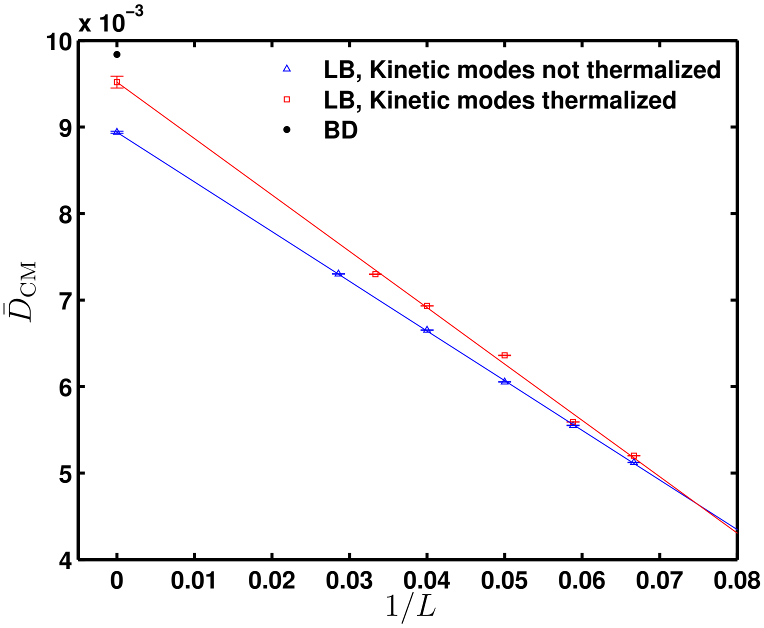

Figure 4.5: The dimensionless long time diffusion constant for the center of mass at various box lengths L.

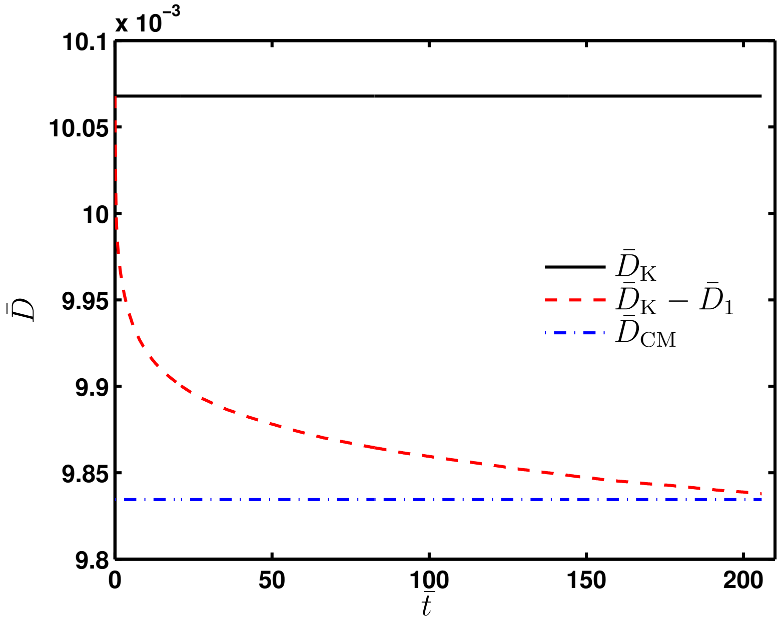

Figure 4.6: The long time diffusion constant for BD simulations obtained from the mean square displacement of the chain center of mass ($\bar{D}_{\mathrm{CM}}$) and from the velocity autocorrelation function via Fixman's expression ($\bar{D}_{\mathrm{K}} - \bar{D}_1$).

much more reliable result and is easier to carry out [128]. According to Fixman [62], the long-time diffusion coefficient D_{CM} can be obtained from the difference between its value at short times D_{K} and the contributions from intramolecular dynamic correlations D_1 (i.e. $D_{\mathrm{CM}} = D_{\mathrm{K}} - D_1$), where D_{K} and D_1 are given by [105; 195],

$$D_{\mathrm{K}} = \frac{D_0}{N} + \frac{k_{\mathrm{B}}T}{6\pi\eta_{\mathrm{s}}}\frac{1}{R_{\mathrm{H}}}, \tag{4.16}$$

$$D_1 = \frac{1}{3N^2}\int_0^{\infty} \langle A_i(t)A_i(0)\rangle \, dt. \tag{4.17}$$

Here, η_{s} is the solvent viscosity, and $A_i = (\sum_{\mu} D_{\mu\nu ij}F_{\nu j})/4$ is the velocity of the chain's center of mass, where $\sum_{\mu} D_{\mu\nu ij}$ and $F_{\nu j}$ are the diffusion tensor and the matrix of total body force, respectively.

Figure 4.6 shows the values of D_{CM} obtained from BD simulations for both methods and the results are in excellent agreement with each other. For the LB simulations without thermalization of the kinetic modes, the value of D_{CM} at the asymptotic limit $L = \infty$ is different from that predicted by the BD simulations by about 9.5%. However, when all the kinetic modes in the LB simulations have been thermalized, the deviation in D_{CM} reduces to 3%. This result clearly indicates that it is very important to thermalize all the kinetic modes in order to obtain correct values for dynamic properties.

The reason for the remaining small discrepancy between LB and BD is not completely clear, since there are numerous possible sources. Firstly, it should be noted that the underlying equations of motion are quite different: LB works with inertia, while BD employs overdamped dynamics. This results in different Schmidt numbers Sc and different Mach numbers Ma, the latter being defined as the ratio of the flow velocity to the speed of sound: Both are finite in the LB method, while in the BD case they are strictly infinite (Sc) and zero (Ma), respectively. Furthermore, the shape of the HI function at small interparticle distances is somewhat different for the two methods: In the BD case, we employ the RPY tensor, while the nearest-neighbor interpolation for LB results in a short-range HI that differs somewhat from the RPY tensor (see also the discussion in Ref. [Dünweg and Ladd]). Finally, it should be noted that the value of the constant g in Eq. 4.1, which is crucial for the mapping between the LB friction parameter ζ_{bare} and the BD friction ζ_{eff}, is only known with some numerical inaccuracy. For highly accurate mappings, it is also necessary to

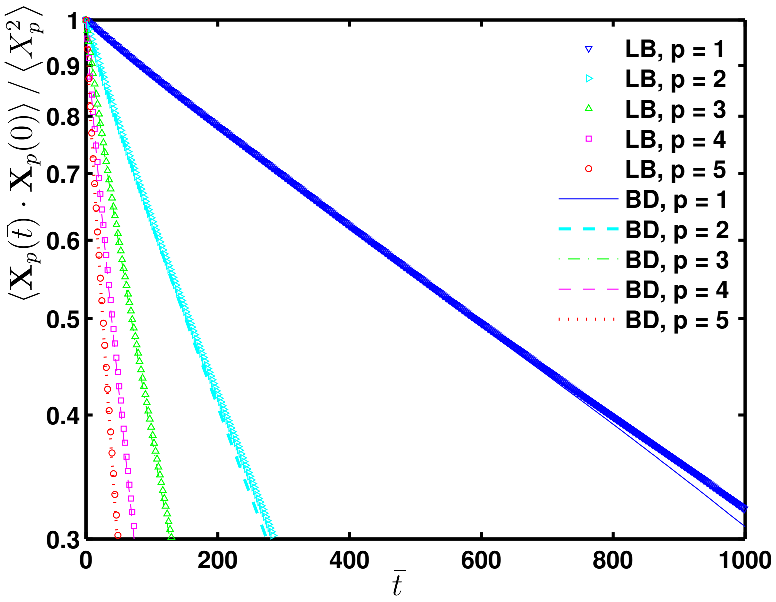

Figure 4.7: Normalized autocorrelation function of the first 5 Rouse modes $\mathbf{X}_p$ (Eq. 4.19) for LB simulations at $L = 25$ and BD simulations at $L \to \infty$.

include a finite-size correction in the definition of g [Dünweg and Ladd]; this was not done in the present study.

In order to examine whether the thermalization of the kinetic modes is also important for the internal modes, we have performed a Rouse mode analysis. The Rouse modes for a discrete chain are defined as [7; 109]

$$\mathbf{X}_p = \frac{1}{N} \sum_{n=1}^{N} \mathbf{r}_n \cos \left[\frac{p\pi}{N} \left(n - \frac{1}{2} \right) \right] \tag{4.18}$$

for $p = 1, 2, \ldots, N-1$.

Within the approximation of the Zimm model, the autocorrelation function of the modes should decay exponentially [50]

$$\frac{\langle \mathbf{X}_p(t_0 + t) \cdot \mathbf{X}_p(t) \rangle}{\langle \mathbf{X}_p^2 \rangle} = \exp\left(-\frac{t}{\tau_p} \right), \tag{4.19}$$

where τ_p is the relaxation of the p-th mode. To validate our Rouse mode analysis routine, we have carried out extensive simulations for a (Gaussian) Rouse chain of $N = 8$ in the absence of HI and EV; the results for τ_p are in excellent agreement

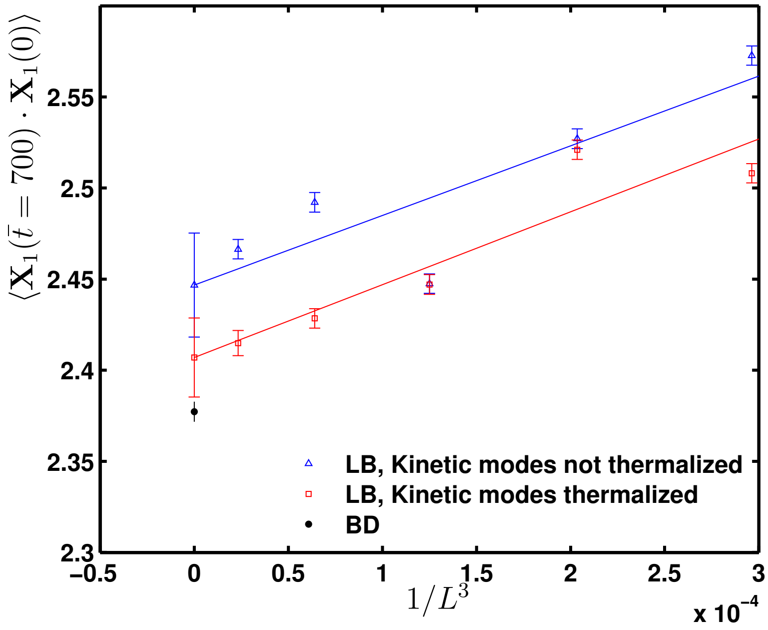

Figure 4.8: The autocorrelation function for the first Rouse mode $\mathbf{X}_1$ at a finite time value of $\bar{t} = 700$ for LB simulations at various box lengths L and BD simulations at $L \to \infty$.

with the analytical predictions [50]. Figure 4.7 shows the normalized autocorrelation function for $p = 1, 2, \ldots, 5$ for the LB model with box length $L = 25$, and the BD model. For nonzero times, there is a small deviation between LB and BD, the latter exhibiting again a slightly faster dynamics. This deviation systematically becomes smaller upon increasing the mode index p. Since high mode index means essentially relaxation on a rather small length scale, it is tempting to attribute the deviation to the finite propagation of HI in the LB model, i. e. to retardation effects which are more important on large length scales than on small ones. Nevertheless, this hypothesis is not proven.

In Ref. [6] it was shown that the autocorrelation function is only subject to an L^{-3} finite size effect, in contrast to the usual L^{-1} behavior. Figure 4.8 shows the value of the autocorrelation function of the first Rouse mode $\mathbf{X}_1$ at a fixed finite time $\bar{t} = 700$, for LB simulations at various box lengths L and BD simulations at $L = \infty$. Within our numerical resolution, the data indeed confirm this L^{-3} finite size effect, both with and without thermalization of the kinetic modes. Furthermore, they demonstrate again that thermalization of all the kinetic modes in LB simulations improves the accuracy of the dynamic properties and brings them closer to the BD prediction: The deviation in the extrapolated limit $L \to \infty$ is reduced from 3% down to 2%. The reasons for the remaining discrepancies are probably of the same nature as in the case of D_{CM}.

We have also evaluated the dynamic structure factor, which is defined as

$$S(k,t) = \frac{1}{N} \sum_{ij} \left\langle \exp\left(i\mathbf{k} \cdot [\mathbf{r}_i(t) - \mathbf{r}_j(0)]\right) \right\rangle . \tag{4.20}$$

When both the wave number and time are in the scaling regime (i. e. $R_{\mathrm{g}}^{-1} \ll k \ll a_0^{-1}$ and $\tau_0 \ll t \ll \tau_{\mathrm{Z}}$), $S(k,t)$ is predicted [50] to exhibit the scaling behavior

$$S(k,t) = S(k,0) f(k^z t). \tag{4.21}$$

A plot of $S(k,t)k^{1/\nu}$ against $(k^z t)^{2/z}$ should collapse to a single curve [7]. The results for both methods are shown in Fig. 4.9. The data were restricted to the scaling regime $20 < t < 80$ and $0.7 < k < 1.5$. These ranges were obtained from the single monomer mean-square displacement, Fig. 4.4, and from the static structure factor, Fig. 4.1, respectively. Here, we particularly focus on adjusting the exponent z such that it would produce the best total data collapse for a chain in an infinite medium (i. e. in the BD model). Obviously, the results from the simulations show Zimm-like rather than Rouse-like behavior. Even though we have suppressed the finite box size effect, a dynamic exponent of $z = 2.75$ yields the best data collapse, which is somewhat smaller than the correct asymptotic one. This result is also consistent with the value of z obtained earlier via the exponent of g_1 in the sub-diffusive scaling regime (i. e. $2/z = 0.728$). The deviation from the asymptotic value is due to the finite chain size used here, and one can expect $z = 3$ only in the long chain limit $N \to \infty$.

More detailed comparisons of the structure factor $S(\bar{k}, \bar{t})$ are shown in Fig. 4.10 ($\bar{k}$ dependence at constant time), Fig. 4.11 ($\bar{k}$ dependence for the relative deviation in the structure factor $S(\bar{k}, \bar{t})$ from BD simulations ((LB-BD)/BD) at constant time), and Fig. 4.12 (time dependence for the *normalized* structure factor $S(\bar{k}, \bar{t})/S(\bar{k}, 0)$ at constant $\bar{k}$).

Figure 4.10 shows the structure factor for BD simulations for a wide range of $\bar{k}$ at three different times and the data clearly indicate that the structure factor decays rapidly with time. Figure 4.11 shows the relative deviation in the structure factor

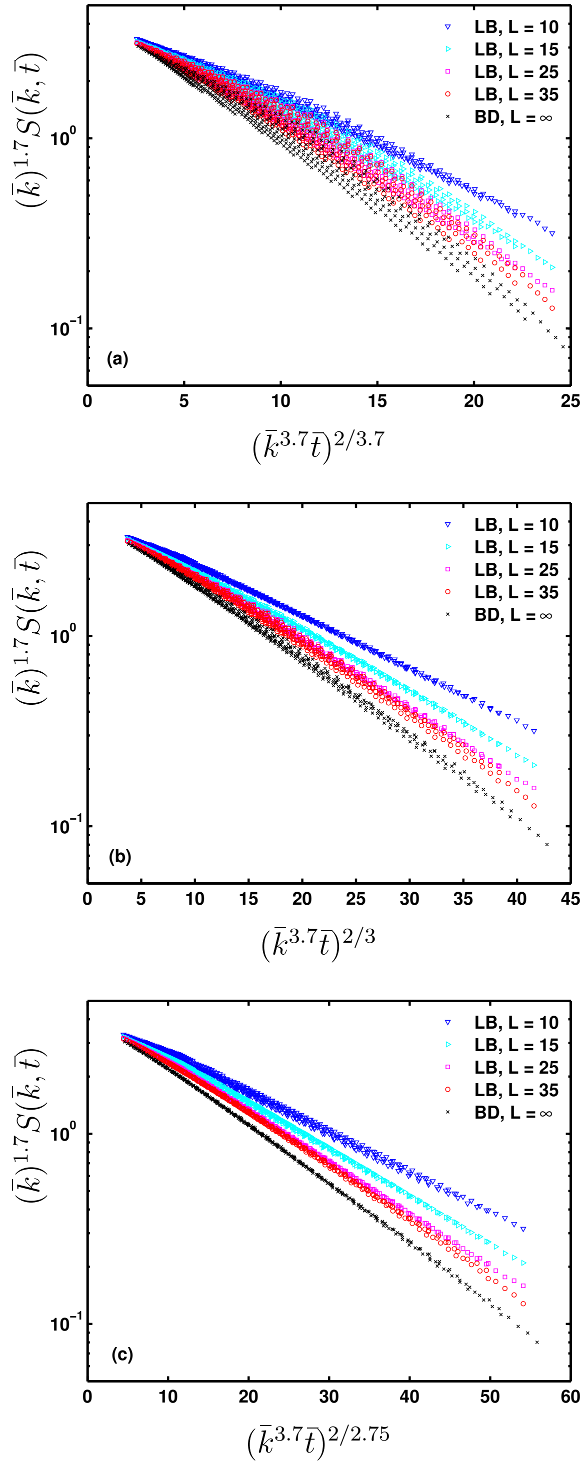

Figure 4.9: Scaling plot of the dynamic structure factor for (a) Rouse scaling ($z = 3.7$, top), (b) asymptotic Zimm scaling ($z = 3$, center), and (c) $z = 2.75$ (bottom), which produces the best collapse.

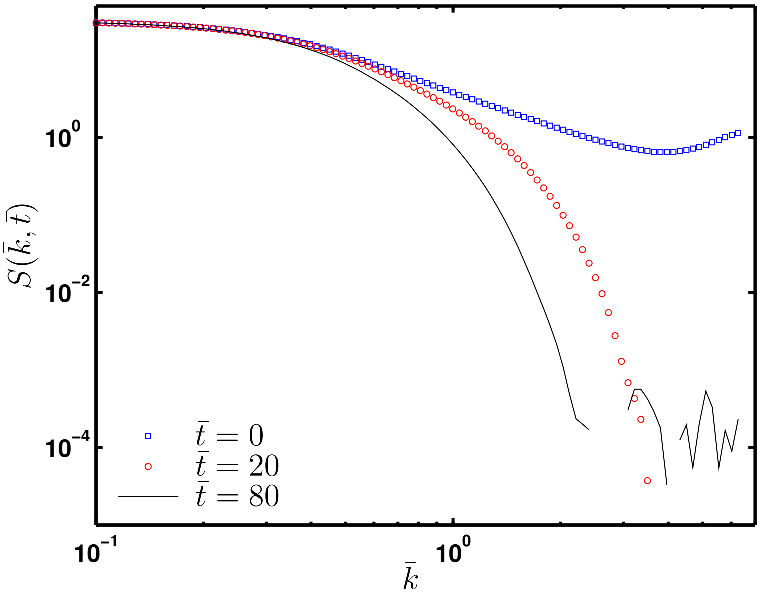

Figure 4.10: The dynamic structure factor $\bar{S}(\bar{k}, \bar{t})$ for the BD simulations ($L = \infty$) at three different times.

for the LB simulations as a function of $\bar{k}$ at three different times. Figure 4.11(a) shows that the relative deviation for various box lengths L for the LB model at $\bar{t} = 0$ are very small (less than 1.5%), which means that they produce similar values for the static structure factor. However, for box length $L = 10$, some deviation in the static conformation can be spotted via the values of the end-to-end distance or the radius of gyration (see Table 4.1). For $\bar{t} \neq 0$, the relative deviation in the structure factor increases with increasing $\bar{k}$. The deviation is larger for smaller box length L and this is attributed to the L^{-1} finite-size correction of the dynamic properties. The scale used in Fig. 4.11(a), (b), and (c) highlights the relative deviation for the LB model (at various box lengths L) from the BD model at three different times. The discontinuity observed in the relative deviation, which occurs roughly at $\bar{k} = 4$ for $\bar{t} = 20$ and at $\bar{k} = 2$ for $\bar{t} = 80$ arises as a result of the statistical noises in the structure factor, that has completely decayed to zero beyond these values of $\bar{k}$. As expected, the LB results seem to approach the BD data as L is increased. A similar feature is also observed in the normalized structure factor $S(\bar{k}, \bar{t})/S(\bar{k}, 0)$ for three different $\bar{k}$ values shown in Fig. 4.12.

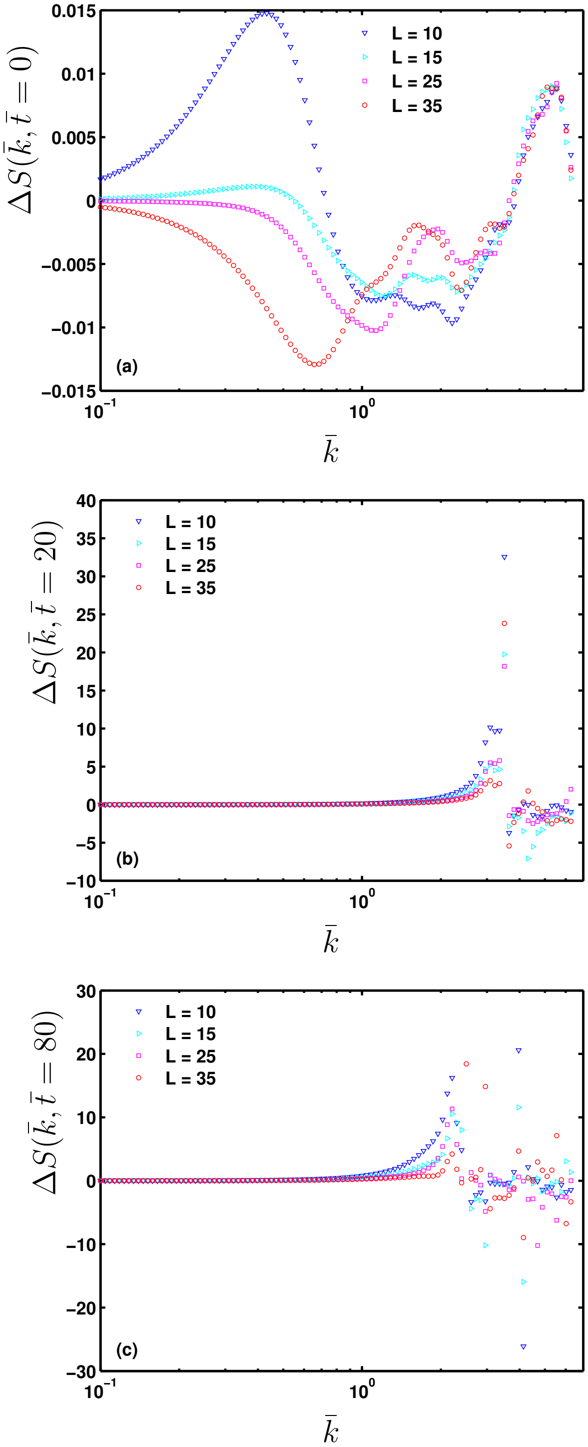

Figure 4.11: The relative deviation in the dynamic structure factor $\Delta S(\bar{k},\bar{t})$ ((LB-BD)/BD) for the LB simulations (at various box lengths L) from the BD simulations ($L=\infty$) at (a) $\bar{t}=0$ (top), (b) $\bar{t}=20$ (center) and (c) $\bar{t}=80$ (bottom).

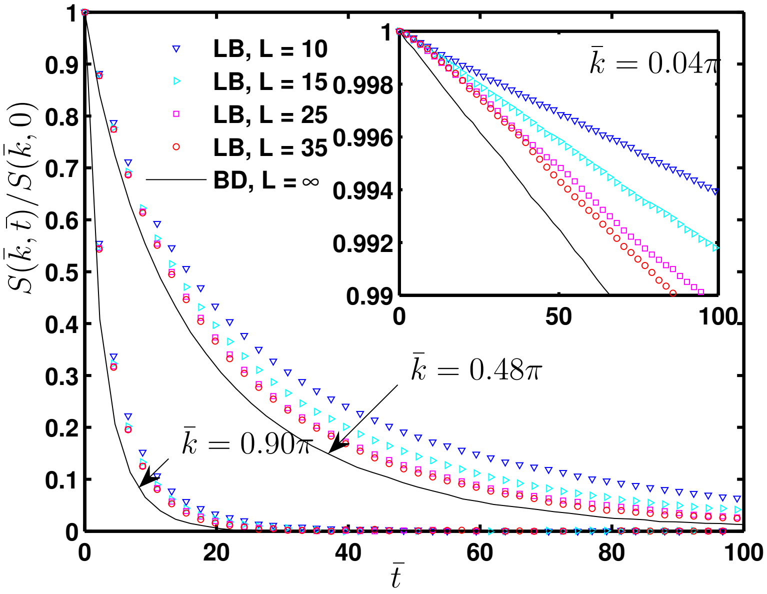

Figure 4.12: The evolution of the ratio of the dynamic structure factor at three different $\bar{k}$ values. Data for $\bar{k} = 0.04\pi$ is displayed in the inset.

4.3.3 Efficiency

For the ultra-dilute system considered here, the lattice Boltzmann part of the hybrid LB method uses up most of the computational resources as the CPU cost for the MD part for the polymer chain is negligible. Since the dynamic properties predicted by the LB model are subject to a finite-size correction of order L^{-1}, extrapolation is required to obtain these properties in the asymptotic limit $L \to \infty$. To perform this extrapolation, the results of at least three different box lengths for the LB model are required. Moreover, the box length should be large enough compared to the chain size such that it does not alter the static properties. The data displayed in Table 4.1 indicate that it is safe to choose L such that $\sqrt{\langle R_{\mathrm{e}}^2 \rangle}/L \leq 0.5$. The three different box lengths L chosen here are $\sqrt{\langle R_{\mathrm{e}}^2 \rangle}/L = 0.5, 0.4$, and 0.3. In this work, we set the total CPU time required for the LB simulations to be the sum of all the CPU times required to run 1000 MD time steps for each of the chosen box lengths. For BD, we take the CPU time needed to observe the system for the same time span in physical units. Each of the simulations performed for the CPU time comparison was run on an Itanium 2 processor of a 1.6 GHz SGI Altix server 3700. All the parameters used to carry out this comparison are the optimal values for both methods. Several

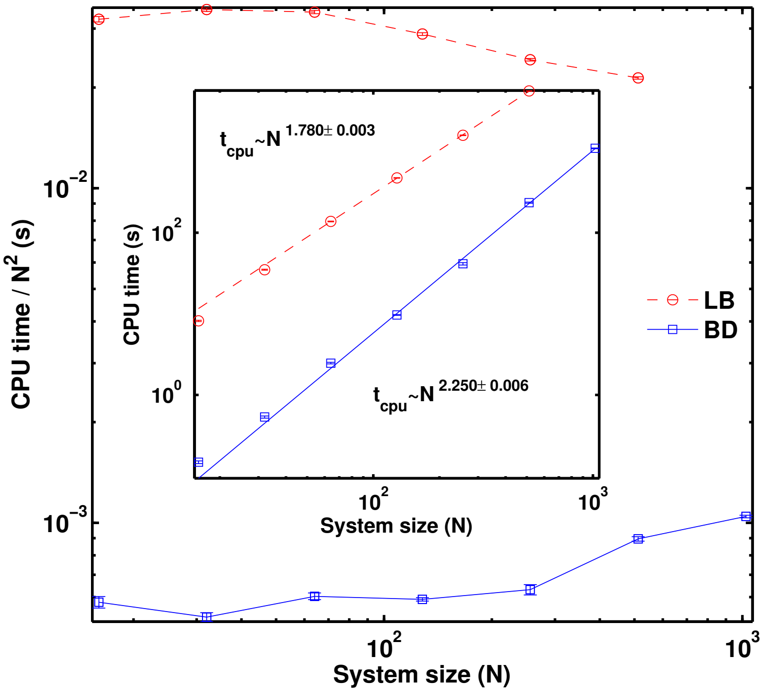

Figure 4.13: Comparison of the CPU time required by the LB and BD systems for the equivalent of 1000 time steps for a wide range of system sizes N.

chain sizes ranging from $N = 16$ to 1024 have been used to obtain the CPU cost for comparison. The results are shown in Fig. 4.13. For the LB method, it is clear that the CPU cost scales linearly with the number of particles, i. e. the number of grid points that the solvent lives on, or L^3. Since the ratio of $\sqrt{\langle R_e^2 \rangle}/L$ is kept constant, or $L \propto \sqrt{\langle R_e^2 \rangle} \propto N^\nu$, this leads to a CPU cost scaling as $N^{3\nu}$. This is indeed found in our benchmarks, see Fig. 4.13. Similarly, our data also confirm the predicted $N^{2.25}$ CPU cost scaling for BD. Though the LB exponent is lower than BD, the large prefactor ensures that the total CPU cost for LB is much more expensive compared to BD for the typical chain lengths used in the literature. It is only when the chain length is excessively large (i. e. N of the order of 10^6 or higher) that LB will become superior to BD for a single-chain system.

The situation completely changes if one studies a semi-dilute system instead, as has been done in Ref. [8]. Here one has a system of M chains of N monomers each, such that the total number of monomers is MN. Therefore the BD CPU cost scales as $(MN)^{2.25}$, while the LB CPU cost depends on the density. Within the blob picture of semidilute solutions, one views a chain as a sequence of "blobs", each comprising n monomers, and having size ξ, which can be viewed as the typical correlation length of density fluctuations, or the typical distance from which point on chain-chain interactions become important. Since the conformation statistics within the blob is that of a SAW, one has $\xi \sim an^{\nu}$, where a is the monomer size. The sequence of blobs forms a random walk, hence $R_e \sim \xi(N/n)^{1/2}$. This gives the minimum size of the simulation box, i. e. $L \sim \xi(N/n)^{1/2} \sim an^{\nu}(N/n)^{1/2} = aN^{\nu}(n/N)^{\nu-1/2}$, or $L^3 \sim a^3 N^{3\nu}(n/N)^{3\nu-3/2}$. We thus see that the CPU effort for the LB method is even slightly *decreased* by the factor $(n/N)^{3\nu-3/2}$ compared to the single-chain case at the same N, due to the shrinkage of the chains resulting from EV screening. In order to estimate the number of chains M, we note that the arrangement of blobs is space-filling, i. e. $L^3 \sim \xi^3 M(N/n) \sim a^3 M n^{3\nu}(N/n)$. Comparing this with the previous expression for L^3, one finds $M \sim (N/n)^{1/2}$. Therefore the BD effort, compared to the single-chain case, is increased by a factor of $M^{2.25} \sim (N/n)^{1.125}$. Taken together, this means that the ratio between LB effort and BD effort is changed by a factor of $\sim (N/n)^{3\nu+1.125-1.5} \approx (N/n)^{1.425}$ in favor of LB. For $N/n = 30$, which is needed as a minimum to resolve the Gaussian statistics of the chains as a whole, one obtains a factor of 130, which more or less compensates the two orders of magnitude seen in Fig. 4.13. Taking into account that for such a system the BD simulation would have to calculate the HI with the periodic images, e. g., via Ewald sums, which is much more complicated than the present single-chain simulation, one sees that for a semidilute solution clearly LB is more efficient, unless a "superfast" BD algorithm [16; 82; 174] is used. For the latter case, the answer is not yet known. The results of Ref. [35] indicate that LBM/MD may be favorable for a rather small number of monomers; however, this study was done under complete neglect of thermal fluctuations in the LBM part, which is clearly incorrect, as demonstrated theoretically in detail in Ref. [Dünweg and Ladd], and also corroborated by the present numerical results. Therefore, the estimate of the LB CPU effort given there is most probably too optimistic.

4.4 Conclusions

The results in this chapter has shown that Brownian dynamics simulations are capable of reproducing various properties predicted by a two-component lattice Boltzmann model (or vice versa). We have demonstrated how to obtain the input values for the BD simulations from the physical input parameters of the LB model such that both models would produce the same static and dynamic properties. For the LB model, most dynamic properties are subject to a finite-size correction of order L^{-1}. In addition to this, it is very important to thermalize all the kinetic modes in order to obtain the correct dynamic properties. Those results that are not affected by L^{-1} finite size effects, such as the mean square displacement in the center of mass system, or the Rouse mode autocorrelation function, agree very favorably with each other. For highly dilute systems where the simulation of a single chain is sufficient, BD is usually the method of choice, as it is much more efficient than the coupled LBM/MD approach, and finite box size effects are absent. The situation changes however in the semidilute case, where it is easy to estimate that BD will not be able to compete, unless "superfast" algorithms are used. Moreover, one should take into account that the hybrid LBM/MD algorithm is rather easily adaptable to complicated boundary conditions, and can even be applied to flows at high Reynolds numbers, where the fluid degrees of freedom become *intrinsically* important, and cannot be handled in terms of a Green's function.

Chapter 5

Homopolymer collapse

5.1 Introduction

The outcomes in Chapter 3 and 4 have strongly suggested that BD simulations of a bead-spring chain model is the most efficient mesoscopic simulation technique for studying a dilute polymer solution. Having validated the chosen model and simulation technique, BD simulations have been carried out to study the collapse dynamics of a single polymer chain in a poor solvent. As a starting point, a single homopolymer chain is used as a prototype to study the protein folding problem.

The lack of comparative studies between theory and experiments, to some extent, can be attributed to the difficulties observed in experiments. Experimental observation of the collapse transition is tricky because of the competition between intrachain collapse and interchain aggregation of chains upon quenching. Although the use of noninteracting polymer molecules, leading to a large aggregation time compared to collapse time, avoids one of the major hurdles in carrying out experiments, there have been only a handful of experimental studies on collapse kinetics [36; 78; 98; 143; 200; 208; 214]. However, the reliability of some of these experiments has been questioned [170].

Unavailability of accurate experimental data on polymer collapse and recent advances in computational resources have led researchers to carry out fairly accurate numerical computations. In fact, much of our understanding of collapse dynamics comes from numerical simulations [2; 26; 33; 103; 104; 123; 162; 163; 164; 197]. The development of numerical computations has also been motivated by, (i) the fact that experiments do not conclusively support any of the theories proposed in the literature, and (ii) there are widely divergent pictures of collapse and scaling laws predicted from the various theories. While a comprehensive review of the theories and simulation studies proposed so far in the literature is not given here, a brief overview of various developments in understanding the kinetics of homopolymer collapse is given below. Before doing so however, it is appropriate to first discuss the manner in which these different approaches model the role of the solvent.

The solvent is the seat of two molecular interactions that occur between solvent molecules and the monomers on a polymer chain. The first interaction, commonly referred to as *solvent quality*, which is responsible for the solution being classified as good, θ, or poor, arises due to the differing thermodynamic affinities that exist between solvent-solvent, solvent-monomer, and monomer-monomer molecular pairs. The second interaction, the so-called *hydrodynamic interaction* (HI) arises because solvent molecules propagate the motion of any one monomer through the ambient liquid to all the other monomers on the polymer chain through a disturbance in the velocity field. While it is essential to include the former interaction in some form in order to model polymer collapse, many theories and simulations neglect the occurrence of hydrodynamic interactions. Furthermore, each of these interactions are included in the different approaches in a variety of different ways. However, a few general remarks regarding aspects that are common to these differing treatments may be made.

The most common approach to the treatment of solvent quality effects is to ignore the explicit presence of solvent molecules, and instead treat them implicitly. This is true both in theoretical and computational models. Basically, it is assumed that the role of the solvent may be mimicked approximately through an effective interaction potential that acts between pairs of monomers. The alternative approach that has been adopted in some studies, in spite of the computational intensity that it entails, is to account explicitly for the presence of solvent molecules, and as a result, model all the three possible pair-wise intermolecular interactions. As will be clear from the summary of the literature below, in general, substantial differences arise between predictions of models that adopt the two different treatments.

With regard to the treatment of hydrodynamic interactions, once again two broadly differing approaches may be discerned depending on whether the solvent is treated implicitly or explicitly. The most common occurrence of the former approach is in analytical theories and in Brownian dynamics simulations, where the presence of explicit solvent molecules is neglected, and only the dynamics of a single polymer chain is examined. In this approach, the propagation of velocity disturbances in the solvent is assumed to occur instantaneously, leading effectively to a instantaneous coupling of the motion of all pairs of monomers on a polymer chain. Interestingly, within the explicit approach to the treatment of HI, the solvent molecules are treated either as point particles (i.e. the solvent is *structureless*), or as molecules with finite size and mass. In either of these explicit cases, hydrodynamic interactions between pairs of monomers on a polymer chain require a finite period of time to develop, as they are propagated from one monomer to the other through the medium of the solvent molecules.

The difference and similarities in the predictions of models with these different approaches to the treatment of solvent quality effects and HI are expanded on below. It is worthwhile noting that all possible combinations of methods to treat these effects have been explored in the literature, namely, (i) implicit solvent quality and implicit HI, (ii) implicit solvent quality and explicit HI, and (iii) explicit solvent quality and explicit HI. The treatment of solvent quality explicitly though the use of explicit solvent molecules automatically implies the explicit treatment of HI. This is the case for instance in explicit solvent molecular dynamics simulations.

A description of the kinetics of collapse with an implicit treatment of solvent quality was first attempted by de Gennes [45] in 1985, when he proposed a two-stage kinetic model for the collapse of a single chain. De Gennes in his pioneering work showed that after an abrupt change in the solvent quality (from good to poor), a single flexible chain quickly forms small blobs or clusters of collapsed monomers along the chain which he called "pearls". The chain then thickens and shortens with the growth of these blobs to form a sausage like structure before ultimately collapsing to the final compact globule state. It was predicted that the characteristic collapse time (τ) increases with increasing the quench depth (i.e. the temperature difference between the theta and final state). Following the work of de Gennes [45], various phenomenological models considering more subtle details, such as topological effects, have been developed to understand collapse kinetics [25; 75; 80; 107]. It is worth mentioning that these phenomenological models also concluded that the collapse takes place via a two stage mechanism as predicted originally by de Gennes [45]. Within the frame work of these models, scaling exponents for various properties which characterize the kinetics of collapse were estimated. For instance, scaling exponents for the growth of the average cluster size ($\langle S(t) \rangle$) with time (t) (defined as $\langle S(t) \rangle \sim t^z$) and the characteristic collapse time (τ) with the chain length (N) (define as $\tau \sim N^\gamma$) were obtained. (The predicted values of the exponents z and γ by various authors are given later in Table 5.2).

Besides these phenomenological models, Dawson and coworkers in a series of papers [115; 201; 202] developed a Gaussian self-consistent method using the Langevin equation with implicit solvent to understand the kinetics of collapse. They proposed a three stage collapse mechanism: first a rapid formation of small clusters, followed by a coarsening stage, and then a slow relaxation towards the compact globule. They also performed Brownian dynamics simulations with implicit solvent and without hydrodynamic interactions (HI) to obtain scaling exponents for various properties [26]. Pitard and Orland [161] developed an analytical theory based on the Langevin equation to study the scaling laws in the absence of HI. Pitard [160] further included HI using a preaveraged Oseen tensor in the theory developed earlier and concluded that HI speeds up the collapse rate.

Recent advances in computational resources has made it possible to perform computationally expensive but highly accurate and informative molecular dynamics (MD), Monte Carlo (MC) and Brownian dynamics (BD) simulations [2; 33; 103; 104; 123; 162; 163; 164; 197]. Tanaka and Mattice [197] performed atomistic molecular dynamic simulations and proposed that collapse is a three stage mechanism. However, Tanaka and Mattice [197] could not report any reliable scaling laws as statistically accurate results were difficult to obtain. Though models accounting for atomistic details would probably be the best for such problems, the intense computational requirement makes this techniques inappropriate even for small molecular weight polymer molecules.

The MC and MD simulation techniques have been used for most of the studies related to polymer collapse. The exception are Brownian dynamics simulations performed by Byrne et al. [26] and by Chang and Yethiraj [33]. Notably, except for MD simulations using an explicit solvent model, all others simulations techniques reported in the literature using MC, Gaussian self-consistent, and BD simulations have employed implicit-solvent methods for treating solvent quality, and the effect of HI is not accounted for [26; 33; 115; 201; 202]. It has been argued in the literature that averaging out solvent degrees of freedom to construct a monomer-monomer pair potential in the implicit solvent approach, as opposed to the multi-body interactions that arise naturally in the explicit solvent approach, can significantly affect polymer collapse dynamics and scaling laws [33; 162; 163; 164]. In one of the earliest attempts to incorporate the effect of explicit solvent, Polson and Zuckermann [163] investigated the effect of the degree of hydrophobicity of monomers on the collapse transition and found that collapse rate increases monotonically with increasing hydrophobicity. To reduce the computational cost, Polson and Zuckermann [163] considered a two dimensional system which was extended to three dimensional systems by Polson and Zuckermann [164] and Polson and Moore [162].

Chang and Yethiraj [33] in their work presented a comprehensive systematic comparison of the explicit solvent predictions from MD simulations with that of an implicit solvent model using BD simulations. The different systems were mapped onto each other by matching the solvent mediated potential in their MD model to the pair-wise two-body interaction in the BD model. Since Chang and Yethiraj [33] did not include hydrodynamic interactions in their BD model, they compared two extreme cases where, (i) either HI was completely neglected (BD simulation), or (ii) HI was included very accurately through a molecular model for the solvent (explicit solvent MD simulation). One of the striking features of this study was that while for the BD simulation, the collapse rate increases initially with increasing quench depth, but decreases at later times, MD simulations predicted a uniform increase in the collapse rate with quench depth. This difference was attributed to the fact that for the BD model, the polymer chains often get trapped in a metastable stage (a local minimum energy state) at large quench depths. No trapping was observed in the case of MD simulations. In addition, the collapse paths between BD simulations and MD simulations were also found to be different.

In order to overcome the computational intractability of explicit solvent based MD simulations, Reddy and Yethiraj [171] have recently proposed a new implicit solvent method in which the solvent is taken into account via a many-body interaction that depends on the solvent accessible surface area (SASA) of the monomers. They show that although there are quantitative differences, in the SASA model, just as in the explicit solvent MD case, homopolymer collapse at large quench depths occurs smoothly without any trapping in metastable states. Since HI effects are not included in the SASA model, their results suggest that the occurrence of trapping or otherwise is not related to the existence of HI, but rather to the manner in which solvent quality effects are included in the model.

More recently, a hybrid simulation technique with the synergy of MD simulations for polymer molecules and stochastic rotation dynamics for the solvent has been proposed to study the dynamical behavior of a polymer chain [103; 104; 123]. This technique ignores individual solvent molecules for the treatment of solvent quality effects, but it preserves the ability of the solvent to transmit the hydrodynamic force and hence, serves as an efficient algorithm to study the collapse dynamics of long polymer molecules. Kikuchi et al. [104] used this technique to show that inclusion of HI accelerates the collapse significantly. They also observed that independent of the presence of HI, polymer molecules always get trapped in local minimum energy states at large quench depth. The absence of explicit solvent-polymer molecular interactions in their work, or the use of shorter chains by Chang and Yethiraj [33] was cited as possible reasons for the discrepancy between their observations and the explicit solvent MD results of Chang and Yethiraj [33]. The collapse path was found to be independent of the presence of HI. Kikuchi et al. [104] also presented a simple scaling theory describing the processes responsible for the collapse kinetics. The scaling exponents predicted from the theory were found to be in good agreement with numerically computed values. In another study, Abrams et al. [2] modeled the collapsing chain as a Gaussian fractal structure and derived a new set of scaling laws for polymer collapse. These authors successfully compared their predicted time-dependent structure factor with values obtained from explicit solvent MD simulations. The predictions of the collapse path by Kikuchi et al. [104] were also in good agreement with that of Abrams et al. [2]. However, scaling exponents proposed by Kikuchi et al. [104] were different from those predicted by Abrams et al. [2] (see Table 5.2).

Given the conflicting nature of the mechanisms proposed in the various theories for the observed kinetics, the role of explicit versus implicit solvent models for the treatment of solvent quality effects and HI, and a virtual absence of experimental observations, the analysis of collapse dynamics using a different approach is a useful exercise. Brownian dynamics simulations with HI incorporated are often used in the literature to model dilute polymer solutions [119; 155], though their application to resolve the collapse problem has been somewhat limited. Brownian dynamic simulations have been shown to reproduce various experimentally observed features at equilibrium and in homogeneous flows [90; 96; 119; 120; 155; 166; 186; 194;

195]. Although the predictions of MD simulations incorporating detailed molecular interactions are much more informative, the Brownian dynamics simulation method offers an efficient and computationally cheaper way to simulate polymer collapse as it is computationally expensive to reach hydrodynamic time scales using MD simulations. This is because of the large number of solvent molecules, and the fact that the polymer molecule in MD simulations evolves slowly compared to the time scale of thermal fluctuations. Another major disadvantage of MD simulations is that it is virtually impossible to simulate polymers with Kuhn steps of order 10^3.

In this work, we use Brownian dynamics (BD) simulations of bead-spring chains to investigate the effect of hydrodynamic interactions, which has been shown to be very crucial in studying the collapse dynamics problem [33; 103; 104; 158]. By its very nature, BD simulations treat the solvent molecules implicitly both in terms of solvent quality effects, and with regard to hydrodynamic interactions.

5.2 The Model

As a preliminary check of our code, we have compared our results with those of Chang and Yethiraj [33], who carried our BD simulations without HI. In order to do this, we have employed the same EV force (derived from the full Lennard Jones potential) and FENE (finitely extensible nonlinear elastic) spring force used by Chang and Yethiraj [33]. However, as the length and the time scales used by Chang and Yethiraj [33] are different from the ones used here (σ, the Lennard-Jones parameter was used by them as the length scale, and $\tau_{\text{BD}} = \sigma^2/D_0$, with the monomeric diffusion coefficient $D_0 = k_{\text{B}}T/\zeta$, as the time scale), the EV and FENE forces have been rescaled by l_H and λ_H. In the rest of the chapter, the "*" superscript is used to indicate that the parameters are non-dimensionalized by l_H and λ_H.

The following forms of EV and attractive interaction for good and poor solvents, respectively, are used in our simulations:

$$V_{\mathrm{EV}}(r^*_{\mu\nu}) = \begin{cases} 4\epsilon^*_{\mathrm{LJ}} \left[\dfrac{(\sigma/l_H)^{12}}{{r^*_{\mu\nu}}^{12}} - \dfrac{(\sigma/l_H)^{6}}{{r^*_{\mu\nu}}^{6}} + \dfrac{1}{4} \right] & \text{for } r^*_{\mu\nu} \le 2^{1/6}(\sigma/l_H), \\ 0 & \text{for } r^*_{\mu\nu} > 2^{1/6}(\sigma/l_H) \end{cases} \tag{5.1}$$

$$V_{\mathrm{attr}}(r^*_{\mu\nu}) = \begin{cases} 4\epsilon^*_{\mathrm{LJ}} \left[\dfrac{(\sigma/l_H)^{12}}{{r^*_{\mu\nu}}^{12}} - \dfrac{(\sigma/l_H)^{6}}{{r^*_{\mu\nu}}^{6}} - c(R^*_c) \right] & \text{for } r^*_{\mu\nu} \le R^*_c, \\ 0 & \text{for } r^*_{\mu\nu} > R^*_c \end{cases} \tag{5.2}$$

where σ is the Lennard Jones parameters, $\epsilon^*_{\mathrm{LJ}} = \epsilon_{\mathrm{LJ}}/k_{\mathrm{B}}T$ is the strength of excluded volume interaction or quench depth, $r^*_{\mu\nu}$ is the distance from bead μ to bead ν. $R^*_c = 2.5(\sigma/l_H)$ is the cutoff radius and the function $c(R^*_c)$ is chosen such that the value of the potential is zero at the cutoff, i.e., $c(R^*_c) = [(\sigma/l_H)/R^*_c]^{12} - [(\sigma/l_H)/R^*_c]^6$.

The repulsive and attractive forces can be derived from the above potentials, and their dimensionless forms are given below:

$$\mathbf{F}^{\mathrm{LJ}^*}_{\mu,\,\mathrm{EV}}(\mathbf{r}^*_{\mu\nu}) = \begin{cases} 4\epsilon^*_{\mathrm{LJ}} \left[\dfrac{12(\sigma/l_H)^{12}}{{r^*_{\mu\nu}}^{14}} - \dfrac{6(\sigma/l_H)^{6}}{{r^*_{\mu\nu}}^{8}} \right] \mathbf{r}^*_{\mu\nu} & \text{for } r^*_{\mu\nu} \le 2^{1/6}(\sigma/l_H), \\ 0 & \text{for } r^*_{\mu\nu} > 2^{1/6}(\sigma/l_H) \end{cases} \tag{5.3}$$

$$\mathbf{F}^{\mathrm{LJ}^*}_{\mu,\,\mathrm{attr}}(\mathbf{r}^*_{\mu\nu}) = \begin{cases} 4\epsilon^*_{\mathrm{LJ}} \left[\dfrac{12(\sigma/l_H)^{12}}{{r^*_{\mu\nu}}^{14}} - \dfrac{6(\sigma/l_H)^{6}}{{r^*_{\mu\nu}}^{8}} \right] \mathbf{r}^*_{\mu\nu} & \text{for } r^*_{\mu\nu} \le R^*_c, \\ 0 & \text{for } r^*_{\mu\nu} > R^*_c \end{cases} \tag{5.4}$$

The dimensionless form of the FENE spring force is:

$$\mathbf{F}^{\mathrm{FENE}*}_{\nu} = \frac{\mathbf{Q}^*_{\nu}}{1 - (Q^*_{\nu}/Q^*_0)^2} \tag{5.5}$$

where $\mathbf{F}^{\mathrm{FENE}*}_{\nu}$ is the connecter force in a spring whose end-to-end vector is specified by the connector vector $\mathbf{Q}^*_{\nu} = \mathbf{r}^*_{\nu+1} - \mathbf{r}^*_{\nu}$. Q^*_{ν} is the dimensionless length of the spring and $Q^*_0 = 2(\sigma/l_H)$ is the dimensionless maximum stretchable length of a single spring. The two different length and time scales used here and in Ref. 33 are related to each other through the expressions $\sigma/l_H = \sqrt{7}$ and $\tau_{\mathrm{BD}}/\lambda_H = 28$, which can be derived by equating the dimensional form of the spring force used in Ref. 33 with the one used here.

The strength of hydrodynamic interactions are governed by the non-draining parameter h [88; 90; 194; 213; 215]. For bead-spring models with finitely extensible springs, $h \equiv \tilde{h}^* \sqrt{N}$, where $\tilde{h}^* = h^*/\chi$, with h^* being the hydrodynamic interaction parameter for chains with Hookean springs, and χ the spring parameter [166; 194]. For the FENE spring force law, $\chi^2 = Q_0^{*2}/(Q_0^{*2} + 5)$. In this work, two different values, $\tilde{h}^* = 0.25$ and 0.5, are used to account for HI. The quench depth values used here are chosen based on those values used by Chang and Yethiraj [33], i.e., $\epsilon_{\mathrm{LJ}}^* = 2.50, 2.61, 5.00$ and 10.00.

It is worth mentioning that our model is similar to the model used by Pitard [160], but the current model includes fluctuating HI rather than preaveraged HI. For good solvent simulations, initial configurations of chains are generated from the random walk distribution function. The chains are then brought to equilibrium in good solvent conditions by carrying out BD simulation for a period of $T_{\mathrm{eq}} = 15\tau_{1,\mathrm{R}}^*$, where $\tau_{1,\mathrm{R}}^* = 0.5 \sin^{-2}(\pi/2N)$ is the longest dimensionless Rouse relaxation time. Hydrodynamic interactions were turned off during the equilibrium simulations as HI does not affect the equilibrium distribution. Once the chain has equilibrated in a good solvent, it is suddenly quenched into the poor solvent by switching the potential from good to poor. For all the simulations, the time step size $\Delta t^* = 0.001$ is used which yielded a time converged solution. Property values are obtained from an ensemble average of 1000 statistically independent trajectories.

5.3 Results and discussion

In this section, we numerically investigate the dynamics of polymer collapse for different strengths of the attractive interaction or quench depths, ϵ_{LJ}^*. We monitor various observable quantities given below, which can be used to characterize the kinetics of collapse.

The mean square radius of gyration is defined as

$$\left\langle R_{\mathrm{g}}^{*2}(t^*) \right\rangle = \frac{1}{2N^2} \sum_{ij}^{N} \left\langle {r^*}_{ij}^{2} \right\rangle \tag{5.6}$$

The total collapse time τ is defined as the time taken for the radius of gyration of a chain to reach 99% of its total change in size during the transition period in which the chain is transformed from a coil to a compact globule. Mathematically, it is defined as

$$R^*_{\mathrm{g}}(\tau) = \frac{1}{100}(R^*_{\mathrm{g}}(0) - R^*_{\mathrm{g,\ eq}}) + R^*_{\mathrm{g,\ eq}}, \tag{5.7}$$

where $R^*_{\mathrm{g,\ eq}} = \sqrt{\langle R^{*2}_{\mathrm{g}} \rangle_{\mathrm{eq}}}$ is the root mean square equilibrium dimensionless radius of gyration in the collapsed state.

In addition to the above properties, the growth of the average cluster size with time $\langle S(t^*) \rangle$ is also recorded. In this work, we have employed two different definitions of average cluster size to investigate the effect of the definition of the average cluster size on this scaling law. These are the number average and the weighted average cluster size, respectively, and they are defined as

$$\langle S_n(t^*) \rangle = \frac{\sum_s sn(s)}{\sum_s n(s)}; \qquad \langle S_w(t^*) \rangle = \frac{\sum_s s^2 n(s)}{\sum_s sn(s)} \tag{5.8}$$

where s denotes the cluster size and $n(s)$ the number of clusters of size s. The algorithm proposed by Sevick et al. [181] is used here to compute the number of clusters and their size. The cluster size is determined by considering the non-nearest-neighbor beads to be a part of a cluster when the separation between two non-nearest-neighbors is less than D. Note that the separation at the minimum of the total potential (FENE+EV) is always smaller than the separation at the minimum of the Lennard Jones potential for the EV force alone. The presence of the FENE potential forces the minimum leftward. In addition, a bead cannot use the separation from either of its nearest-neighbors to register itself as part of a cluster, even if the neighboring bead already belongs to a cluster. It is worth mentioning that this latter restriction on the cluster definition is very crucial because the scaling exponent is very sensitive to the way a cluster is being defined as well as the overlapping distance D. In fact, it was found that if this restriction is neglected, then the average cluster size becomes so sensitive to the value of the overlapping distance D that no universal value for this exponent can be obtained. The values of the average cluster size at various values of D is also investigated to observe the sensitivity of this quantity to the overlapping distance D.

In order to establish the time step convergence and the accuracy of our BD simulations, we show results for the Flory exponents ν and the time evolution of the normalized mean square radius of gyration in the absence of HI, together with the results of Chang and Yethiraj [33], in Figs. 5.1 and 5.2, respectively. It is well

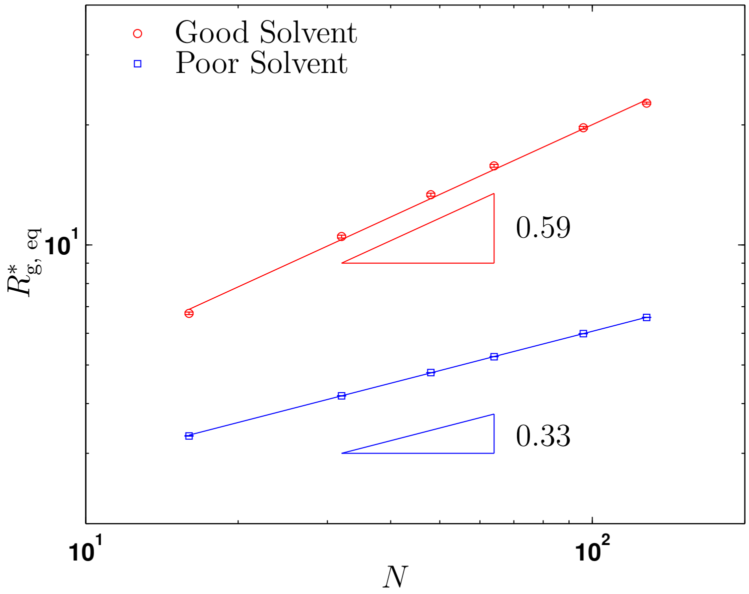

Figure 5.1: The equilibrium mean radius of gyration at various chain lengths in good and poor solvents. The values of the Flory exponents ν for good solvent and poor solvent are approximately 0.59 and 0.33, respectively.

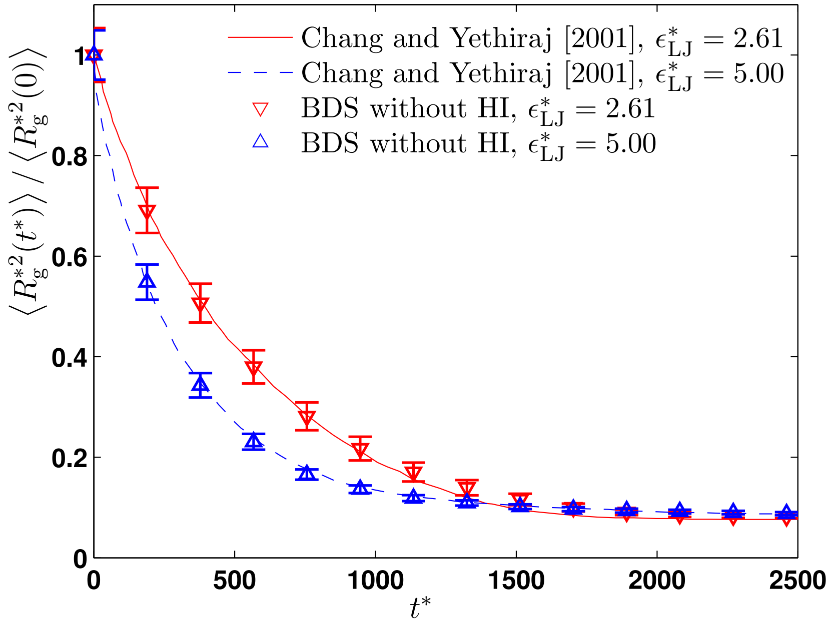

Figure 5.2: Variation of normalized mean square radius of gyration with time for a collapsing polymer chain, with $N = 128$, in the absence of HI, for two different quench depths, plotted together with the results reported by Chang and Yethiraj [33].

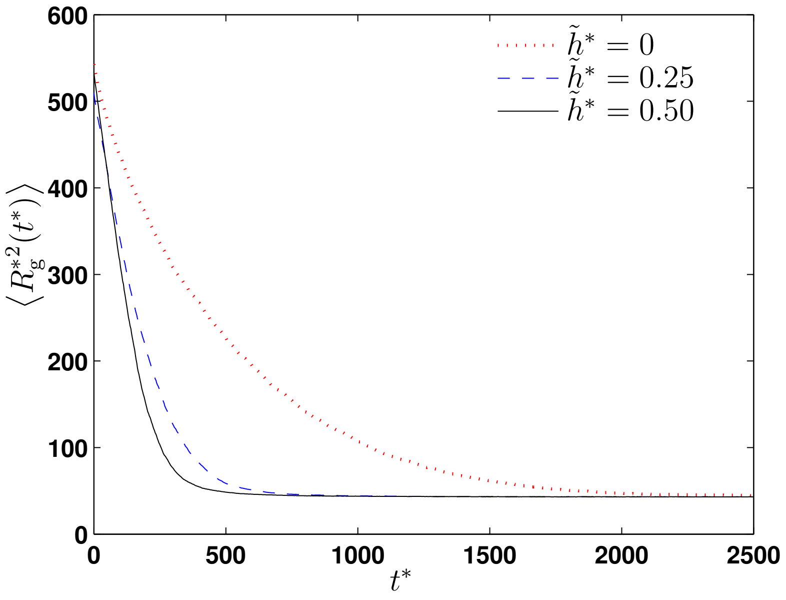

Figure 5.3: Variation of the mean square radius of gyration with time for a collapsing polymer chain, with $N = 128$, with and without HI at a low quench depth, $\epsilon^*_{\text{LJ}} = 2.61$.

known that the mean radius of gyration scales with the chain length as $R^*_g \sim N^\nu$ with $\nu = 0.588$ for a good solvent and $\nu = 0.33$ for a poor solvent [65]. Figure. 5.1 shows that the values 0.59 for good solvent and 0.33 for poor solvent obtained from our simulations are very close to the expected values. Figure 5.2 clearly shows that in the absence of HI, the predicted evolution of the radius of gyration in this work is in excellent agreement with that of Chang and Yethiraj [33] for both $\epsilon^*_{\text{LJ}} = 2.61$ and 5.00. The agreement also indicates that the mapping of the length and time scales between our bead-spring model to that used by Chang and Yethiraj [33] have been performed satisfactorily.

Figure. 5.3 shows the effect of hydrodynamic interactions on the evolution of the mean square radius of gyration at a low quench depth ($\epsilon^*_{\text{LJ}} = 2.61$) for $N = 128$. It is evident that HI plays an important role in accelerating the collapse. Increasing the strength of hydrodynamic interactions or the value of $\tilde{h}^*$, leads to a larger collapse rate and hence, a faster convergence to the final compact state. It can be seen that the time taken for the chain to reach its final equilibrium state reduces approximately four fold in the presence of HI. Molecular dynamics simulations also predict a similar qualitative behavior [33; 104].

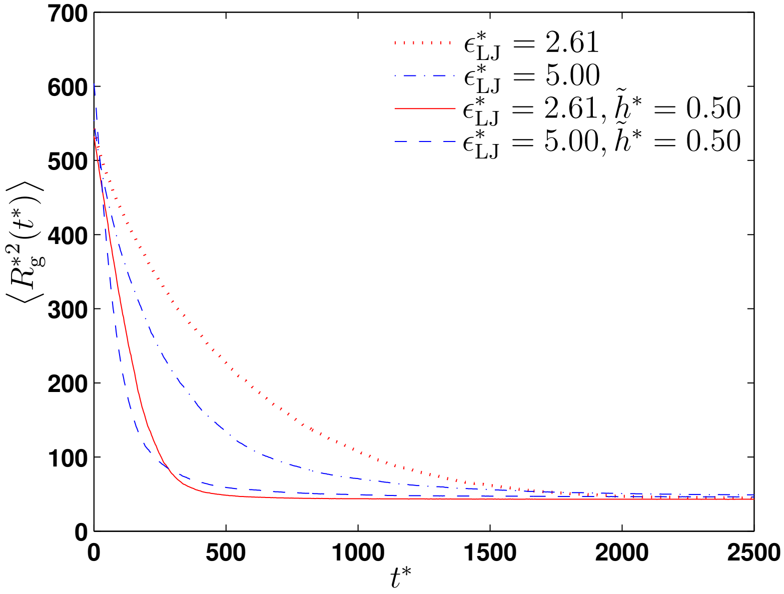

Figure 5.4: Variation of the mean square radius of gyration with time for a collapsing polymer chain, with $N = 128$, with and without HI for two different quench depths.

Increasing the value of the quench depth from 2.61 to 5 reveals some interesting results. As shown in Fig. 5.4, initially the collapse rate increases with increasing quench depth. However, at long times, the collapse becomes more gradual, leading to a lower collapse rate at high quench depth compared to that at low quench depth. We observed that this collapse behavior is independent of the presence of HI. Similar behavior was observed previously by Kikuchi et al. [104] using a hybrid approach which, as mentioned earlier, includes the solvent explicitly as point particles in order to propagate hydrodynamic interactions, but (as in BD simulations) treats the solvent implicitly with regard to solvent quality effects. Generally, one would expect that the radius of gyration for a chain at deep quench should be smaller than that of a chain at lower quench, since the stronger interaction would cause the chain to squeeze tighter. However, the chain at large quench gets trapped in a metastable state and stays there for a long time rather than approaching its final minimum energy state [33; 104]. Our simulations suggest that chains are trapped in one of the local energy minima irrespective of the presence of HI, in agreement with the earlier results of Kikuchi et al. [104].

The trapping phenomena occurs more frequently at high quench depth as shown in Fig. 5.5. Figure 5.5 compares the time evolution of the radius of gyration for

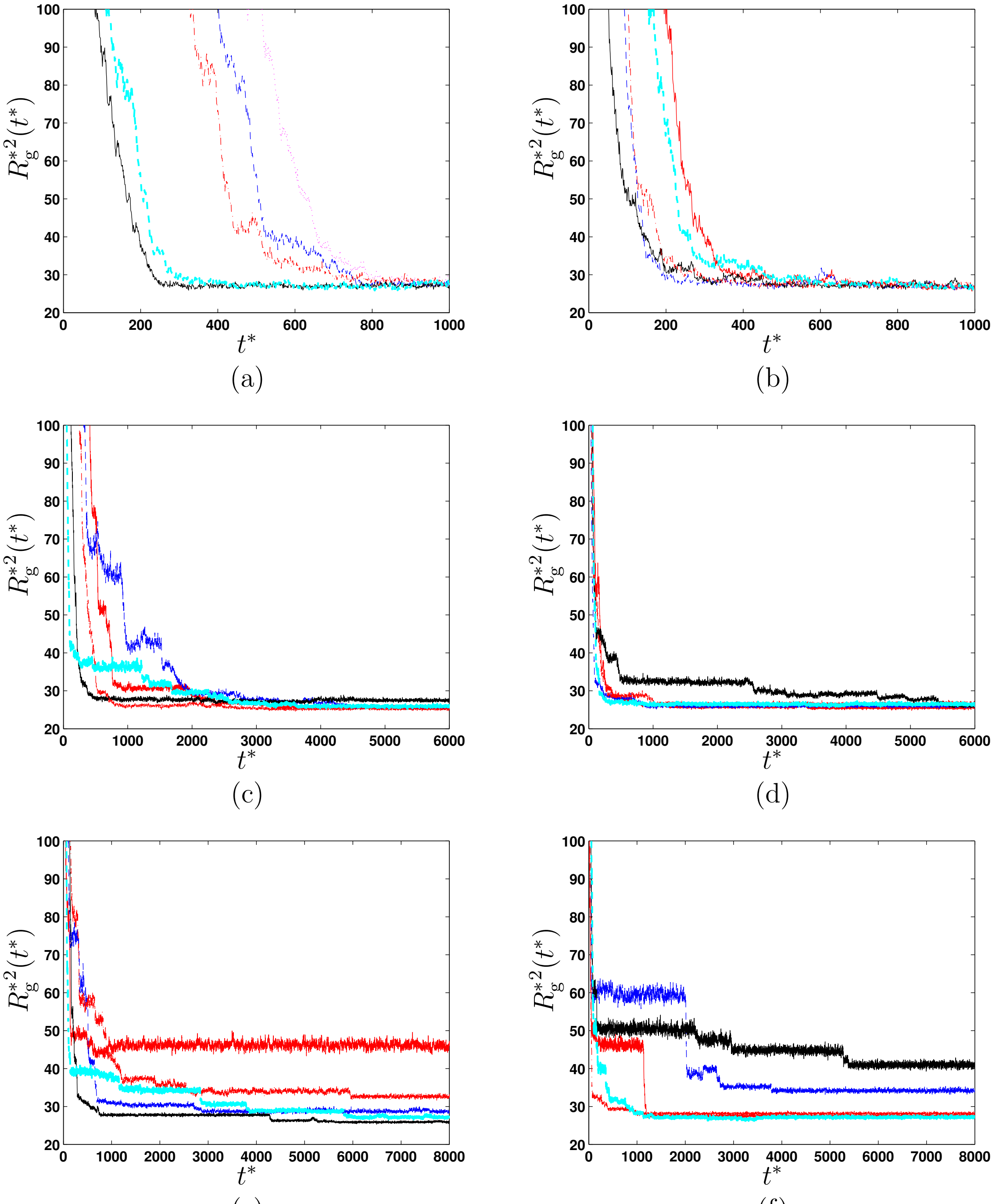

(a) (b) (c) (d) (e) (f)

Figure 5.5: Variation of the square radius of gyration with time for various quench depths from 5 independent trajectories, for chain length $N = 64$. (a) $\epsilon^*_{\mathrm{LJ}} = 2.61$, (b) $\epsilon^*_{\mathrm{LJ}} = 2.61, \tilde{h}^* = 0.50$, (c) $\epsilon^*_{\mathrm{LJ}} = 5.00$, (d) $\epsilon^*_{\mathrm{LJ}} = 5.00, \tilde{h}^* = 0.50$, (e) $\epsilon^*_{\mathrm{LJ}} = 10.00$, and (f) $\epsilon^*_{\mathrm{LJ}} = 10.00, \tilde{h}^* = 0.50$.

five independent trajectories for chains of length $N = 64$, with and without HI at three different quench depths $\epsilon^*_{\mathrm{LJ}} = 2.61, 5.00$ and 10.00. At the lowest quench depth ($\epsilon^*_{\mathrm{LJ}} = 2.61$), all trajectories go to their equilibrium values independent of the presence of HI [Figs. 5.5(a) & 5.5(b)] with a slightly smoother collapse for some of the trajectories with HI. As expected, the time taken for the trajectories to reach the equilibrium values is smaller in the presence of HI. For the remaining intermediate and largest quench depth, some trajectories become trapped in metastable states and this trapping effect happens more frequently at larger quench depth [Fig. 5.5(c)-(f)]. Here, the change in the chain size occurs in a discrete manner, hopping from one metastable state to another until the final configuration is reached. Even the inclusion of HI cannot avoid the trapping at sufficiently large values of the quench depth.

As mentioned earlier, both the explicit solvent MD simulations of Chang and Yethiraj [33], and the SASA model of Reddy and Yethiraj [171] lead to a collapse pathway that is free of trapped states even at large quench depths. The discrepancy between these results and results of other simulation techniques remains an unanswered question. Based on the similarity between the picture of collapse in this work and the observations of Kikuchi et al. [104], where HI was included explicitly, it seems likely that the discrepancy with the results of Yethiraj and coworkers arises not because of the presence or absence of HI, but because of the different treatment of solvent quality effects in the different approaches. As suggested by Chang and Yethiraj [33], due to the absence of the solvent spatial volume, an implicit treatment of solvent molecules cannot capture the crowding effect seen in explicit solvent MD simulations, and hence might be responsible for the discrepancy.

In this context, it is worth noting that due to the large computational effort, and for convenience, all simulation studies of the collapse transition by explicit solvent MD carried out so far have used solvent particles which are identical to the monomers on the polymer chain [2; 33; 162; 163; 164; 171]. Consequently, it is not clear how sensitive the results are to the size of the solvent molecules. In an extensive investigation of a binary mixture of nano-colloidal particles using equilibrium and nonequilibrium MD simulations, McPhie et al. [137] have shown that the results of MD simulations only approach the Brownian limit when the mass ratio between the monomer and the solvent particles, $\mu \geq 50$, or the size ratio, $s \geq 4$. Since in the theory that leads to BD simulations the mass ratio is assumed to approach infinity, it seems reasonable to expect that in order to compare the results of MD simulations with those of BD simulations, it is preferable to use size and mass ratios in the MD model at which the results from both the models are comparable. In the case of the polymer collapse problem, Polson and Moore [162] have suggested that it would be very useful to investigate systems with smaller solvent-to-monomer size ratios, with the implication that this more accurately describes the polymer-solvent systems in experimental studies of polymer collapse. Clearly a detailed investigation of the effect of the solvent size on the collapse dynamics of polymers is required before the reasons for the discrepancy between explicit MD and BD simulations can be completely resolved.

Snapshots of the typical collapse pathways for a collapsing chain of length $N = 128$ at two different quench depths, $\epsilon^*_{\mathrm{LJ}} = 2.61$ and 10.00, are shown in Figs 5.6 and 5.7, respectively. For comparison, the results are presented both in the absence and in the presence of HI with $\tilde{h}^* = 0.5$. There are no noticeable differences in the collapse pathways for the two cases. However, the collapse pathways are significantly different for small and large quench depths. For small quench depth (Fig. 5.6), the chain quickly forms localized blobs and these blobs then coarsen to form a dumbbell or two pearls separated by a linear chain. Finally, the pearls combine to form a sausage which slowly rearranges itself into a compact state. Similar qualitative features of the collapse pathways have been observed by other authors [2; 33; 104]. For large quench depth, Fig. 5.7, the formation of localized blobs and sausage like structure is very rapid but the transformation from the sausage to the globule is much slower.

Due to the conflicting depiction of various scaling law exponents in literature, we have also attempted to explore this issue with the predictions of BD simulations. However, we have only carried out this analysis for $\epsilon^*_{\mathrm{LJ}} = 2.50$, where no trapping occurs.

The exponent α characterizing the power law decay of the mean square radius of gyration ($\left\langle R_{\mathrm{g}}^2(t) \right\rangle = \left\langle R_{\mathrm{g}}^2(0) \right\rangle - At^{\alpha}$, where A is a constant) at the initial stage of collapse is obtained by fitting a linear curve to the log-log plot of $\left\langle R_{\mathrm{g}}^2(0) \right\rangle - \left\langle R_{\mathrm{g}}^2(t) \right\rangle$ vs t. An example of this procedure is shown in Fig. 5.8 and the inset shows the values of α for various degrees of polymerization N at low quench depth ($\epsilon^*_{\mathrm{LJ}} = 2.50$). The computed values of α for various chain lengths are given in Table 6.1. The values of α for $\tilde{h}^* = 0.25$ follow the same trend as that for $\tilde{h}^* = 0.5$, but they lie between

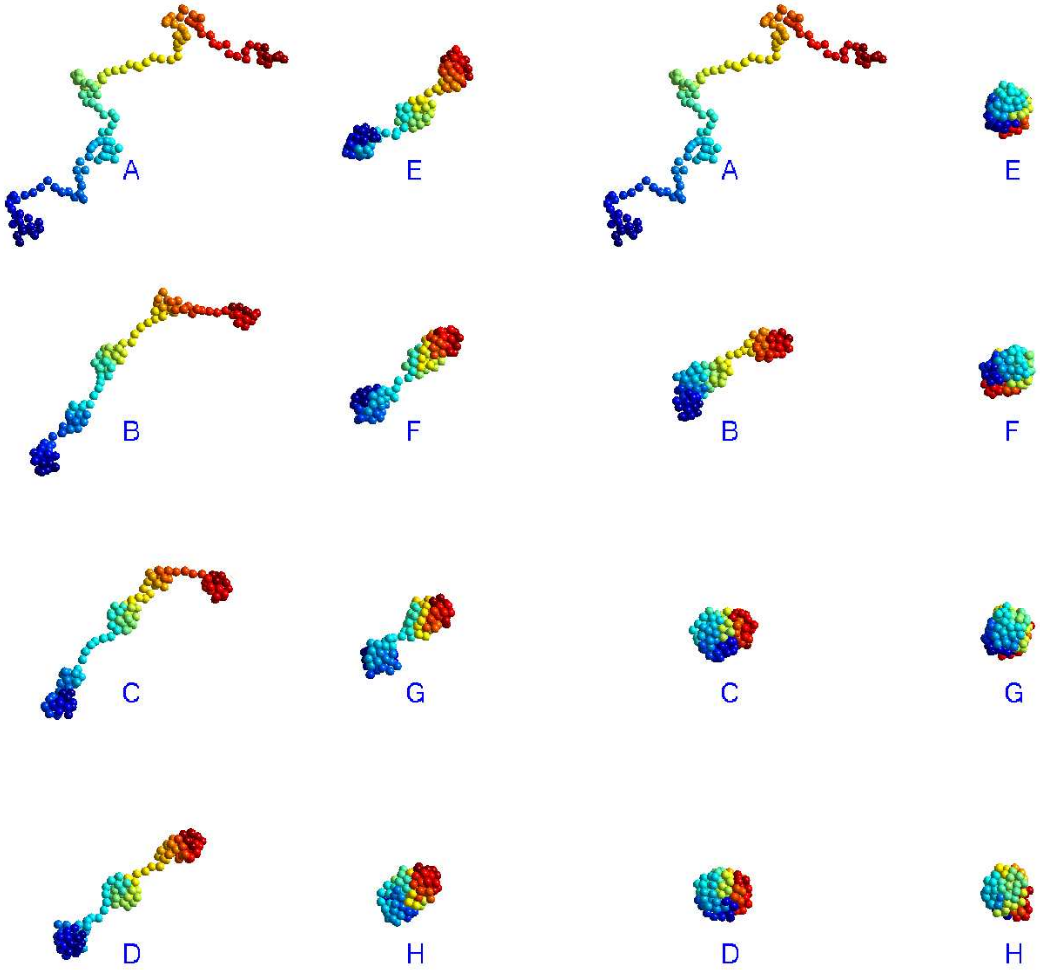

(a) (b)

Figure 5.6: Simulations snapshot of a collapsing $N = 128$ chain at $\epsilon^*_{\mathrm{LJ}} = 2.61$, (a) in the absence of HI and, (b) in the presence of HI with $\tilde{h}^* = 0.50$. The time interval between each successive snapshot is 280 λ_H and the sequence is A to H.

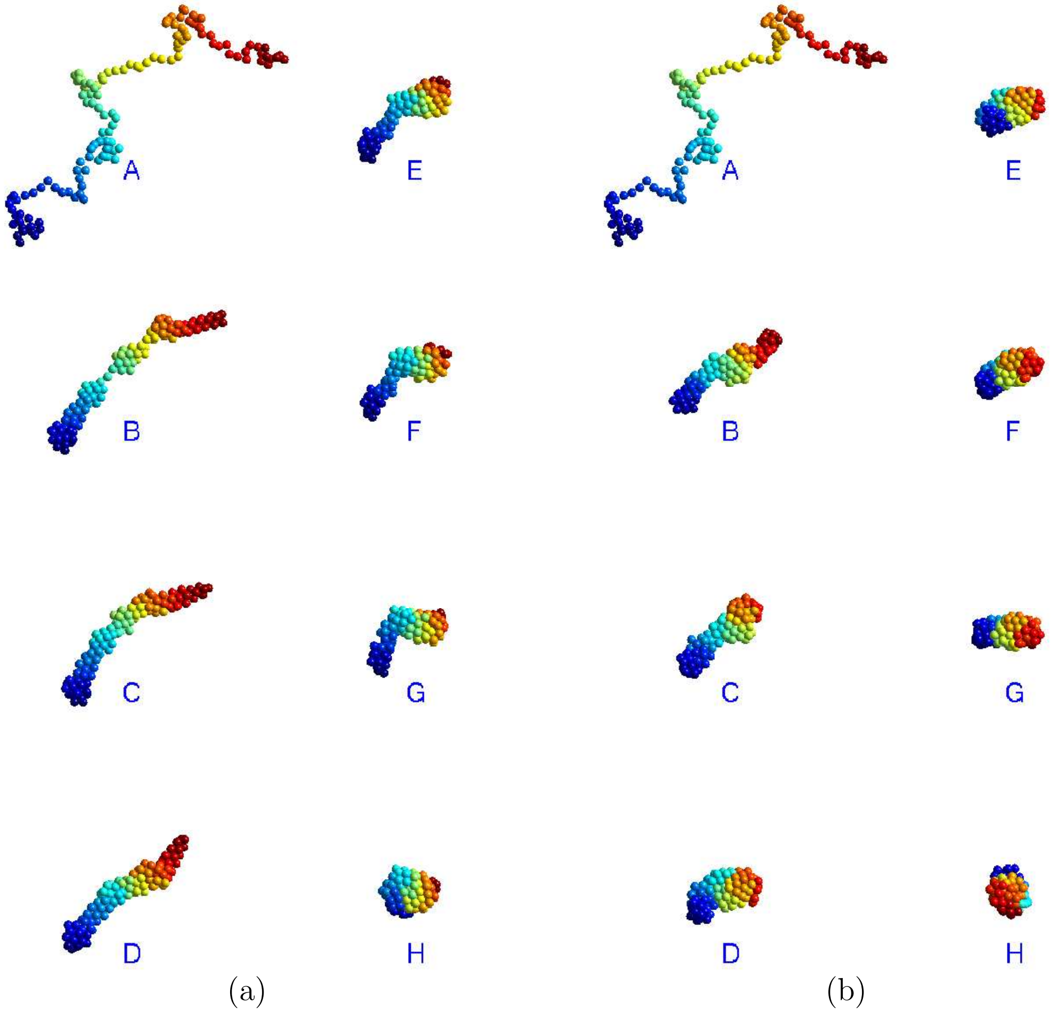

Figure 5.7: Simulations snapshot of a collapsing $N = 128$ chain at $\epsilon^*_{\rm LJ} = 10.00$, (a) in the absence of HI and, (b) in the presence of HI with $\tilde{h}^* = 0.50$. The time interval between each successive snapshot is 280 λ_H and the sequence is A to H.

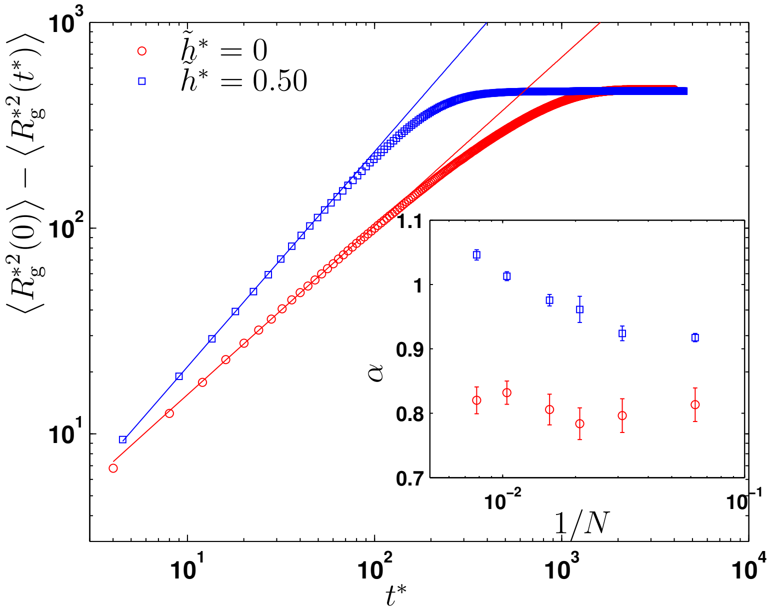

Figure 5.8: Decrease in the magnitude of the mean square radius gyration relative to its initial size with time for a collapsing polymer chain of length $N = 128$, in the absence and presence of HI, at a low quench depth, $\epsilon^*_{\rm LJ} = 2.50$. Inset: The corresponding values of α for various chain lengths.

Table 5.1: Values of the exponents for the early stages of collapse and the growth of the number average cluster size for $D = 1.20 D_{min}$ (i.e. α and z in $R_g^2 \sim t^\alpha$ and $\langle S_n \rangle \sim t^z$) at various degrees of polymerization N, in the absence and in the presence of HI. Note that only the values at low quench depth $\epsilon^*_{\rm LJ} = 2.50$ have been calculated, where no trapping occurs.

N	$\alpha\,(\tilde{h}^* = 0)$	$\alpha\,(\tilde{h}^* = 0.50)$	$z\,(\tilde{h}^* = 0)$	$z\,(\tilde{h}^* = 0.50)$
16	0.81 ± 0.03	0.92 ± .01	0.42 ± 0.01	0.53 ± 0.01
32	0.80 ± 0.03	0.92 ± .01	0.53 ± 0.01	0.72 ± 0.01
48	0.78 ± 0.02	0.96 ± .02	0.58 ± 0.01	0.85 ± 0.01
64	0.81 ± 0.02	0.98 ± .01	0.62 ± 0.01	0.93 ± 0.01
96	0.83 ± 0.02	1.01 ± .01	0.66 ± 0.01	1.04 ± 0.01
128	0.82 ± 0.02	1.05 ± .01	0.67 ± 0.01	1.08 ± 0.01

the values of α for $\tilde{h}^* = 0$ and $\tilde{h}^* = 0.5$. For the case with HI, only property values for $\tilde{h}^* = 0.5$ are reported here as chains with this value of $\tilde{h}^*$ collapse more rapidly compared to those with $\tilde{h}^* = 0.25$. It is clear from the inset of Fig. 5.8 that while the values for α appear to have reached their asymptotic limit with large N for the case without HI, the asymptotic value of α is yet to be attained for simulations with HI at $N = 128$, which is the largest value considered here. The computational intensity for larger values of N has prohibited us from considering even larger values of N, so we report the value at $N = 128$ here.

Values of α reported previously in literature are shown in Table 5.2. Kuznetsov et al. [115] used the Gaussian self-consistent (GSC) method and predicted that for small quench, the exponent α should take a value ~ 0.6363 in the absence of HI, and ~ 0.8181 in the presence of HI, which are different from the ones predicted here. However, the exponent values predicted by Kuznetsov et al. [115] may not be accurate because the GSC method has been known to predict an incorrect Flory exponent in the large fluctuation regime, i.e. for chains in good and theta solvents [24; 46; 50; 201]. On the other hand, our predictions are close to $\alpha = 1$ (with HI) and 3/4 (without HI) predicted by Pitard [160]. This is expected because the model used here is a rigorous version of the model used by Pitard [160] and includes fluctuating hydrodynamic interactions.

The second stage of collapse is known as cluster coarsening, where previous studies indicate that a power law also holds for the growth of the average cluster size with time ($\langle S(t) \rangle \sim t^z$). The growth of the number average and the weight average cluster size with time for a wide range of overlapping distances D is shown in Fig. 5.9. The overlapping distance D is measured in term of D_{min}, where $D_{min} = 2^{1/6}(\sigma/l_H)$ is the distance at the minimum of the Lennard Jones potential. The values of the cluster growth exponent z at a chosen overlapping distance are obtained from the slope of a linear fit to the linear portion of the log-log plot of $\langle S(t) \rangle$ vs t (as shown in Fig. 5.10). Moreover, the overlapping distance D should be chosen such that at the final compact globular state, the average cluster size should be the same as the chain length N because the chain has formed a single cluster of N beads at this stage. Fig. 5.9 indicates that the minimum value of D/D_{min} should be 1.10 or higher in order to satisfy this requirement. The values of z for the two different definitions of the average cluster size at various overlapping distance are shown in the inset of Fig. 5.9 and they are also listed in Table 5.4. The above figure and table indicate

Table 5.2: Values of all the scaling exponents reported in literature, in the absence and in the presence of HI.

Authors	α no HI	α HI	z no HI	z HI	γ no HI	γ HI
Abrams et al. [2]	–	–	–	–	3/2	5/6
Byrne et al. [26]	–	–	0.66	–	–	–
de Gennes and co-workers [25; 45]	–	–	–	–	2.00	0.50
Halperin and Goldbart [80]	–	–	–	–	6/5	4/5
Kikuchi et al. [104]	–	–	1/2	3/4	2	4/3
Klushin [107]	–	–	0.54	0.80	1.60	0.93
Dawson and co-workers [114; 115]	7/11	9/11	1/2	–	1.96	1.34
Lee and Kapral [123]	–	–	–	–	–	1.00
Pitard and co-workers [160; 161]	3/4	1	–	–	5/3	1.00
Our results	0.82 ± 0.02	1.05 ± 0.01	0.67 ± 0.01	1.08 ± 0.01	1.35 ± 0.01	1.01 ± 0.01

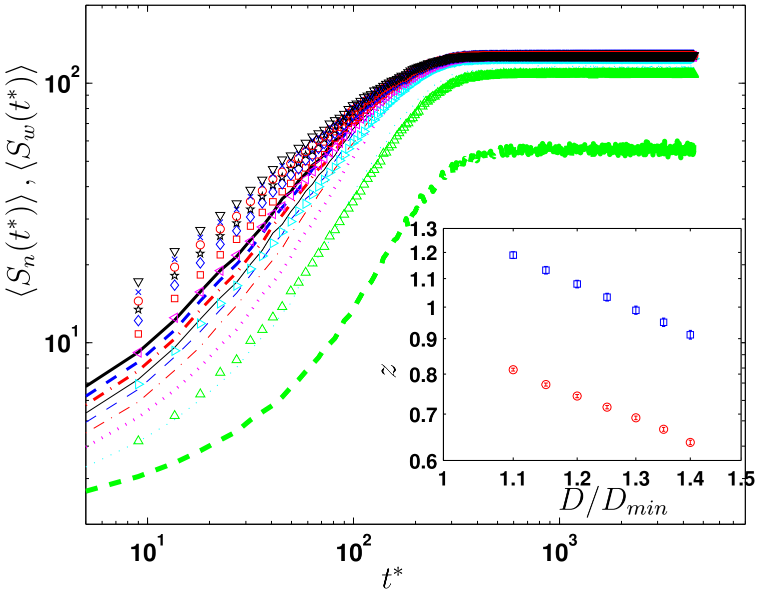

Figure 5.9: Variation of the number average and the weighted average cluster size with time for a collapsing polymer chain with $N = 128$, in the presence of HI, at a low quench depth, $\epsilon^*_{\text{LJ}} = 2.50$. From bottom to top: $D/D_{min} = 1.00$ (where $D_{min} = 2^{1/6}(\sigma/l_H)$) with an increment of 0.05 for each line and symbol moving upwards. Lines represent the number average cluster size and symbols represent the weight average cluster size. Inset: The corresponding values of z for the number average (square) and the weighted average (circle) cluster size for various values of overlapping distance D.

that there is no universal value for the exponent z and that z is very sensitive to the value of the overlapping distance D. Furthermore, one can clearly see from this figure that there are only two different regimes for the weight average cluster size, while there are three different regimes for the number average cluster size. Since the number average cluster size definition reproduces the visual observation of a three-stage collapse (as seen in Fig. 5.6), we have used this definition here to characterize cluster growth.

Even though there is no unique choice of D, a value of $D/D_{min} = 1.2$ is used in order to compare with the numerical value of z reported by Byrne et al. [26], who have used this value previously. The number average cluster growth for this value of D is shown in Fig. 5.10 and the figure inset shows the values of z for various chain lengths. These values are also listed in Table 6.1 for different N. Interestingly, for this choice of D, z attains an asymptotic value with increasing N. In the free

Table 5.4: Values of the exponent z for the growth of the average cluster size at various values of overlapping distance D (in unit of $D_{min} = 2^{1/6}(\sigma/l_H)$) for a collapsing polymer chain with $N = 128$, in the presence of HI at $\epsilon_{\rm LJ}/k_{\rm B}T = 2.50$.

D/D_{min}	z for $S_n \sim t^z$	z for $S_w \sim t^z$
1.10	1.19 ± 0.01	0.81 ± 0.01
1.15	1.13 ± 0.01	0.77 ± 0.01
1.20	1.08 ± 0.01	0.74 ± 0.01
1.25	1.03 ± 0.01	0.72 ± 0.01
1.30	0.99 ± 0.01	0.69 ± 0.01
1.35	0.95 ± 0.01	0.67 ± 0.01
1.40	0.91 ± 0.01	0.64 ± 0.01

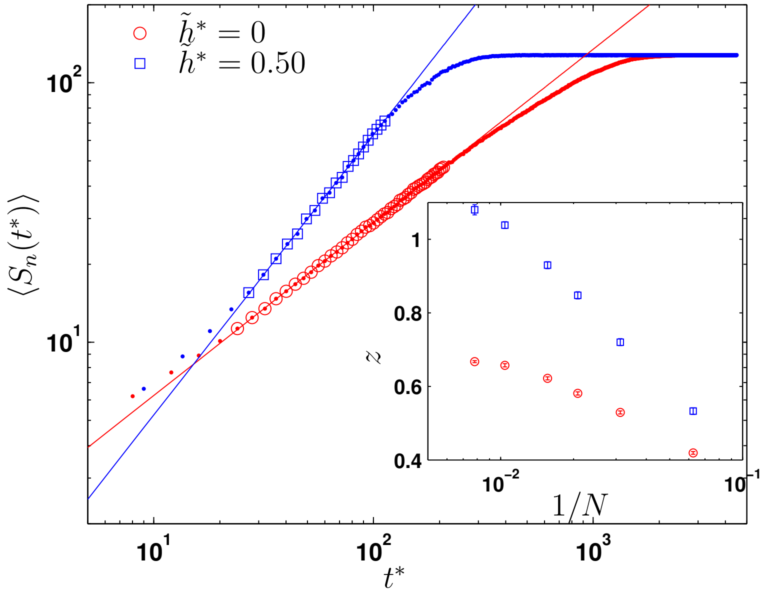

Figure 5.10: Variation of the number average cluster size with time for a collapsing polymer chain with $N = 128$ for $D/D_{min} = 1.20$, in the absence and presence of HI, at a low quench depth, $\epsilon^*_{\rm LJ} = 2.50$. Inset: The corresponding values of z for various chain lengths.

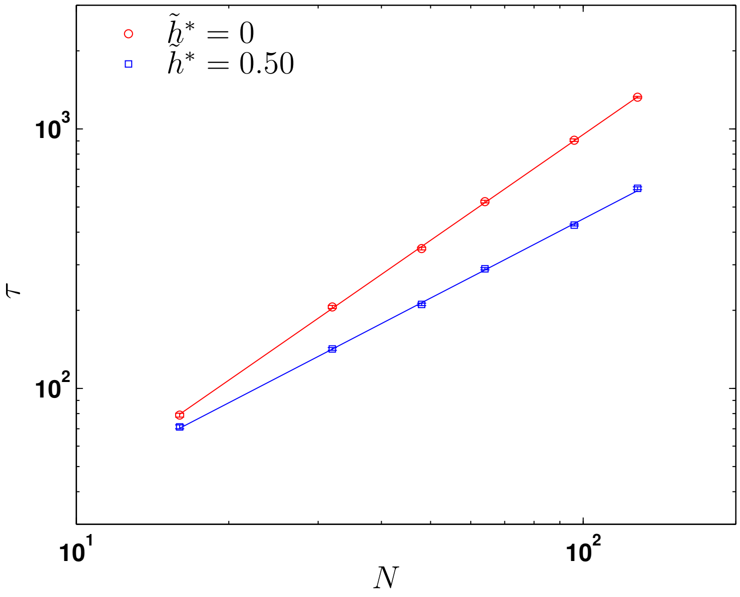

Figure 5.11: Mean collapse time at various chain lengths, in the absence and presence of HI, at a low quench depth, $\epsilon^*_{\text{LJ}} = 2.50$.

draining limit ($\tilde{h}^* = 0$), the exponent value has converged to the limiting value of 2/3 reported by Byrne et al. [26], and is slightly larger than the prediction of 0.54 by Klushin [107]. In the presence of HI, the value appears to be converging to $z \sim 1$ for $\tilde{h}^* = 0.50$, which is larger than the theoretical value of 0.80 predicted by Klushin [107] (see Table 5.2 for a detailed comparison).

The characteristic collapse time (τ) has been predicted to scale with the chain length (N) as $\tau \sim N^\gamma$. Results for the collapse time τ for different values of N are shown in Table 5.5 and Fig. 5.11. It is observed that for all N, the collapse time is always smaller when HI is switched on (τ_H) compared to the case where HI is suppressed (τ_B). The rate of collapse also increases with increasing strength of HI, which is not shown here. The exponents for the collapse time are $\gamma_H = 1.01 \pm 0.01$ for $\tilde{h}^* = 0.5$ and $\gamma_B = 1.35 \pm 0.01$. These results agree reasonably well with values reported by other authors [2; 107; 160]. However, they are different from the values predicted recently (4/3 and 2 with and without HI, respectively) by Kikuchi et al. [103, 104]. We believe that the reason for the discrepancy could lie in the relative large ratio of chain size to the box length used in the simulations performed by Kikuchi et al. [104], which might affect dynamic scaling. More recently, Lee and Kapral [123] have used the same method but with a larger box length to study

Table 5.5: Average collapse time of a polymer chain of length N, without (τ_B) and with (τ_H) hydrodynamic interactions, at $\epsilon_{\mathrm{LJ}}/k_{\mathrm{B}}T = 2.50$. The values of the exponent γ for the total collapse time in terms of the degree of polymerization N ($\tau \sim N^{\gamma}$) are also listed.

N	τ_B ($\tilde{h}^* = 0$)	τ_H ($\tilde{h}^* = 0.50$)
16	78.92 ± 1.35	71.16 ± 1.23
32	206.10 ± 2.74	142.05 ± 1.75
48	346.03 ± 4.26	211.01 ± 2.36
64	525.12 ± 6.00	289.30 ± 2.75
96	905.48 ± 9.93	426.44 ± 3.61
128	1325.69 ± 10.08	590.97 ± 7.38
γ	1.35 ± 0.01	1.01 ± 0.01

polymer collapse, and they found that in the presence of HI, the collapse time scales as $\tau_H \sim N^1$, which is closer to our prediction (see Table 5.2 for a detailed comparison).

5.4 Conclusions

We have presented an alternative way to incorporate implicit hydrodynamic interactions by means of Brownian dynamics simulations to study the dynamics of polymer collapse in a poor solvent. The Brownian dynamics simulations predict similar observations to those that have been reported previously in the literature regarding the speed up of collapse caused by hydrodynamic interactions and the existence of a three stage collapse path. One of the striking features of this study is the confirmation that an implicit treatment of HI does not avoid the trapping phenomena, and that chains always get trapped in metastable states of local free energy minima at large quench depth, unlike earlier explicit solvent based MD simulations which show a smooth transition to the final global minimum free energy state. We have computed exponents of various observable quantities to show that the predictions of BD simulation agree well with some of the theoretical predictions.

Chapter 6

Copolymer collapse

6.1 Introduction

The collapse of different types of copolymers has been studied previously through both theory [203] and simulations [40; 69; 79; 101; 102; 204; 207]. In an early theoretical study, Timoshenko et al. [203] have shown that the kinetics of collapse for random copolymers involves at least two, sometimes three, distinct stages. The earliest of these stages is described as the rapid formation of clusters or micelles along the chain, in a manner similar to homopolymer collapse. Following this stage is the coarsening of these intramolecular micelles, which coalesce at a rate that depends on the dispersion of the hydrophobicity. A third kinetic stage is also observed for polymers with particularly large dispersion, i.e. chains which are composed of more H beads than P beads, where rapid rearrangement to a more compact globule occurs. Using Brownian dynamics simulations of a bead-spring chain model composed of 50% H and 50% P monomers without incorporating HI, Cooke and Williams [40] found that microphase separation (H blocks being separated by P blocks due to unfavourable interactions) plays an important role in the thermodynamics as well as the kinetics of collapse for heteropolymers with various block sizes. This microphase separation often gives rise to compact states in the form of connected strings of intrachain micelles. The existence of strings of such micelles has been observed in simulations [40; 69; 204] and was also predicted by Halperin [79].

Even with the above composition for H and P monomers, the number of possible sequences and conformations is still too large to be investigated via computer simulations. This is one of the primary motivations for many researchers in recent years to attempt to design or engineer sequences that mimic biological evolution such that they rapidly fold to a desired target native structure with lowest energy [182; 184; 185]. Recently, Khokhlov and Khalatur [101; 102] have introduced a method of designing a copolymer chain composed of 50% H and 50% P monomers such that it would fold rapidly into its final native structure and is quite stable. The method involves first collapsing a homopolymer chain into its equilibrium compact state and then marking half of the monomers that are closest to the center of mass as H type while the remaining monomers are marked as P type. Surprisingly, copolymer chains with sequences generated via this method (also known as "protein-like" copolymers) were found to fold much more rapidly and the native conformations were more stable compared to random copolymers (RC) and random block copolymers (RBC) with the same average block length of H or P polymers $\langle L \rangle$. Although the protein-like copolymer (PLC) chains seem to collapse faster and they form the most compact equilibrium structures compared to RBC chains with the same average block length $\langle L \rangle$, it remains to be seen if this behavior also holds for off lattice bead-spring chain models, especially when HI is present. In addition, it is unclear whether RBC chains with different average block lengths $\langle L \rangle$ also consistently collapse slower and are less compact compared to PLC chains in the presence of HI.

In this chapter, we use Brownian dynamics simulations of bead-spring chains composed of 50% hydrophobic H type beads and 50% polar P type beads to investigate the effect of chain sequence on copolymer collapse. In particular, our aim is to determine the effects of block length on the kinetics of folding and the compactness of the final collapsed state in the presence of HI, for three different copolymers, namely, multi-block copolymers (MBC), random block copolymers (RBC) and protein-like copolymers (PLC). The exact features of a sequence that directly governs the chain's kinetics of collapse and its final equilibrium size will be identified. Effects of HI and chain length on the order of collapse amongst the various copolymers is also examined.

6.2 The Model

6.2.1 General Model

Here, we have employed a two letters code HP model for our copolymers. The polymer is assumed to be in an aqueous solvent such that HP and PP interactions are purely repulsive (i.e. in good solvent), while HH interactions are attractive (i.e. in poor solvent).

In this chapter, the same dimensionless potentials accounting for bead-bead interactions and spring entropic resistance as well as simulation technique are used here as used previously in Chapter 5. In this work, we use $\tilde{h}^* = 0.50$ (i.e. $h^* = 0.46$ for the chosen value of $Q_0^* = 2\sqrt{7}$) to account for HI, since it has been shown previously that this value leads to a rapid collapse. The quench depth value used here is chosen based on the value used in the work for homopolymer collapse, namely, $\epsilon_{\text{LJ}}^* = 2.50$, since with this value, a homo-polymer chain smoothly folds into its final equilibrium compact stage without being trapped in one of its intermediate metastable states.

The main aim of this study is to investigate the effect of the sequence and/or the average block size on the static and dynamic properties of different types of copolymers including the protein-like copolymer (PLC) generated by the coloring algorithm proposed by Khokhlov and Khalatur [101, 102], both in the presence and in the absence of HI.

Since the energy of the denatured state is not sequence-specific, the chain sequence does not play a role under good solvent conditions [184]. In fact, it is thermodynamic quantities such as the temperature that govern the chain properties in the denatured state. Chain initial configurations are generated from the random walk distribution function. For equilibration in the denatured stage, we have treated all copolymer chains as homo-polymer chains and they are brought to equilibrium in good solvent conditions by carrying out BD simulation for a period of $T_{\text{eq}} = 15\tau_{1,\text{R}}^*$, where $\tau_{1,\text{R}}^* = 0.5 \sin^{-2}(\pi/2N)$ is the longest dimensionless Rouse relaxation time. Moreover, hydrodynamic interactions were turned off during the equilibrium simulations as HI does not affect the equilibrium distribution. For convenience, we have saved the equilibrium position vectors of 500 independent homopolymer chains in good solvent conditions in a file and used them as initial configurations for all types of copolymer chains. With these stored configurations, each copolymer chain is constructed with a selected sequence and then suddenly quenched into poor solvent conditions by switching the potential from good to poor and various properties are then monitored. For all the simulations, the time step size $\Delta t^* = 0.001$ is used which yielded a solution with very small discretization errors. Property values are obtained from an ensemble average of 500 statistically independent trajectories, which use the starting configurations from these saved files.

6.2.2 Chain Sequence Construction

We have carried out simulations for two different chain lengths of $N = 64$ and 128 beads at a fixed H:P ratio of 1:1 (i.e. $N_{\mathrm{H}} = N_{\mathrm{P}} = N/2$). We have studied three different families of copolymer chains with sequence types that were either inherited from the parent globule, regular or probabilistic. The first type is the protein-like copolymers or PLC, where the process of generating the sequence involves first collapsing a homopolymer to its native state. Then the interior of this collapsed globule is marked as the hydrophobic H block and the exterior as the hydrophilic or polar P block. The marked chain is then unraveled to obtain a designed sequence of copolymers. The second family of copolymers is the regular or alternating multiblock copolymers (MBC), where the sequences were of the form $L\mathrm{H}L\mathrm{P}$ with $N/2L$ blocks, with L being the size of contiguous H or P blocks. The last family is known as the random-block copolymers (RBC) in which the chain sequence is primarily characterized by the Poisson distribution $f(x) = e^{-\lambda}\dfrac{\lambda^x}{x!}$, $(x = 1, \ldots, \lambda > 0)$, where $\lambda = \langle L \rangle$ is the average block length, and x is the size of the contiguous block.

6.3 Results and discussion

In this section, we numerically investigate the dynamics of collapse for three different types of copolymers at a single value of the strength of the attractive interaction or quench depth, $\epsilon^*_{\mathrm{LJ}} = 2.50$, both in the presence and in the absence of HI. We monitor various observable quantities given below, which can be used to characterize the kinetics of collapse.

Apart from the mean square radius of gyration given by Eq. 5.6, the state of polymer collapse can also be observed by the internal energy U, which is given as

$$U = \sum_{ij} (V_{\mathrm{EV}}(r^*_{ij}) + C(\mu, \nu) V_{\mathrm{attr}}(r^*_{ij})), \tag{6.1}$$

where the function $C(\mu, \nu)$ takes a value of 1 when μ and ν are both H type monomers and 0 otherwise.

In addition, the growth of the average cluster size with time $\langle S(t^*) \rangle$ is also monitored. We have used the definition of the number average cluster size to study this property, which has been shown to consistently reproduce three-stage kinetics for homo-polymer collapse [158]. The number average cluster size is defined as

$$\langle S_n(t^*) \rangle = \frac{\sum_s s n(s)}{\sum_s n(s)}, \tag{6.2}$$

where s denotes the cluster size and $n(s)$ the number of clusters of size s. The algorithm proposed by Sevick et al. [181] is used to compute the number of clusters and their size. Only H type beads were used to define a cluster. The cluster size is determined by considering non-nearest-neighbor beads to be a part of a cluster when their separation is less than a certain overlapping distance D. In addition, a bead cannot use the separation from either of its nearest-neighbors to register itself as part of a cluster, even if the neighboring bead already belongs to a cluster. It is worth mentioning that in the previous chapter, we have found that the exponent z for the scaling law $\langle S_n \rangle \sim t^z$, observed in the second stage of collapse, is not universal and it is very sensitive to the value of the overlapping distance D for homo-polymer collapse. Further details on the average cluster size and the sensitivity of z to D can be found in Chapter 5.

Figure 6.1 shows the effects of block length L and average block size $\langle L \rangle$ for the protein-like, regular multi-block and random block copolymer chains on the evolution of the mean square radius of gyration for $N = 128$, in the presence of HI. The data certainly shows that the average block length plays an important role in accelerating the collapse as well as controlling the final equilibrium size of the copolymer chains. It is worth mentioning that the average block length $\langle L \rangle$ for a PLC chain in our model, for both $N = 64$ and $N = 128$ bead chains, is approximately 3, which is very close to the value reported by Khokhlov and Khalatur [101, 102] ($\langle L \rangle = 3.173$), who used a lattice model for $N \geq 256$ chains. We first discuss the

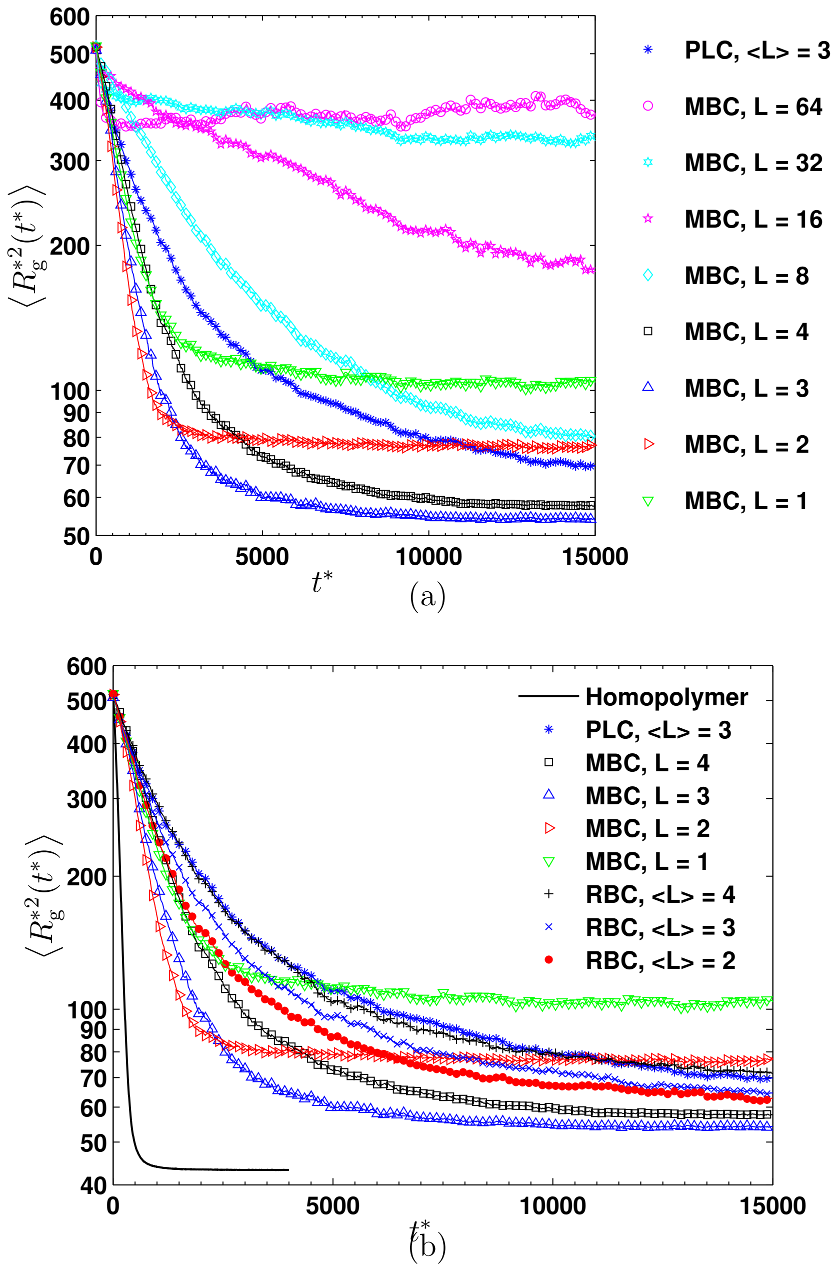

(a)

(b)

Figure 6.1: Variation of the mean square radius of gyration with time for $N = 128$ chains, in the presence of HI, for (a) the PLC chain and MBC chains with various values of block length L, and (b) all three types of copolymers with values of average block length $\langle L \rangle \leq 4$.

Table 6.1: Values of the exponents for the early stages of collapse and the growth of the number average cluster size for $D/D_{\text{min}} = 1.20$ (i.e. α and z in $\left\langle R_{\text{g}}^2(0)\right\rangle - \left\langle R_{\text{g}}^2(t)\right\rangle \sim t^{\alpha}$ and $\langle S_n\rangle \sim t^z$) for all types of copolymers with $N = 128$ at various values of average block lengths $\langle L\rangle$, in the presence of HI. Values of the total collapsed time τ and the equilibrium mean square radius of gyrations $\left\langle R_{\text{g}}^2\right\rangle_{\text{eq}}$ are also listed here to give an indication of how fast the chain collapsed and their compactness at the equilibrium collapsed stage. Note that PLC, MBC and RBC denote protein-like, multi-block and random-block copolymers, respectively.

Type	$\langle L\rangle$	α	z	τ	$\left\langle R_{\text{g}}^2\right\rangle_{\text{eq}}$
PLC	3	0.945 ± 0.021	0.510 ± 0.009	5732 ± 146	69.762 ± 1.151
MBC	64	0.999 ± 0.012	0.920 ± 0.044	2044 ± 185	369.034 ± 8.605
MBC	32	0.978 ± 0.022	0.158 ± 0.003	N/A	N/A
MBC	16	0.842 ± 0.043	0.441 ± 0.005	N/A	N/A
MBC	8	0.616 ± 0.020	0.646 ± 0.004	6670 ± 139	79.819 ± 0.989
MBC	4	1.033 ± 0.026	0.819 ± 0.017	4248 ± 101	57.616 ± 0.064
MBC	3	1.316 ± 0.088	0.858 ± 0.018	3304 ± 118	54.287 ± 0.239
MBC	2	1.287 ± 0.029	1.008 ± 0.025	1967 ± 53	77.051 ± 0.385
MBC	1	0.929 ± 0.038	0.857 ± 0.018	2771 ± 103	103.906 ± 1.134
RBC	4	0.987 ± 0.028	0.631 ± 0.008	5447 ± 138	71.511 ± 1.278
RBC	3	1.071 ± 0.025	0.575 ± 0.006	5496 ± 141	64.513 ± 1.006
RBC	2	1.045 ± 0.037	0.595 ± 0.009	4948 ± 132	62.839 ± 0.985

effect of block length on the behavior of the MBC chain. The simplest type of MBC is the diblock copolymer with $L = N/2$. It can be seen from Fig. 6.1 (a) that this diblock chain collapses to its equilibrium state faster than any of the other copolymer chains present in the plot. This is always true for such a copolymer because one of its ends (i.e. the end with the H block) behaves like a homo-polymer chain in a poor solvent, which rapidly folds into its final equilibrium globular state, while the other end behaves like a homopolymer in a good solvent, remaining as a swollen coil. Due to the large size of this swollen part, the chain cannot form a compact equilibrium structure and consequently always has a relatively large final equilibrium size. By reducing the block size to $L = 32$, so that one has 4 blocks, one can clearly see two distinctive regions of collapse. The first region represents the early stage of collapse, where each H block of size L rapidly folds into a single cluster. Thus at the end of this stage, the chain is made up of $N/2L$ clusters or pearls separated by strings of P block chains. Since the folding of the H block is entirely homopolymer-like and is unaffected by the P type monomers, the time taken for each of these H block chains to completely fold into a small cluster within each block is quite fast. This leads to a narrow range of time where the early stage of collapse occurs. The time window where this early collapse stage takes place depends on the block size of the H block as it takes longer for a large block to completely fold compared to a smaller block, as might be expected. The second regime represents the growth or coalescence of these intrachain-clusters into a single large cluster. These clusters are separated from each other by a string of P block, which has the same fully stretched length as that of the original H block. If the separation between the two intrachain-clusters is larger than the range of the attractive interaction (or equivalently, the P block chain length is large), then these intrachain-clusters go through a diffusion-like process, with each of these clusters diffusing around due to thermal fluctuations. It is only when they interact with each other, i.e. when their separation distance comes within the range of attractive interaction, that they coalesce. Thus the growth of the average cluster size is quite gradual in this case. However, if the P block chain length is sufficiently small such that two intrachain-clusters are within the range of their attractive interaction, then the two clusters quickly coalesce to form a larger cluster and diffusion plays little or no role in the collapse. Moreover, the average cluster size will also grow much more rapidly, or equivalently, there is a rapid reduction in chain size. Since the diffusion time is proportional to the size of the intervening P block [40], it is expected that the coalescence time is shorter for smaller P block sizes and consequently the collapse is much more rapid compared to large P block sizes. Further, the presence of a large P block size also leads to a less compact final collapsed size because blocks of P beads always repel the core of H beads and they form dangling legs extruding away from the core, resulting in a larger equilibrium size.The results for $L = 32$ to $L = 8$ for MBC chains in Fig. 6.1 (a) also confirm these expectations. Since the window for the early stage of collapse is quite narrow for most copolymer chains investigated, it is not clearly visible in Fig. 6.1. Note that for all MBC chains with $L \geq 8$, the final equilibrium size is still larger than that of the PLC chain. However, when $L = 4$, the MBC chain reaches its equilibrium native state faster and the final equilibrium size is smaller than that of a PLC chain. Reducing the block size of MBC chain to $L = 3$ further reduces the final size as well as the total collapse time compared to values obtained for the $L = 4$ chain. In fact, the data shows that the MBC chain with $L = 3$ produces the lowest final equilibrium size compared to all other types of copolymer chains for the entire range of L and $\langle L\rangle$ values that have been investigated. The total collapse time and the mean square radius of gyration for all three types of copolymers are also listed in Table. 6.1. Further reduction in the block size to $L = 2$ leads to a slightly faster collapse (as evidenced by the value of τ in Table. 6.1), but it also increases the final chain equilibrium size. Note that for every L monomers of H type that fuse with another cluster of H type monomers, L monomers of P type are brought into close proximity due to the connectivity along the chain. As a result, a repulsive force builds up as the coalescence process takes place. For the $L = 2$ chain, the energy gained from coalescence of clusters of H type monomers cannot overcome the repulsion due to the presence of P type monomers and so the chain does not form a single cluster of H monomers. This means that the chain cannot fold into a spherical compact globule at equilibrium, and this leads to an increase in the final chain equilibrium size. The kinetics of collapse of an MBC chain with $L = 1$ also conforms to this behavior, with the chain collapsing slower, and the final equilibrium size even larger than for $L = 2$. The large increase in the repulsive force for this chain has increased the total collapse time and it further swells the chain to a larger equilibrium size.

The large repulsive force built up due to the overcrowded presence of P type monomers for MBC chains with $L \leq 2$ can also be observed via the high value of the internal energy U in Fig. 6.2. Note that the internal energy for MBC chains with $L = 32$ and 16 is not reported here because the chains with these block sizes had not yet reached their equilibrium state during the course of simulation. This figure also clearly indicates that a chain which has the lowest equilibrium size does not necessarily have the lowest internal energy. Moreover, a chain with the lowest internal energy may not fold into the most compact final structure. Our finding is also consistent with the findings reported by Cooke and Williams [40] who have used BD simulations without HI for their analysis.

From Fig. 6.1 (b), we can see that an RBC chain with $\langle L\rangle = 4$ almost has the same kinetics of collapse as well as the final equilibrium size as that of the PLC chain. However, the final equilibrium size for an RBC chain with $\langle L\rangle < 4$ is smaller than the size of a PLC chain. This result contradicts the findings of Khokhlov and Khalatur [102] who have found that an RBC chain that has the same average block size as that of a PLC chain, collapses slower and forms a less compact final structure. The

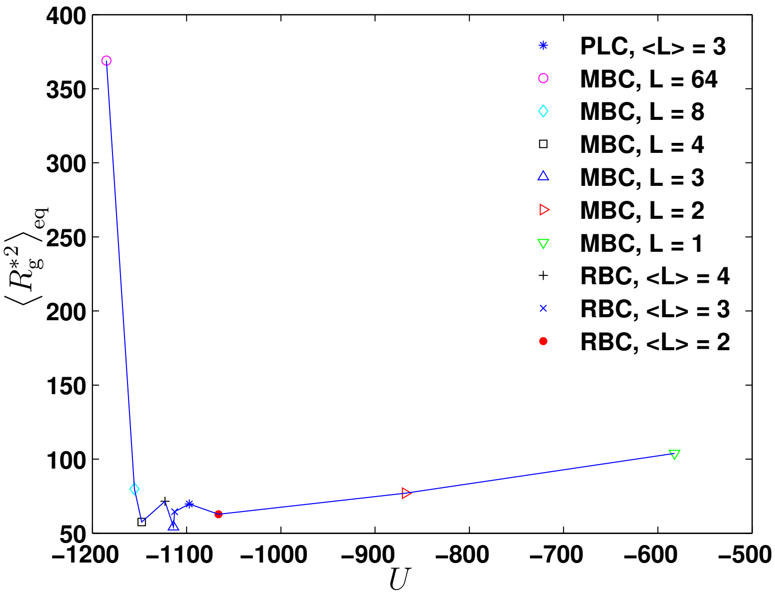

Figure 6.2: Coordinate pairs $(U, \langle R_g^{*2} \rangle_{eq})$ of the internal energy and $\langle R_g^{*2} \rangle_{eq}$, respectively, in the final collapsed state for all copolymer chains with $N = 128$, in the presence of HI.

discrepancy between our results and the results reported by Khokhlov and Khalatur [102] may arise because we have used a different model as well as a different strength of H-P interactions.

In order to show that the above results predicted by our BD simulations in terms of the order of collapse amongst the various copolymers and the final equilibrium value of R_g are independent of HI, we have carried out simulations for $N = 128$ chains without HI. In addition, simulations of $N = 64$ chains at various values of quench depth ϵ_{LJ}^* have also been carried out to show that the order of collapse amongst the various copolymers is independent of chain length as well as the quench depth. Figure 6.3 shows the effects of average block size for all types of copolymers on the evolution of the mean square radius of gyration for $N = 128$, in the absence of HI. Since it is very time consuming to completely observe a copolymer chain from its denatured state to its totally collapsed state when HI is suppressed, we have only simulated these chains up to the upper limit of time that was chosen for the case when HI is present. It can be seen from the figure that only the MBC chain with $L = 2$ has reached equilibrium and the value of the final equilibrium size is the same as for the case with HI as observed in Fig 6.1 (a). Nevertheless, the

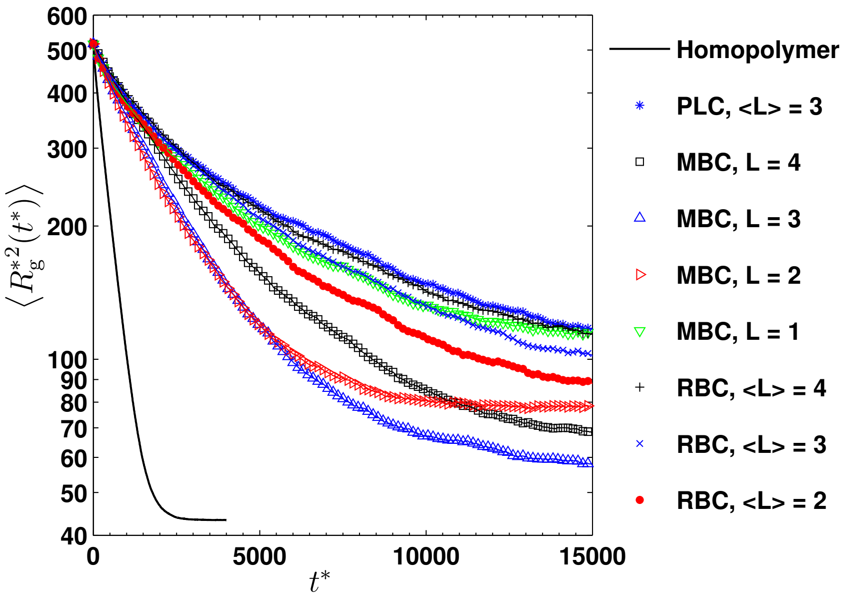

Figure 6.3: Variation of the mean square radius of gyration with time for all three types of copolymer chains with $N = 128$, for various values of the average block length $\langle L \rangle$, in the absence of HI.

qualitative similarity of the data seems to indicate that the results discussed above are independent of HI.

Figure 6.4 shows the effects of quench depth on the kinetics of collapse for $N = 64$ chains with the block length $L = 3$ (MBC) and average block size $\langle L \rangle = 3$ (PLC, RBC) for all three types of copolymers. For all the quench depths investigated, it can be seen from the figure that the MBC chains collapse the fastest and have the most compact equilibrium size, followed by the RBC chains. Out of all three types of copolymer chains, the PLC chain collapses the slowest and the final equilibrium size is the least compact. Generally, one would expect that the radius of gyration for a chain at deep quench should be smaller than that of a chain with lower quench values because the stronger attractive interaction would cause the chain to squeeze into a tighter globule. The above figure shows that a chain smoothly folds into its final compact state for low quench depth. However, at very large quench depth (i.e. $\epsilon_{\mathrm{LJ}}^* = 10$), a chain gets trapped in a metastable state and stays there for a long time rather than approach its final minimum energy state. The inset of Fig. 6.4 (a) shows this trapping behavior at very large quench depths much more clearly for a MBC chain. This inset reveals that while MBC chains with $\epsilon_{\mathrm{LJ}}^* \leq 5$ have fully reached

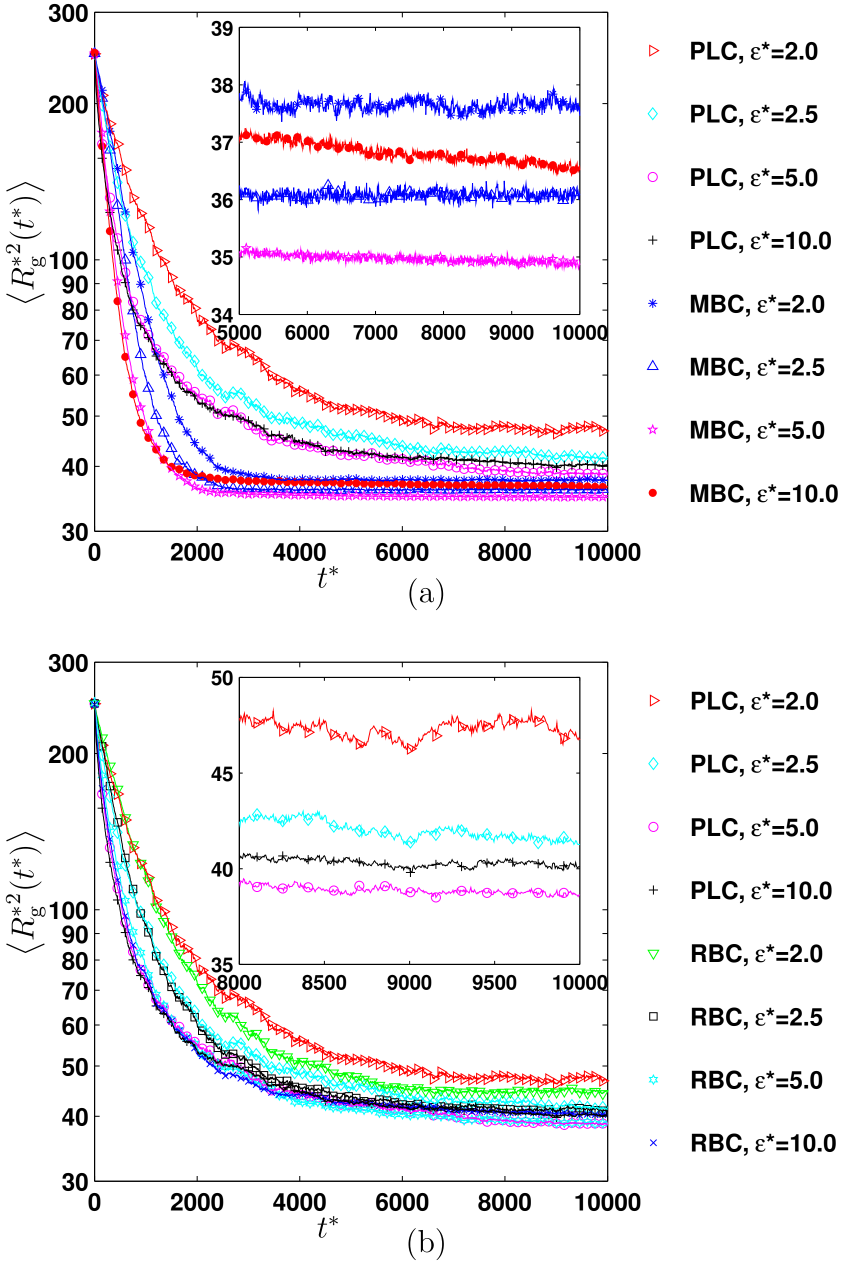

Figure 6.4: Variation of the mean square radius of gyration with time for chains with $N = 64$, in the presence of HI, for (a) PLC and MBC chains with block length of $L = 3$, and (b) PLC and RBC chains with an average block length of $\langle L \rangle = 3$. Here, ϵ^* denotes the value of the quench depth or ϵ^*_{LJ}. Insets: Variation of the mean square radius of gyration with time for chains with $N = 64$ and $L = 3$ or $\langle L \rangle = 3$ at various quench depths ϵ^*, for (a) MBC chain, and (b) PLC chain.

their equilibrium compact state, chains with $\epsilon^*_{\rm LJ} = 10$ are still gradually approaching the equilibrium state. A similar result is also observed for other types of copolymer chains (see Fig. 6.4 (b)). This trapping behavior for an implicit solvent model has also been observed by various other authors [33; 104; 158; 216]. In previous chapter, we have shown that a homopolymer chain will get trapped at $\epsilon^*_{\rm LJ} = 5$, while our current results indicate that a copolymer chain still smoothly folds at this quench depth. This result seems to indicate that the presence of P type monomers in the chain prevents it from being trapped in a local well and smooths out the energy landscape for the folding process of copolymers. This in turn pushes the value of quench depth where trapping occurs to a much higher value, when the local interaction is so strong that thermal fluctuations cannot be overcome, leading to the chain being trapped in a metastable stage.

Snapshots of the typical collapse pathways for a collapsing chain of length $N = 128$ for MBC chains are shown in Fig 6.5, and for PLC and RBC chains in Fig 6.6. From these figures, it can be seen that there exist at least two distinct stages for the kinetics of collapse for these copolymers. It is to be noted that almost all of the copolymer chains with sequences that fold into a spherical compact structure have a three-stage mechanism. The early stage involves the rapid formation of localized blobs along the chain. Following this stage, these blobs then coarsen by fusing with other nearby blobs to form a dumbbell or two pearls separated by linear chain. Finally, the pearls combine to form a sausage which slowly rearranges itself into a compact state. However, for copolymer chains with sequences consisting of short P blocks that do not fold into a spherical compact structure (for instance, MBC chains with $L \leq 2$), only the first two distinct stages is observed and the final compaction stage is not observed. Further, copolymer chains with sequences consisting of large P blocks such as MBC chains with $L = 32$ and 16, seem to acquire another distinct stage after the early rapid collapse stage, known as the "diffusion" or "plateau" regime. During this diffusion stage, the number and size of the intrachain clusters remains unchanged due to the large separation between the H blocks. Similar qualitative features of the collapse pathways have also been observed by other authors [40; 42].

The exponent α characterizing the power law decay of the mean square radius of gyration ($\langle R^2_{\rm g}(t) \rangle = \langle R^2_{\rm g}(0) \rangle - At^{\alpha}$, where A is a constant) at the initial stage of collapse is obtained by fitting a linear curve to the log-log plot of $\langle R^2_{\rm g}(0) \rangle - \langle R^2_{\rm g}(t) \rangle$ vs

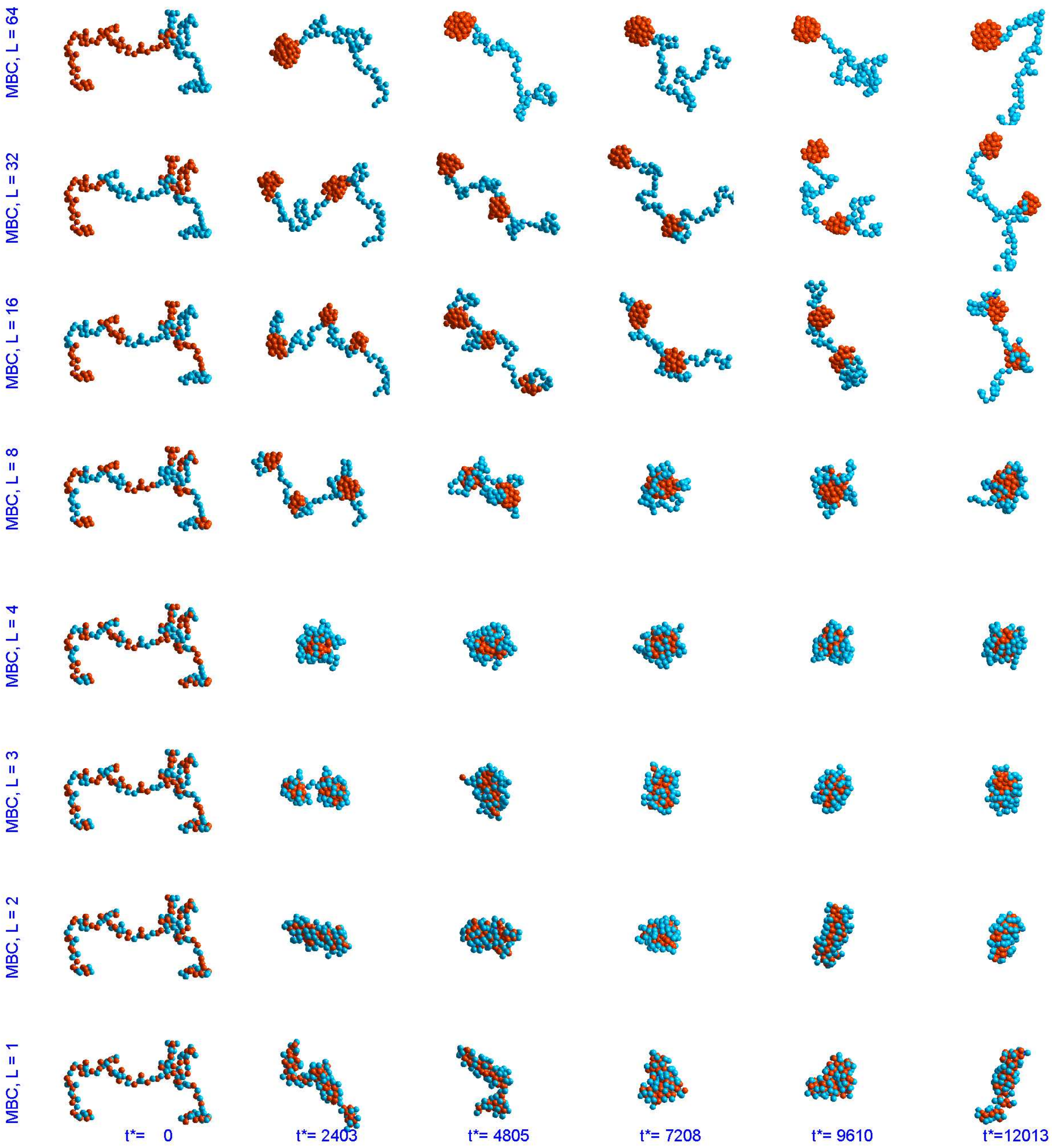

Figure 6.5: Snapshots of different types of collapsing regular multi-block copolymers (MBC) chain with $N = 128$, in the presence of HI.

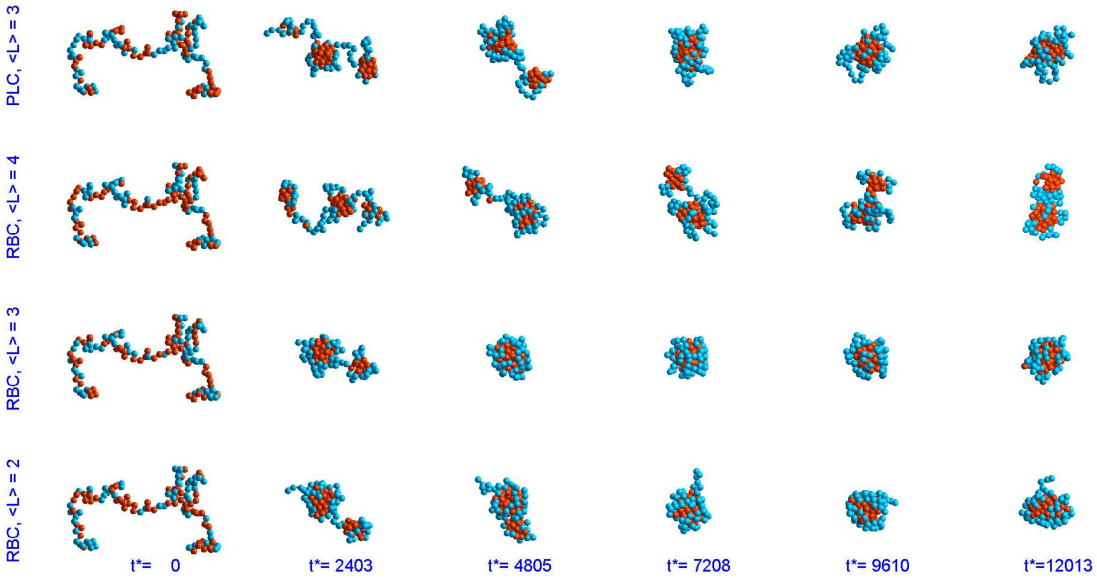

Figure 6.6: Snapshots of different types of collapsing protein-like copolymers (PLC) and random-block copolymers (RBC) chains with $N = 128$, in the presence of HI.

t. The computed values of α for all type of copolymers with different average block sizes are given in Table 6.1. The values for the cases without HI are not reported here because the chains had not reached their final equilibrium state during the course of the simulations. For a homopolymer chain at the same quench depth, we have obtained a value of $\alpha = 1.05 \pm 0.01$ with the presence of HI. Interestingly, it can be seen from Table 6.1 that there exist some copolymer chains which have a faster rate of collapse for this early stage compared to that of a homopolymer chain. Similar results have also been observed by Cooke and Williams [40] for copolymer chains in the absence of HI. Thus the presence of P type monomers along the chain speeds up the rate of collapse in the early stage of collapse for these sequences. However, most of the copolymer chains investigated in this work have a slower rate of collapse compared to that of a homopolymer chain.

The second stage of collapse is known as cluster coarsening, where previous studies of homopolymer chains indicate that a power law also holds for the growth of the average cluster size with time ($\langle S_n(t)\rangle \sim t^z$). The growth of the number average cluster size with time for a chosen value of overlapping distance $D/D_{min} = 1.20$, where, $D_{min} = 2^{1/6}(\sigma/l_H)$ is the distance at the minimum of the Lennard Jones potential, is shown in Fig. 6.7. One can clearly see from Fig. 6.7 (a) and Fig. 6.7

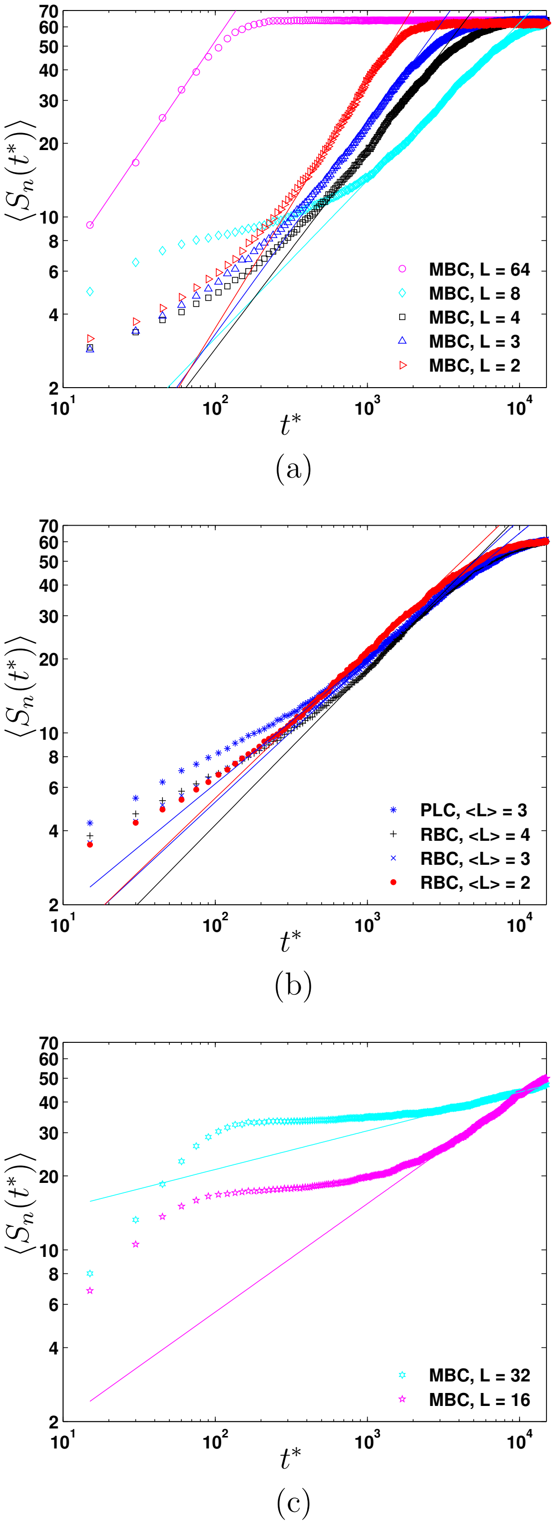

(a)

(b)

(c)

Figure 6.7: Variation of the number average cluster size with time for chains with $N = 128$ for the overlapping distance $D/D_{min} = 1.20$, in the presence of HI, for (a) MBC chains, (b) the PLC chain and RBC chains with $\langle L \rangle \leq 4$, and (c) MBC chains with $L = 32$ and 16.

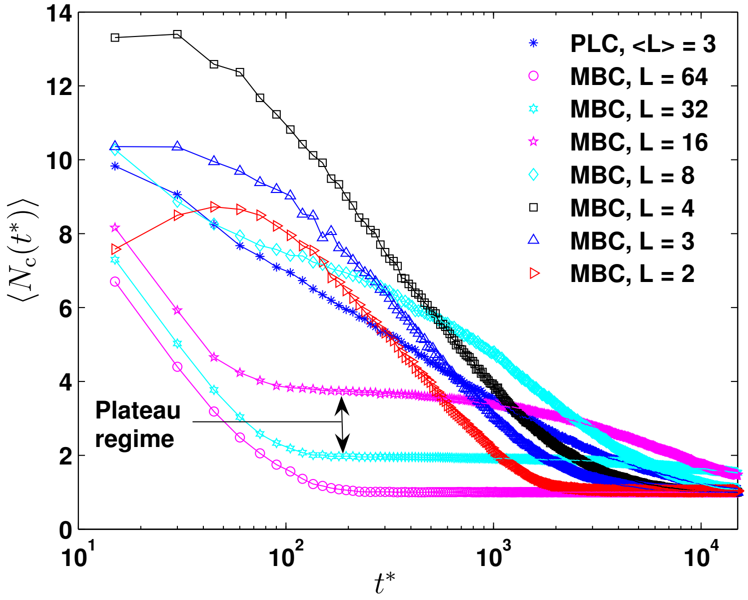

Figure 6.8: Variation of the number of clusters with time for the PLC and MBC chains with the overlapping distance $D/D_{min} = 1.20$, in the presence of HI.

(b) that there are three different regimes for the number average cluster size. Thus this result on the growth of the number average cluster size with time also confirms a three-stage collapse as has been seen earlier via observations in Figs. 6.5 and 6.6. However, for MBC chains with large block size (i.e. $L = 32$ and 16), the kinetics of collapse can be described in terms of four different regimes rather than three, where an additional regime appears between the first and second stage entirely due to diffusion. The existence of this plateau region for MBC chains with large block size is observed in Fig. 6.7 (c) and coincides with the large diffusion regime seen in Fig 6.5, where the average cluster size remains constant as coalescence has not yet occurred during this process. Since the range of attractive interaction between H type clusters is quite short compared to the size of the P block that separates them, it is necessary for these clusters of H type monomers to diffuse until they are within the range of attractive interaction to coalesce to a larger cluster. The final and fourth regime is not observed in Fig. 6.7 (c) since the chains in our simulations have not yet reached their equilibrium size after $t^* = 1.5 \times 10^4$. The appearance of a diffusion regime for MBC chains with large P block can also be identified from the plateau regions in the evolution of the number of clusters N_c with time as shown in Fig. 6.8.

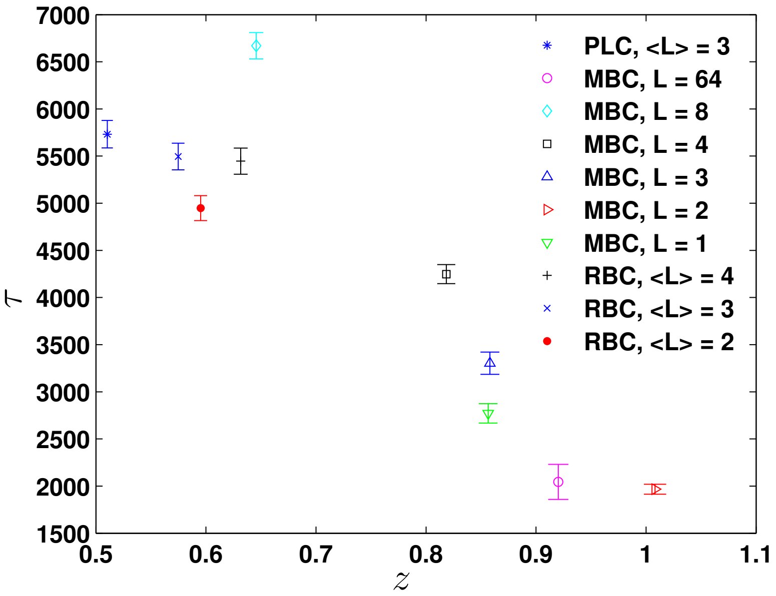

Figure 6.9: Coordinate pairs (z, τ) of the second stage exponent and total collapsed time, respectively, for all copolymer chains with $N = 128$, in the presence of HI.

Although there is no unique choice of D, we choose $D/D_{min} = 1.20$ in order to compare effects of average block size on the rate of collapse of the second stage. A similar value for D has also been used by other authors to study the exponent z for homopolymer and copolymer chains [26; 40; 158]. The values of the cluster growth exponent z at a chosen overlapping distance are obtained from the slope of a linear fit to the linear portion of the log-log plot of $\langle S_n(t^*)\rangle$ vs t^* in Fig. 6.7 for all types of copolymers with various block sizes $\langle L\rangle$. Values of z are listed in Table 6.1. Interestingly, the value of z obtained for these copolymers is always smaller than the value $z = 1.08 \pm 0.01$ reported for a homopolymer as shown in Chapter 5.

The characteristic collapse times (τ) for all three types of copolymers with $N = 128$ are shown in Table 6.1. It is observed that for all types of copolymers used in this work, the collapse time is much larger than the collapse time for a homopolymer chain, for which $\tau = 590.97 \pm 7.38$. A plot of τ vs z shown in Fig. 6.9 indicates that the total collapse time depends on the rate of collapse of the second stage, which is characterized by z. As has been pointed out earlier, MBC chains with $L = 32$ and 16 had not yet reached their equilibrium state during the course of our simulation, and hence, the the total collapse time for these two chains are not available. Careful analysis of the exponent z for MBC chains with $L \leq 32$ shows that the block size of P

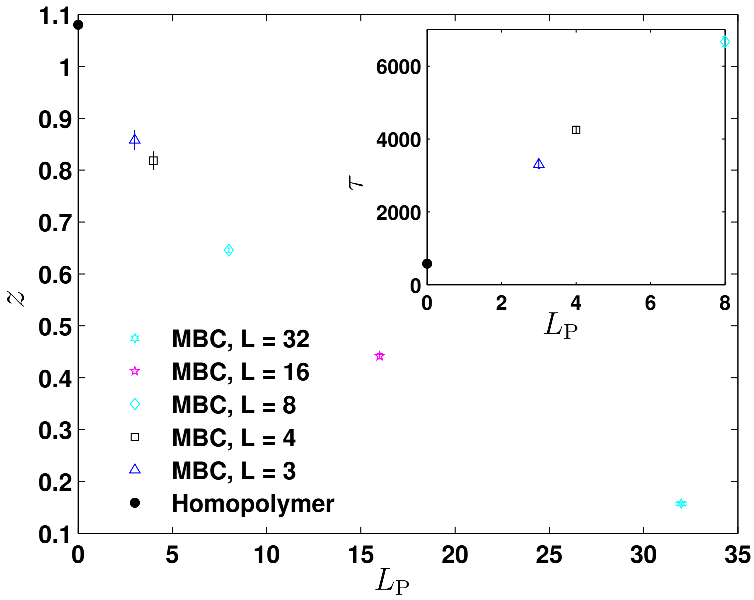

Figure 6.10: Coordinate pairs (L_{P}, z) of the block size of P type monomers and the second stage exponent, respectively, for MBC chains and a homopolymer chain with $N = 128$, in the presence of HI. Inset: The corresponding coordinate pairs (L_{P}, τ) of the block size of P type monomers and total collapse time for these chains, in the presence of HI.

type monomers has a direct influence on the value of z, with an increases in the value of z for decreasing value of P block size as seen in Fig 6.10. The inset of Fig 6.10 shows a direct relationship between the total collapse time and the P block size for MBC chains that formed a final equilibrium state with globular conformations, with a reduction in the total collapse time for decreasing P block size. The data clearly indicate that the block size of P type monomers is not only controlling the length of the diffusion process for chains with large P block size, but it also affects the rate of collapse of the cluster coarsening stage for copolymers with small P block size where diffusion plays little or no role at all. Thus one can conclude the rate of collapse of the second stage is the rate limiting factor that controls the total collapse time of a polymer chain. Since the exponent z for a homopolymer chain is always larger than for copolymer chains, this explains why the total collapse time for copolymers is much larger than that of a homopolymer.

In order to understand the relationship between the kinetic accessability of the final collapsed state and the final equilibrium size of a copolymer, we plot the chain collapse time versus its final size, in Fig. 6.11. Since not all copolymer chains fold

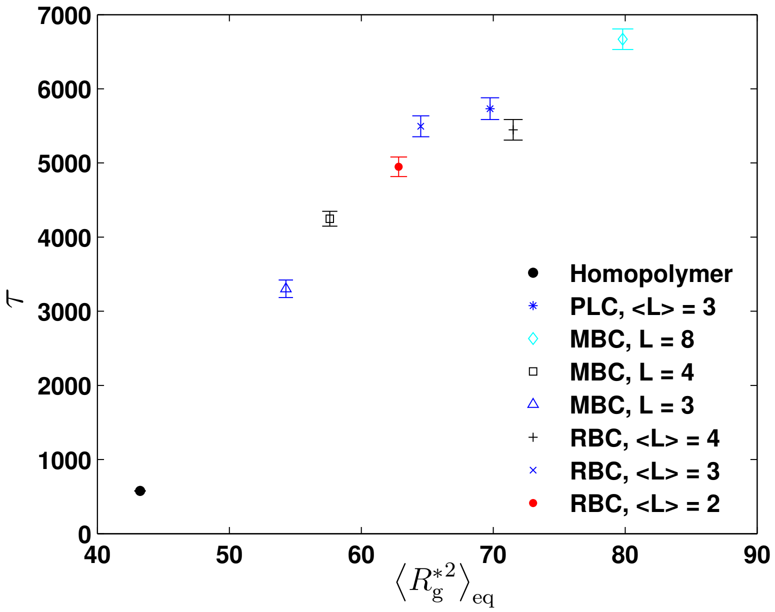

Figure 6.11: Values of the total collapse time with the equilibrium mean square radius of gyration at the final collapsed stage for all copolymers chain with $N = 128$, in the presence of HI.

into a compact globular structure, and our primary interest is in chains that form a compact state which closely resembles globular proteins, we only plotted the collapse time of selected copolymer chains that have folded into a spherical compact structure. The figure clearly shows that the chain total collapse time is directly related to its final equilibrium size. This result reveals a very interesting feature that is not expected, i.e., a chain which has a small equilibrium size tends to fold much more rapidly compared to a chain with a larger equilibrium size. Intuitively, one might expect that it would take longer for a chain to fold into a more compact equilibrium structure rather than a loosely packed structure, but these results suggest the opposite. Sali et al. [175] have pointed out that a pronounced energy minimum is a necessary condition to guarantee that the native state is stable, and it is sufficient for a compact globule with random structures to rapidly find a transition state that folds to the stable native state in a short time. Thus the deep energy minimum of the compact structure seems to provide a guide (or a strong thermodynamic driving force) for the chain to quickly fold into its final equilibrium state. In the present work, we have made no attempts to determine the free energy of the chains. However, we anticipate that knowledge of the relationship between the free energy of

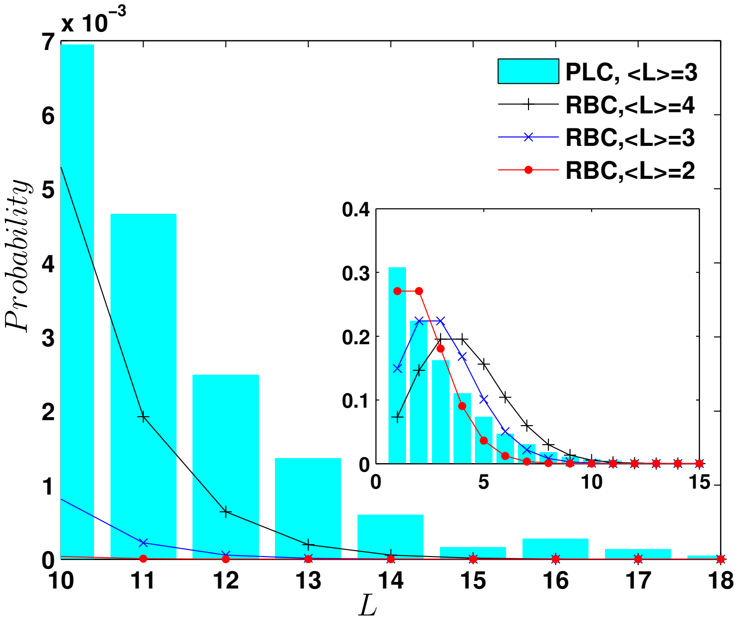

Figure 6.12: The tails of the normalized distribution of P blocks for a protein-like copolymer (PLC) and random-block copolymers (RBC) with three different average block lengths $\langle L \rangle$, for $N = 128$. Inset: The complete normalized distribution for PLC and RBC chains.

the native state and the size of the native conformation may help in resolving this behavior.

Before we discuss Fig. 6.12, we recall our earlier discussion on the kinetics of collapse for MBC chains in Fig. 6.1 (a) which showed that the presence of a large P block size leads to a less compact final collapsed size due to the formation of dangling legs of P type monomers extruding away from the core of H type monomers. Furthermore, the discussion on the rate of collapse of the second stage in Fig. 6.7 and Fig 6.10 showed that the P block size not only governs the diffusion time but it also plays an important role in the speed of the collapse of the second stage. The length of P block in a chain has a direct effect on the total collapse time because a larger P block size would induce a longer diffusion time as well as a larger cluster coalescence time for the second stage, leading to an increase in the total collapse time. Since the total collapse time and the final equilibrium size depend on the block size of P type monomers in the chain, we have plotted the block length distribution of P type monomers for PLC and RBC chains in Fig. 6.12, focusing on the tails of the distribution at large block length L (the complete distribution is shown in the inset). It can be seen that the distribution for PLC chains decays much more slowly compared to that for RBC chains, i.e. it has a longer tail. Thus on average, a PLC chain sequence is more likely to have large blocks of P type monomers compared to an RBC chain sequence. This also leads to a larger collapse time as well as a larger equilibrium size in PLC chains compared to RBC chains with the same average block size $\langle L \rangle$. Therefore, any chain with a sequence that has a long tail for the distribution of P type monomers tends to have a slow dynamics of collapse, as well as to have an increase in its final equilibrium size.

6.4 Conclusions

We have shown that Brownian dynamics simulations incorporating implicit hydrodynamic interactions can be used to study the dynamics of copolymer collapse in a poor solvent. Our simulations observations are similar to those that have been reported previously in the literature regarding the speed up of collapse caused by hydrodynamic interactions and the existence of at least two stages of collapse. The kinetics of collapse can be described as a rapid initial formation of clusters followed by cluster coalescence and sometimes a rearrangement of the clusters to form a compact state. It is also found that the presence of P type monomers pushes the value of quench depth at which the trapping phenomena occurs to a higher value compared to the value seen for homopolymer chains. A striking feature observed here is that the total collapse time is completely governed by the coarsening stage and the rate of collapse of this stage depends on the block size of P type monomers along the chain.

Chapter 7

Effects of solvent quality and chain sequence on the coil-stretch hysteresis window

7.1 Introduction

In a landmark paper in 1974, using an approximate dumbbell model, de Gennes [43] showed that the presence of hydrodynamic interactions creates large barriers in the effective steady-state free energy landscape of polymers suspended in an irrotational flow. Further, he predicted that these ergodicity breaking barriers would result in the phenomenon of coil-stretch hysteresis. A similar prediction was made by Hinch [83] at about the same time. Almost immediately after the reports of the possible occurrence of this peculiar phenomenon, several researchers [68; 84; 198] carried out more detailed numerical calculations with a dumbbell model, including nonlinear spring force laws incorporating the effects of finitely extensibility, and variable drag coefficients accounting for the change in hydrodynamic drag produced by chain deformation. They too confirmed the existence of coil-stretch hysteresis. Predictions of the occurrence of coil-stretch hysteresis using a detailed bead-spring chain model combined with the consistent-averaging technique for including hydrodynamic interactions was first reported by Magda et al. [132]. These authors predicted the existence of multiple solutions for the extensional viscosity at a particular extension rate in uniaxial extensional flow, indicating the presence of coil-stretch hysteresis. Bird and co-workers [58; 212], however, argued that the hysteretic effects predicted by de Gennes [43] were a consequence of the use of inappropriate mathematical closure approximations rather than due to the presence of variable drag acting on the beads induced by hydrodynamic interactions. Although it has subsequently been shown that indeed hysteresis does not exist at a true steady-state [17], this criticism ignored de Gennes's original observation that a quasi-steady state can still be sustained for a long period of time, which could significantly exceed typical experimental observation times. According to de Gennes, such a quasi-steady state would arise due to the existence of a large energy barrier over which the configurations of a long polymer would have to hop in order to transition between coiled and extended states.

These issues remained largely unresolved until Schroeder and co-workers [179; 180] demonstrated in 2003 for the first time that coil-stretch hysteresis does indeed exist by performing single molecule experiments and observing conformations of DNA chains at a microscopic level. In these experiments, highly extensible stained E-coli DNA molecules (1.3 mm in length, about 3.0 million base pairs) were stretched in a planar extensional flow and visualized by fluorescence microscopy. For a narrow range of flow strengths near the coil-stretch transition, the DNA molecules were found to be stable for at least 12 strain units in either a coiled or a stretched state, depending on the deformation history. They also performed Brownian dynamics simulations with a bead-spring chain model that included HI and observed similar behavior as seen in the experiments. Recently, Sridhar et al. [191] have reported experimental observations of coil-stretch hysteresis for synthetic polymers of moderate to large molecular weights using the filament stretching rheometer (FSR). In their experiments, these authors introduced a new method to measure the stress in a dilute polymer solution. In this method, the polymer solution is initially exposed to a high strain rate causing the chains to rapidly unravel and stretch. Subsequently, the strain rate is suddenly quenched into a range of values in which coil-stretch hysteresis is observed. The unique design of the FSR enables a continuous measurement of the stress during the entire period of experimental observation. With this method, they observed that different time-dependent elongational strain-rate profiles led to pronounced history dependence and aging effects within a narrow range of strain rates. In addition to experimental measurements, these authors also performed Brownian dynamics simulations with a bead-spring chain model that included HI to confirm their findings.

A theoretical explanation for the existence of hysteresis [43; 179; 180] can be briefly sketched as follows. In a uniaxial elongational flow, the nonequilibrium steady-state probability distribution function $\psi(Q)$ for a polymer molecule's end-to-end distance Q, has a Boltzmann form, $\psi(Q) \sim \exp\left[-E(Q;\dot{\varepsilon})/(k_{\mathrm{B}}T)\right]$, where, $E(Q;\dot{\varepsilon})$ is the effective nonequilibrium energy function parameterized by the strain rate $\dot{\varepsilon}$ [179; 180]. The minima in the effective energy E (with a corresponding maxima in the probability ψ) occur at the values of Q at which the total frictional force on the polymer exerted by the surrounding solvent is balanced by the entropic resistance of the molecule to stretching. For $\dot{\varepsilon} < \dot{\varepsilon}_{\mathrm{min}}$, E has a single minimum at $Q = 0$, whereas for $\dot{\varepsilon} > \dot{\varepsilon}_{\mathrm{max}}$, this minimum is shifted to a value of Q close to its maximum value of stretchable length L_{max}. However, for $\dot{\varepsilon}_{\mathrm{min}} < \dot{\varepsilon} < \dot{\varepsilon}_{\mathrm{max}}$, the existence of nonlinearities both in the drag coefficient and in the entropic spring resistance lead to two minima in E: one at $Q = 0$, and another closer to L. For molecules that are sufficiently large, the intervening maximum between the two minima can be much larger than the mean energy of thermal fluctuations in the solvent, $k_{\mathrm{B}}T$. Therefore, if an ensemble of chains is subjected to a strain rate $\dot{\varepsilon}_{\mathrm{min}} < \dot{\varepsilon} < \dot{\varepsilon}_{\mathrm{max}}$, the molecules are kinetically trapped in either the coiled or stretched state energy minimum, depending on their initial configurations. In such a circumstance, de Gennes showed that the time required for ergodicity to be fully established could be far greater than observation time scales typically encountered in experiments, even for polymer molecules of moderately large molecular weights. Using a rate theory to describe thermally activated transitions over an energy barrier, Beck and Shaqfeh [18] have recently shown that the rate of hopping between the energy minima decreases exponentially with molecular weight, indicating that in the limit of infinite system size, ergodicity is broken at strain rates that lie between the two critical values $\dot{\varepsilon}_{\mathrm{min}}$ and $\dot{\varepsilon}_{\mathrm{max}}$. As a result, there is a significant slowing of the dynamics of macroscopic observables within the "hysteresis window" for solutions of long polymer molecules.

The principal findings of studies so far of the coil-stretch hysteresis phenomenon can be briefly summarized as follows:

1. Both BD simulations and experimental observations under theta conditions have indicated that hysteretic behavior can only be observed for polystyrene molecules with a minimum molecular weight of about 5×10^5 [89; 191]. Below this chain length, the barriers to transitions between the basins of attraction are comparable to or less than $k_{\mathrm{B}}T$ at all strain rates.

2. Hysteresis only occurs for values of the ratio of effective drag coefficients in the stretched to coiled states, $\zeta_{\text{stretch}}/\zeta_{\text{coil}}$, which are 4.5 or greater. In line with the previous point, it is estimated that the value of $\zeta_{\text{stretch}}/\zeta_{\text{coil}}$ for polystyrene molecules with molecular weight of about 5×10^5 under theta condition is around 4.5 [89; 191]. Further, Hsieh and Larson [89] have estimated that the minimum molecular weight for a coil-stretch hysteresis to occur in a good solvent is seven times higher than that in a theta solvent because the coiled state is more expanded in a good solvent.

3. Under theta conditions, the longest relaxation time τ_1 scales with the molecular weight N as $\tau_1 \sim N^a$, where $a = 2$ and $3/2$ for cases without and with HI, respectively. Interestingly, the inverse of the above scaling law is observed for the molecular weight scaling of the critical strain rate $\dot{\varepsilon}_{\text{max}}$ which corresponds to the extension rate for the occurrence of a coil-stretch transition from an initially coiled state, i.e. $\dot{\varepsilon}_{\text{max}} \sim N^{-a}$ [22; 23; 29; 38; 99; 145; 146]. While each of these two properties heavily depend on HI, their product $\dot{\varepsilon}_{\text{max}}\tau_1$ (which is often referred to as the critical Deborah De_{max} or Weissenberg number Wi_{max}), remains constant at round 0.5 and is independent of HI as well as molecular weight [38; 89; 132].

4. In recent years, several groups of researchers have studied the effects of solvent quality on the molecular weight scaling of $\dot{\varepsilon}_{\text{max}}$ and τ_1. They have found that the introduction of excluded-volume interactions due to good solvent conditions does not alter the values of the exponent a for the scaling law $\dot{\varepsilon}_{\text{max}} \sim N^{-a}$ observed under theta conditions [10; 59; 67; 99; 138; 139; 144; 149]. However, the presence of excluded-volume interaction has been found to change the value of the exponent a for the scaling of the relaxation time τ_1 in the presence of HI from $a = 1.5$ for theta solvents to $a = 1.8$ for good solvents [38; 150; 172].

5. Cifre and de la Torre [38] have shown that for a fixed chain length, the value of the critical strain rate $\dot{\varepsilon}_{\text{max}}$ remains unchanged for a wide range of solvent qualities in good and in theta solvents. However, this value changes rapidly in a poor solvent, increasing as the strength of attractive interaction increases. These results suggest that the value of the exponent a for poor solvents maybe different from the value of 1.5 obtained in good and theta solvents.

Although it was found through BD simulations and through rate theory that the molecular weight of the dissolved polymer has a large influence on the size of the coil-stretch hysteresis window [18; 89], there has been no attempt so far to investigate the effects of solvent quality on the size of the hysteresis window, especially in the poor solvent regime where the ratio of effective drag coefficients $\zeta_{\text{stretch}}/\zeta_{\text{coil}}$ could exceed the minimum value of 4.5 even for short polymer molecules because the coiled state is much more compact. The present chapter aims at partially filling this unexplored gap.

In this work, we have carried out BD simulations of a FENE chain model with $N = 32$ and 64 beads, in the presence of HI, to study the effects of solvent quality on the nature of the conformational hysteresis window in extensional flows. Apart from studying solvent quality effects on a homopolymer (Ho) chain, effects of different types of interaction potentials between intrachain blocks in a diblock copolymer (Co) has also been investigated. Here, two types of diblock copolymers have been examined, where the difference between these diblock copolymers lies in the energetic interaction between the blocks in the chain. The first type is the standard good-poor diblock copolymer, which is composed of a block of P type monomers for good solvent and a block of H type monomers for poor solvent. The interactions between the beads within these two blocks are the same as those described for the copolymers used in Chapter 6. Beads that belong to different blocks interact via the repulsive interaction potential. The dimensionless forms of these potentials are given as

$$V_{\text{EV}}(r^*_{\mu\nu}) = \begin{cases} 4\epsilon^*_{\text{LJ}} \left[\dfrac{(\sigma/l_H)^{12}}{{r^*_{\mu\nu}}^{12}} - \dfrac{(\sigma/l_H)^{6}}{{r^*_{\mu\nu}}^{6}} + \dfrac{1}{4} \right] & \text{for } r^*_{\mu\nu} \leq 2^{1/6}(\sigma/l_H), \\ 0 & \text{for } r^*_{\mu\nu} > 2^{1/6}(\sigma/l_H) \end{cases} \tag{7.1}$$

$$V_{\text{attr}}(r^*_{\mu\nu}) = \begin{cases} 4\epsilon^*_{\text{LJ}} \left[\dfrac{(\sigma/l_H)^{12}}{{r^*_{\mu\nu}}^{12}} - \dfrac{(\sigma/l_H)^{6}}{{r^*_{\mu\nu}}^{6}} - c(R^*_c) \right] & \text{for } r^*_{\mu\nu} \leq R^*_c, \\ 0 & \text{for } r^*_{\mu\nu} > R^*_c \end{cases} \tag{7.2}$$

where σ is the Lennard Jones parameters, $\epsilon^*_{\text{LJ}} = \epsilon_{\text{LJ}}/k_{\text{B}}T$ is the strength of excluded volume interaction or quench depth, $r^*_{\mu\nu}$ is the distance from bead μ to bead ν. $R^*_c = 2.5(\sigma/l_H)$ is the cutoff radius and the function $c(R^*_c)$ is chosen such that the value of the potential is zero at the cutoff, i.e., $c(R^*_c) = [(\sigma/l_H)/R^*_c]^{12} - [(\sigma/l_H)/R^*_c]^{6}$.

The second type is known as the theta-poor diblock copolymer, which is made up of a theta block and a poor block. The same interactions are employed for this type of copolymer, except that there are no bead-bead interactions between the beads in the theta block as if this block is a segment of an ideal Gaussian chain. Note that all the blocks are equal in length. We use the same FENE spring potential as has been used in Chapter 5 with $\tilde{h}^* = 0.5$. For convenience, we use the equilibrium position vectors of chains that have fully reached their final collapsed state from previous simulations reported in Chapter 5 and Chapter 6 as the initial coiled configurations for this study. Chains with initially stretched configurations are generated from linear chains aligned in the flow direction that have been extended to 90% of their maximum stretchable length. For all the simulations, the product of extension rate and time step size $\dot{\epsilon}^* \Delta t^* = 0.0001$ has been used, which yielded a solution with very small discretization errors. Property values are obtained from an ensemble average of 500 statistically independent trajectories.

7.2 Results and discussion

In order to observe the effects of solvent quality on the coil-stretch conformational hysteresis window for a full range of solvent conditions, we have run simulations for chains under three different solvent regimes, namely, good, theta and poor. For good and poor solvent conditions, a value of $\epsilon^*_{\text{LJ}} = 2.50$ has been used, $\epsilon^*_{\text{LJ}} = 5.00$ is used to represent a poorer solvent condition, and bead-bead interactions are suppressed under theta conditions. Here, the dimensionless strain rate has been non-dinmensionalized by the characteristic relaxation time of a Hookean spring λ_H. The starting configurations of both initially coiled (IC) and initially stretched (IS) states have been used for these simulations.

It is observed that a majority of researchers in the field of polymer science have often used the Rouse-Zimm longest relaxation time τ_1 to rescale the strain rate and plot various properties such as stress and end-to end distance as a function of Weissenberg number. However, in practice, it is quite difficult to extract the longest relaxation time from experimental data. In presenting their experimental findings, experimentalists quite often used $\eta^*_{\text{p},0}\lambda_H$ (where $\eta^*_{\text{p},0}$ is the dimensionless zero-shear rate polymer viscosity) as the relaxation time since this quantity can be easily obtained from experiments, and it is given as

$$\eta^*_{\text{p},0}\lambda_H = \frac{\eta_0 - \eta_{\text{s}}}{n_{\text{p}} k_{\text{B}} T}, \tag{7.3}$$

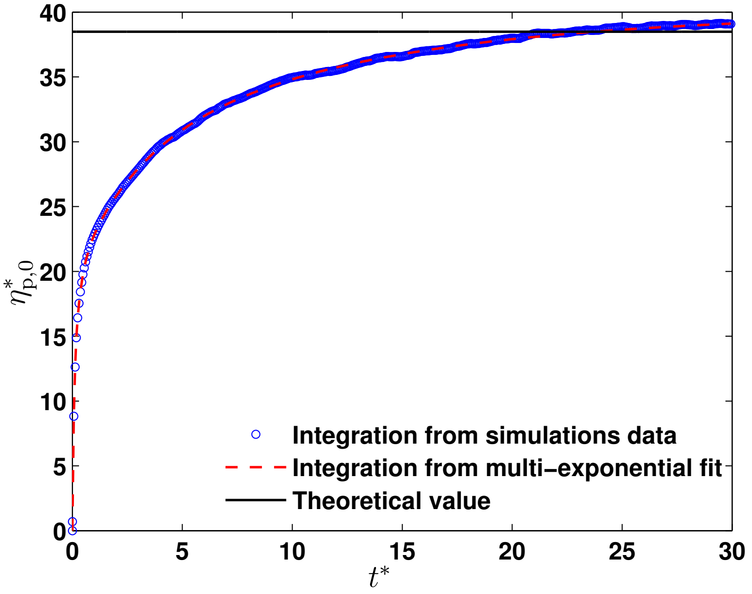

Figure 7.1: Variation of the zero-shear rate polymer viscosity with time for a homopolymer chain with $N = 8$ in a poor solvent condition, at $\epsilon^*_{\mathrm{LJ}} = 2.50$, in the absence of HI.

Table 7.1: Values of the zero-shear rate intrinsic viscosity for various types of polymer chains under different solvent conditions, in the presence of HI at $\epsilon^*_{\mathrm{LJ}} = 2.50$.

Type	Interaction	N	ϵ^*_{LJ}	$\eta^*_{\mathrm{p},0}$
Homopolymer	good	32	2.50	690.091 ± 9.510
Homopolymer	theta	32	2.50	105.495 ± 1.045
Homopolymer	poor	32	2.50	253.697 ± 19.884
Homopolymer	good	64	2.50	2437.772 ± 32.755
Homopolymer	theta	64	2.50	269.561 ± 1.301
Homopolymer	poor	64	2.50	529.313 ± 26.612
Homopolymer	poor	64	5.00	503.670 ± 20.101
Copolymer	good-poor	64	2.50	1922.758 ± 60.339
Copolymer	theta-poor	64	2.50	462.045 ± 46.732

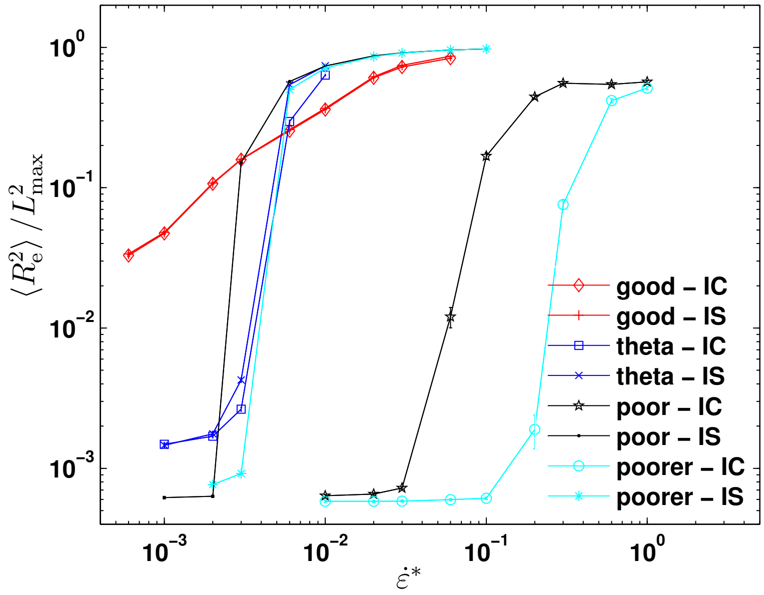

Figure 7.2: Variation of the mean square end-to-end distance with dimensionless strain rate at $\varepsilon = 10$ for a homopolymer polymer chain, at various solvent qualities. For good solvent conditions, a chain of $N = 32$ beads has been used. For all the remaining solvent conditions, chains with $N = 64$ beads have been used.

where η_0 is the solution viscosity, η_s is the solvent viscosity, and n_p is the number density of polymer.

In this work, we have used $\eta^*_{p,0}\lambda_H$ as the longest relaxation time rather than the actual Rouse-Zimm longest relaxation time τ_1, and the definition of the Weissenberg number used here is the product of $\eta^*_{p,0}\lambda_H$ and $\dot{\varepsilon}$. The zero-shear rate intrinsic viscosities reported here are obtained via the Green-Kubo formulation. The values of the zero-shear rate intrinsic viscosity obtained from simulations have also been validated with the theoretical predictions for cases without HI as reported by Prakash [167]. We have used a multi-exponential curve to fit the stress-stress autocorrelation function data obtained from simulations and have extracted the zero-shear rate viscosity by performing a numerical integration of the fitted curve. As can be seen in Fig. 7.1 this method produces a very reliable value for the zero-shear rate viscosity. Values of the zero-shear rate intrinsic viscosity for chains subjected to different static solvent conditions are listed in Table 7.1.

Figure 7.2 shows the variation of mean square end-to-end distance with dimensionless strain rate for a homopolymer chain with $N = 64$ at a Hencky strain $\varepsilon = 10$, for four different solvent conditions, except for chains in a good solvent where $N = 32$ has been used. It can be seen from the figure that conformational coil-stretch hysteresis can be observed for chains with $N = 64$ beads in theta and in poor solvents. However, there is no hysteresis for a 32 bead chain under good solvent conditions. Since, as suggested by Hsieh and Larson [89], the occurrence of coil-stretch hysteresis in a good solvent requires a chain with molecular weight at least seven times larger than that required for theta conditions, and the required simulation time exceeds our current computational resources, we have only performed simulations for a chain with $N = 32$ beads in a good solvent, which will prove to be useful later on for the analysis of copolymers with $N = 64$ in flow. The figure clearly shows that the critical strain rate $\dot{\varepsilon}^*_{\text{max}}$ for the occurrence of a coil-stretch transition is delayed further as the solvent quality decreases from good to poor. In a poor solvent, the critical strain rate $\dot{\varepsilon}^*_{\text{max}}$ for the occurrence of a coil-stretch transition increases with larger quench depth because the stronger attractive interaction has caused the coiled chain to remain in a coiled state much longer compared to that for a weaker attractive interaction. The critical strain rate $\dot{\varepsilon}^*_{\text{min}}$ for a stretch-coil transition is also higher for larger quench depth because the stronger attractive interaction has overcome the large energy barrier and allowed the stretched chain to collapse back to a coil at a higher strain rate, which does not occur for a stretched chain with a shallower quench depth. Thus the width of the hysteresis window increases with increasing attractive interaction. It is observed that the hysteresis window for the theta condition is very narrow compared to that for poor solvents and it lies within the hysteresis window of a poor solvent at $\epsilon^*_{\text{LJ}} = 2.50$.

Variation of mean square end-to-end distance with Weissenberg number for the case described above is shown in Fig. 7.3. The coil-stretch hysteresis window for a theta solvent is located at a lower Weissenberg number compared to that for a poor solvent. Although there is no coil-stretch hysteresis for a chain in a good solvent used in this work, if one takes the mid point of the change in the end-to-end distance as the point where coil-stretch transition occurs (as is frequently done in the literature [38; 146]), one can deduce that the critical Weissenberg number Wi_{max} for the coil-stretch transition is higher for good solvents compared to that for a theta solvent. Previous findings reported by various authors [38; 59; 67; 99; 138; 139; 144; 149; 150; 172] have shown that the critical Weissenberg number Wi scales as $N^{0.3}$ for good solvents while it remains constant at 0.5 for a theta solvent.

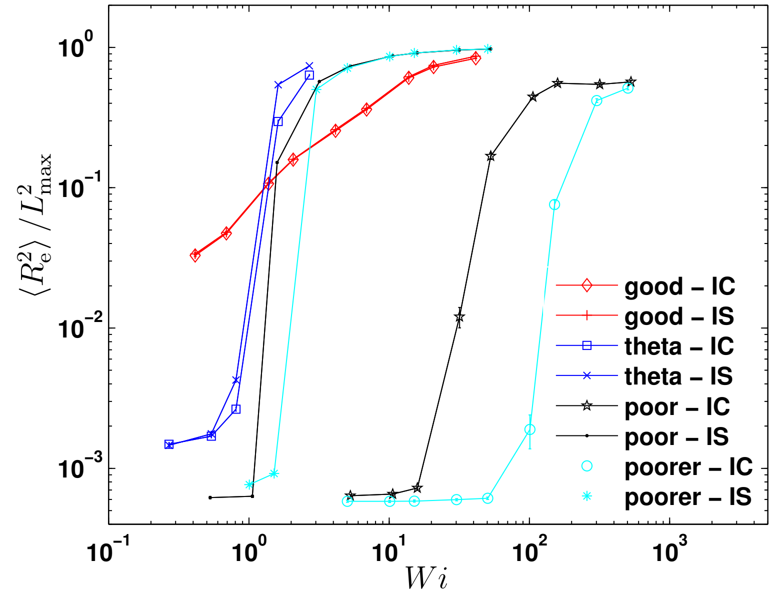

Figure 7.3: Variation of the mean square end-to-end distance with Weissenberg number at $\varepsilon = 10$ for a homopolymer polymer chain, at various solvent qualities. For good solvent condition, a chain of $N = 32$ beads is used. For all the remaining solvent conditions, chains of $N = 64$ beads are used.

This result implies that the critical Weissenberg for the occurrence of coil-stretch hysteresis is higher in good solvents compared to that in theta solvents for chains with sufficiently large molecular weight. In our simulations, we see in Fig. 7.3 that the above expectation in the shift of critical Weissenberg number $Wi_{\max}$ is true even though the chain used in the good solvent is only half the length of the chain used in the theta solvent. Moreover, it is observed that the width of the hysteresis window for a poor solvent is at least an order of magnitude higher compared to that for a theta solvent and this ratio further increases with increasing the quench depth.

In addition to the quench depth, the width of the hysteresis window for a poor solvent can also be increased by increasing the chain length as seen in Fig. 7.4, where the hysteresis window for chains with $N = 32$ is completely embedded within the window of the chains with $N = 64$. It is clear that the critical Weissenberg number for coil-stretch transition is not universal in poor solvents, and it depends on chain length even though the quench depth is kept constant. This might have to do with the fact that the solvent quality is determined not only by $\epsilon_{\rm LJ}^*$, but also by chain length [112; 113]. Since our main aim is to study the effects of solvent quality

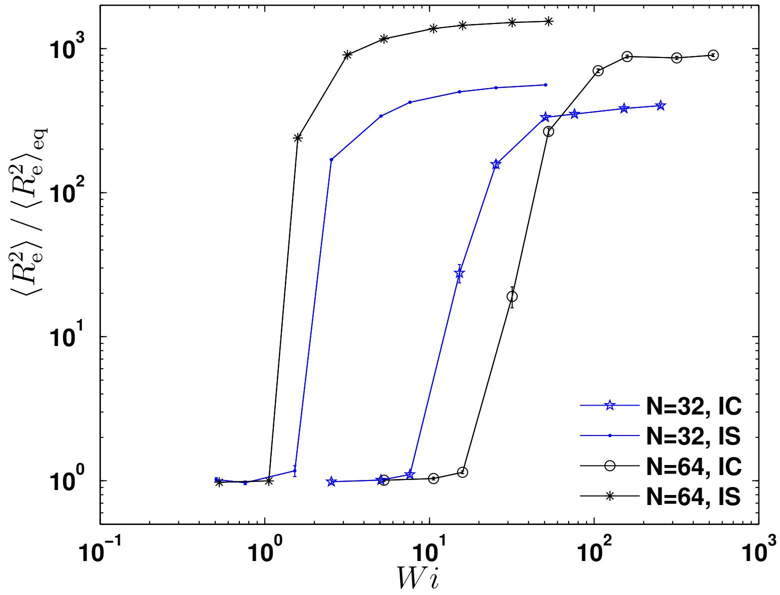

Figure 7.4: Variation of the mean square end-to-end distance with Weissenberg number at $\varepsilon = 10$ for homopolymer polymer chain with $N = 32$ and $N = 64$, at $\epsilon_{\text{LJ}}^* = 2.50$.

on the conformational hysteresis window, we have not attempted to determine the molecular weight scaling of the critical Weissenberg number for coil-stretch transition in a poor solvent. Detailed study of the molecular weight scaling of Wi_{max} in the future may help clarify these observations.

Furthermore, we have found that the width of the hysteresis window is sensitive to the value of Hencky strain at which the data is extracted and the window is narrower for larger values of Hencky strain. This is entirely in line with the expectation that hysteresis vanishes as the steady state is approached and chains have sufficient time to hop barriers [17]. The results in Fig. 7.3 suggest that from an experimental point of view, experimental observations of conformational coil-stretch hysteresis should be much easier to observe and detect for a chain in a poor solvent because the coil-stretch transition occurs at a much higher strain rate and the width of the window is significantly wider even for very short chain lengths.

Figure 7.5 shows snapshots of the typical unraveling pathways for a coiled homopolymer chain of length $N = 96$ in a poor solvent, at $\epsilon_{\text{LJ}}^* = 2.50$, which is subjected to a dimensionless strain rate of $\dot{\varepsilon}_{\text{max}}^* = 0.10$. It can be seen that *unraveling* pathways of a homopolymer chain in extensional flow are very different

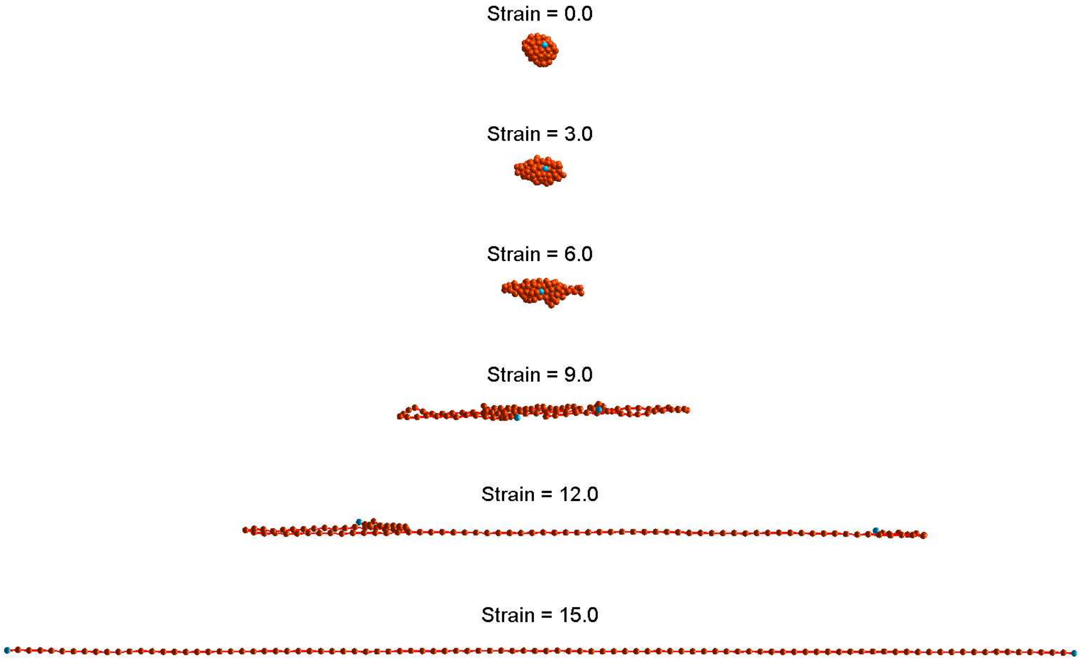

Figure 7.5: Simulation snapshots of an initially coiled chain with $N = 96$ at $\dot{\varepsilon} = 0.10$ at various values of Hencky strain ε. The ends beads are indicated with blue color.

to the *collapsing* pathways in a quiescent poor solvent. For a collapsing chain in a static poor solvent, it is observed that the chain first forms many small clusters followed by a dumbbell configuration before rearrangement to a compact globule. In extensional flow, the chain does not form strings of clusters or a dumbbell, rather it forms a chain with folded ends that are aligned along the flow direction. Due to the attractive interaction, the chain unfolds itself by sliding the folded segments at each folded end away from the chain's center until it is completely stretched out.

Typical snapshots of an initially coiled homopolymer chain of length $N = 96$ subjected to a wide range of dimensionless strain rate at $\varepsilon = 10$, in a poor solvent with $\epsilon^*_{\text{LJ}} = 2.50$, is shown in Fig. 7.6. Here, it can be seen that below a certain critical strain rate (i.e. $\dot{\varepsilon}^*_{\text{max}} < 0.10$), the chain remains in a coiled state even at a value of Hencky strain of $\varepsilon = 10$. It is interesting to note that at a certain dimensionless strain rate (i.e. $\dot{\varepsilon}^* = 0.30$), a chain appears to be stretched out to a greater length than the same chain subjected to a higher dimensionless strain rate. This behavior can be explained by the rapid stretching of the folded ends of the chain due to the strength of flow. In the presence of a flow field with strain rate greater than the

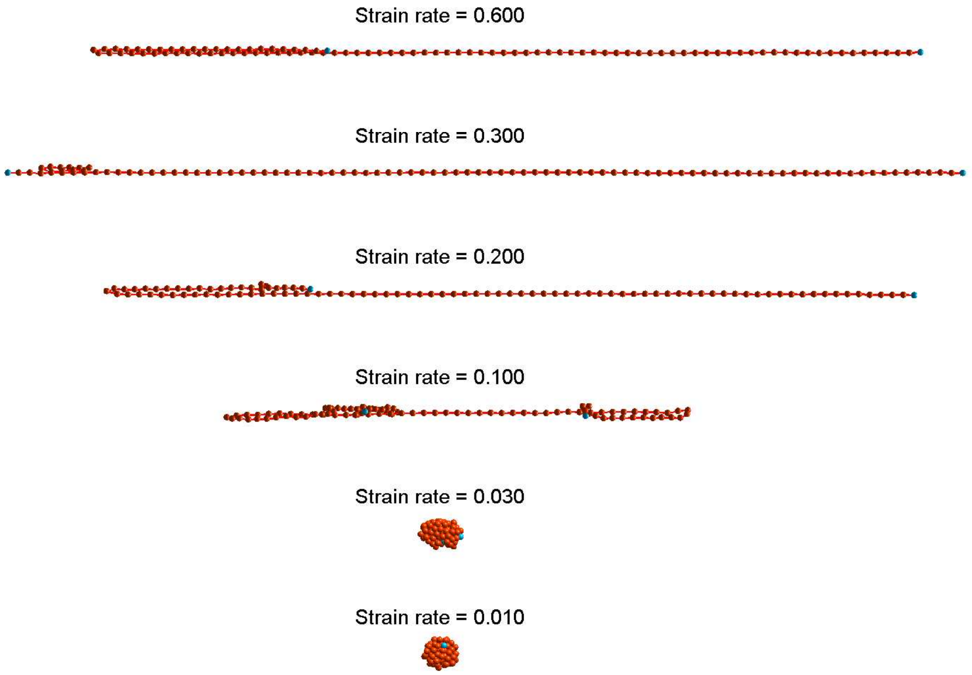

Strain rate = 0.600

Strain rate = 0.300

Strain rate = 0.200

Strain rate = 0.100

Strain rate = 0.030

Strain rate = 0.010

Figure 7.6: Simulation snapshots of an initially coiled chain with $N = 96$ at $\varepsilon = 10$ subjected to various flow strengths. The ends beads are indicated with blue color.

critical strain rate for a coil-stretch transition, the flow causes the coiled chain to unravel beginning with the parts that are exposed to the flow. This leads to the formation of folded loops at each end. However, the number of folded loops is usually not distributed evenly at each end. Since the two ends of the chain have to stretch in opposite directions, one end is likely to unraveled faster than the other. The remaining end continues to stretch such that it forms a folded end which is made up of a string with the folded part inward. Since the characteristic time scale (inverse of the extension rate) is shorter in a strong flow, we may anticipate that the number of fluctuations in chain configurations within the characteristic flow time are small. Thus it is less likely for the flow to grab the folded segments and stretch it out. As a result, beads in the string along the folded end align with the flow direction and slowly slide on top of each other due to the attractive interaction between them until they are unfolded. In contrast, the lower characteristic time scale in a weaker flow tolerates the existence of a larger number of chain configurational fluctuations. In this case, it is more likely that the flow will grab the folded end and unravel it fully. Thus in a certain range of Hencky strains and strain rates, the length of the folded end of a chain in a strong flow is longer than for a chain in a weaker flow.

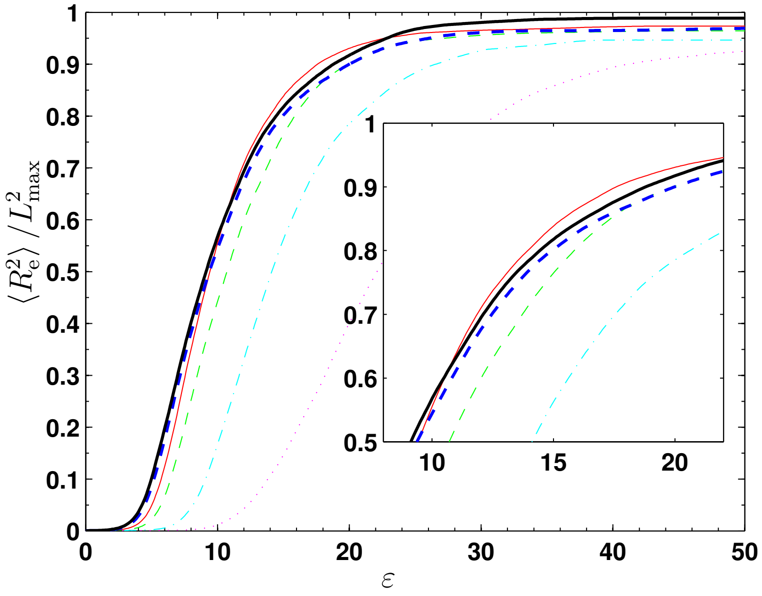

Figure 7.7: Variation of the mean square end-to-end distance with Hencky strain for a homopolymer chain in a poor solvent, with $N = 64$, at $\epsilon^*_{\text{LJ}} = 2.50$, subjected to various flow strengths. The values of dimensionless strain rate increases from right to left, beginning with $\dot{\varepsilon}^* = 0.06$ (dot-dot), $\dot{\varepsilon}^* = 0.10$ (dash-dot), $\dot{\varepsilon}^* = 0.20$ (thin dash-dash), $\dot{\varepsilon}^* = 0.30$ (thin line), $\dot{\varepsilon}^* = 0.60$ (thick dash-dash), and $\dot{\varepsilon}^* = 1.00$ (thick line). Inset: Variation of the end-to-end distance with Hencky strain focusing on the non monotonic region.

To examine if this behavior is confined to individual trajectories, or it is also a property of an ensemble of chains, we also plot the ensemble average end-to-end distance of 500 independent trajectories for a range of dimensionless strain rates and the results are shown in Fig. 7.7. The inset of Fig. 7.7 clearly shows that this non-monotonic increase in the stretching of the chain's end-to-end distance, which occurs at values of Hencky strain between 10 and 25, is also seen for an ensemble averaged property.

Snapshots of a typical initially coiled good-poor copolymer chain of length $N = 128$ subjected to a wide range of dimensionless strain rates at $\varepsilon = 10$, in a poor solvent at $\epsilon^*_{\text{LJ}} = 2.50$, is shown in Fig. 7.8. The figure shows that while the good block has been fully unraveled at $\dot{\varepsilon}^* = 0.001$, the poor block still remains in a coiled globule and only unravels at a strain rate 0.001. This visual observation suggests that it may be possible to obtain a dual coil-stretch hysteresis window provided that

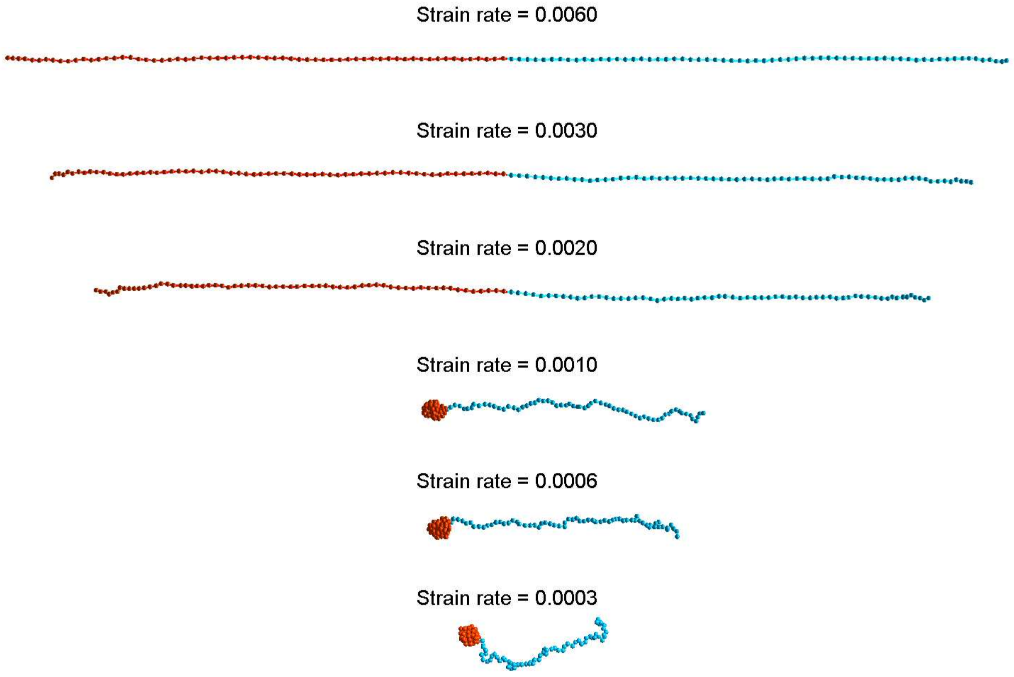

Figure 7.8: Simulations snapshot of an initially coiled good-poor diblock copolymer chain with $N = 128$ at $\varepsilon = 10$ subjected to various flow strengths.

there is a coil-stretch hysteresis window for each individual block.

Figure 7.9 (a) shows the variation of mean square end-to-end distance with dimensionless strain rate for a good-poor diblock copolymer chain in a poor solvent at $\epsilon_{\mathrm{LJ}}^* = 2.50$, with $N = 64$, at $\varepsilon = 10$, and the corresponding variation for each individual block which is a homopolymer with $N = 32$. For the good-poor diblock copolymer, it is observed that only the poor solvent block gives rise to a coil-stretch hysteresis window and there is no hysteresis window for the good solvent block with the short chain length used in this study. It is clearly shown that the good block in a good-poor copolymer begins to unravel at a lower dimensionless strain rate compared to that of the individual good block with the same chain length. Moreover, the coil-stretch transition for the poor block in a good-poor diblock copolymer with $N = 64$ occurs at much lower dimensionless strain rate compared to that for an individual poor block alone with $N = 32$. The large drag force induced from the attached poor solvent globule appears to help reduce the energy barrier, which in turn causes the chain to unravel at a much lower dimensionless strain rate. Similarly, the drag of a unraveled tethered chain due to the presence of a good block

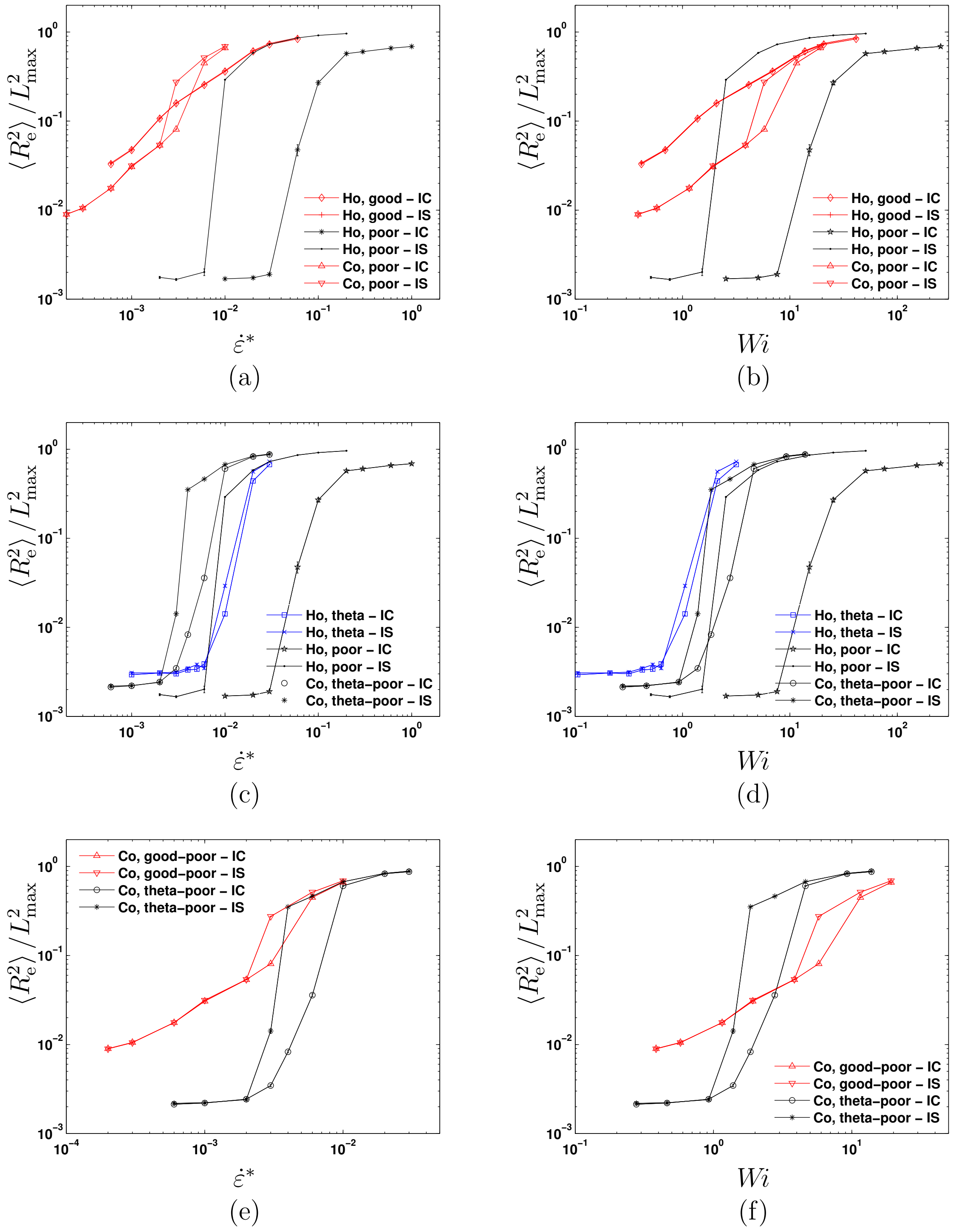

Figure 7.9: Variation of the mean square end-to-end distance with dimensionless strain rate at $\varepsilon = 10$, for (a) $N = 64$ good-poor diblock copolymer chain and the corresponding individual blocks with $N = 32$, (c) $N = 64$ theta-poor diblock copolymer chain and the corresponding individual blocks with $N = 32$, (e) a good-poor and a theta-poor diblock copolymer chain, with $N = 64$. The same combinations as a function of Wi are shown in (b), (d), and (f), respectively.

also appears to help speed up the unraveling of the poor block. Variation of the end-to-end distance with *Wi* for these chains are shown in Fig. 7.9 (b). It can be seen from the figure that the width and the height of the hysteresis window for the poor block in a good-poor copolymer are much narrower compared to that of a poor block alone. The value of Weissenberg number at which the good block in a good-poor copolymer begins to unravel is almost the same as that of the individual good block. Similar behavior is also observed for a theta-poor copolymer chain as seen in Fig. 7.9 (c). The existence of a hysteresis window for a theta block, which is completely embedded within the window of a poor block, appears to lead to the emergence of an overlapping hysteresis window for a theta-poor copolymer chain. Notably, however, the width of the hysteresis window for either copolymer chain composed of two different blocks is significantly narrower compared to the width obtained for an individual poor block with half the total chain length (see Figs. 7.9 (b) and (d)).

Figure 7.9 (e) shows that the coil-stretch transition for a good-poor copolymer chain occurs at lower dimensionless strain rate compared to a theta-poor copolymer chain. However, in term of Weissenebrg number, the coil-stretch transition for a good-poor copolymer chain is delayed to a much higher Weissenberg number compared to a theta-poor copolymer chain as can be seen in Fig. 7.9 (f). Further, the height of the hysteresis window for the theta-poor copolymer is much larger than that for a good-poor copolymer. This is perhaps related to the fact that the observed hysteresis window for a theta-poor copolymer chain is a combination of two overlapping hysteresis windows that occur within the same range of dimensionless strain rates, one for the theta block and one for the poor block. The results suggests that if the diblock copolymer chain has significantly long good and poor blocks such that coil-stretch hysteresis may be observed for the good solvent block as well, the existence of a dual coil-stretch hysteresis window is possible. Such experiments would surely be easier for one to perform than to carry out simulations due to computational limitations.

7.3 Conclusions

Brownian dynamics simulations of a nonlinear bead-spring chain model incorporating implicit hydrodynamic interactions have been carried out to study the hysteresis phenomenon of a single chain molecule in extensional flow. Our simulations for a homopolymer indicate that the occurrence of the coil-stretch transition, which is the key characteristic of polymer behavior in extensional flows, is delayed to significantly higher Weissenberg numbers in a poor solvent relative to that in theta or good solvents. Furthermore, the width of the coil-stretch hysteresis window (which can only be predicted by including HI in the model) is observed to increase by an order of magnitude in poor solvents compared to that in good or theta solvents. Diblock copolymers are found to exhibit a fascinatingly complex behavior in extensional flow. With increasing extension rate, the P block gets fully stretched while the H block remains coiled. Ultimately, a threshold value is reached at which the H block begins to unravel, and the copolymer undergoes a coil-stretch transition. For sufficiently different interaction potentials for the two blocks, it is envisaged that a dual coil-stretch hysteresis window may be observed.

Chapter 8

Conclusions

The main objective of this work has been to use Brownian dynamic simulations of bead-spring chain models incorporating implicit fluctuating hydrodynamic interactions to investigate the role of the solvent in mediating the dynamics of the collapse of a single flexible polymer molecule in dilute solution, when the solvent quality is suddenly quenched from good to poor. In such conditions, the intramolecular hydrodynamic interactions due to momentum propagation via the solvent medium plays a very crucial role in speeding up the process of collapse. More importantly, effects of hydrodynamic interactions, the strength of bead-bead interactions, and chain sequence on the dynamics of folding and on the final equilibrium size have been studied in great detail. The precise features of a copolymer sequence that controls chain kinetics as well as the size of the equilibrium compact state have been identified. In addition, predictions of the effects of solvent quality on the conformational coil-stretch hysteresis window has also been attempted via simulations of bead-spring chain models.

Before examining the kinetics of collapse of a single chain molecule, Brownian dynamic simulations have been carried out to show that a nonlinear bead-spring chain model with the SFG scheme can reproduce the predictions of the fine-grained bead-rod model. The main findings of this work on validating the model are listed below:

- In the absence of EV and HI, the analytical results for linear viscoelastic properties obtained using the bead-spring model with the SFG scheme are in complete agreement with the infinitely stiff Fraenkel spring results in the limit $N_\mathrm{s} \rightarrow N_\mathrm{k}$. This establishes that the correct limit for carrying out the extrapolation procedure when using the SFG scheme is N_k.

- The numerical computations of linear viscoelastic properties in the presence of HI are found to be in good agreement with the results of the bead-rod model. In shear flow, the SFG results show excellent agreement with bead-rod results for a range of shear rates both in the absence and presence of HI and EV. In the limit $N_\mathrm{s} \rightarrow N_\mathrm{k}$, the numerical and analytical results obtained using the SFG scheme are found to be independent of the choice of spring force law.

Since the presence of the nonlinear phenomena of intramolecular hydrodynamic interactions significantly hastens the folding process, it was worth while exploring which is the most efficient mesoscopic simulation technique to capture the effects of HI in a dilute solution. The difference between using an implicit solvent model (BD) versus an explicit solvent model (LB) was evaluated by comparing their predictions of static and dynamic properties of dilute polymer solutions. The results of this comparative study are given below:

- A mapping method on obtaining the input values for the BD simulations from the physical input parameters of the LB model such that both models would produce the same static and dynamic properties has been demonstrated.
- The static conformations of the LB model are found to be distorted when the box length L is too small compared to the chain size. For the LB model, most dynamic properties are subject to a finite-size correction of order L^{-1}, while the BD model directly reproduces the asymptotic $L \rightarrow \infty$ behavior.
- Apart from the finite box size effects, it is crucial to properly thermalize all the kinetic modes in order to obtain the correct dynamic properties for the LB simulations. It is only then that these results are in excellent agreement with each other.
- For dilute polymer solutions, Brownian Dynamics is found to be much more computationally efficient than lattice Boltzmann as long as the degree of polymerization is not excessively large.

The principal findings with regard to the collapse of homopolymers and copolymers in a quiescent solvent and their behavior in extensional flow obtained via BD simulations are summarized below.

- Simulations of a non-linear bead-spring chain model has shown that solvent mediated interactions such as bead-bead interactions and hydrodynamic interactions play an important role in the kinetics of collapse for a single polymer chain. Our predictions confirms previous observations that HI facilitates the folding, and it is observed that HI hastens the folding process by at least a factor of four for a chain with $N = 128$ beads.

- Our simulations indicate that the polymer collapse takes place via a three-stage mechanism, namely, formation of pearls, coarsening of pearls and the formation of a compact globule. Although HI is found to speed up the folding process significantly, visual inspection of the snapshots of the folding process has revealed that the presence of HI does not alter the kinetic pathways of the coil-to-globule transition. However, it is found that the kinetic pathways are significantly different for shallow and deep quenches.

- BD results also confirm that an implicit treatment of HI does not avoid the trapping phenomena, and that chains always get trapped in metastable states of local free energy minima for long periods before acquiring their native globular state at large quench depth, unlike earlier explicit solvent based MD simulations which show a smooth transition to the final global minimum free energy state.

- Two different definitions of average cluster size have been employed and it is found that the number average cluster size definition reproduces the visual observation of a three-stage collapse. Careful analysis of the growth of average cluster size in the second stage of collapse has shown that there is no universal value for the exponent z for the scaling law $\langle S_n(t) \rangle \sim t^z$ and that z is very sensitive to the value of the overlapping distance D. The exponents characterizing the decay of various properties such as the radius of gyration have been determined and they agree well with some of the theoretical predictions as well as the values reported in the literature.

- A two-letter HP code has been employed to model a copolymer chain, with hydrophobic and hydrophilic interactions with the solvent. Both these interactions are modeled as effective interactions between segments of the polymer chain using Lennard-Jones potentials with appropriately chosen cut-off distances, such that attractive interactions are switched on for H type blocks, while purely repulsive interactions are retained for P type blocks. It is found that the chain sequence has a strong influence on the kinetics of copolymer collapse as well as on the compactness and energy of its final collapsed state.

- Our simulations suggest that copolymer collapse takes place via at least two, sometimes three stages of collapse in which a rapid formation of clusters is followed by cluster coalescence with the clusters finally rearranging themselves into a compact state.

- The coloring algorithm proposed by Khokhlov and Khalatur [102] has been used to construct the protein-like copolymer chains. Multi-block and random block copolymer chains are found to collapse much faster compared to protein-like copolymer chains with the same average block length. This order of collapse amongst the three types of copolymers investigated is also found to be independent of HI and chain length.

- It is found that the presence of P type monomers along the chain pushes the value of quench depth at which the trapping phenomena occurs to a higher value compared to the value seen for homopolymer chains. Further, the presence of P type monomers also speeds up the rate of collapse in the early stage of collapse for copolymer chains. In some cases, it is found that a copolymer chain might have a larger value of the exponent α for the scaling law $\left\langle R_{\mathrm{g}}^2(0)\right\rangle - \left\langle R_{\mathrm{g}}^2(t)\right\rangle \sim t^{\alpha}$, compared to that for a homopolymer chain.

- A very interesting feature observed in this study is that the total collapse time is completely governed by the coarsening stage known as the "cluster aggregation" stage, and the rate of collapse of this stage depends on the block size of P type monomers along the chain. Any chain sequence which consists of short block lengths of P type monomers is found to collapse much faster than chain sequences with long P block lengths. In addition, the block size of P type monomers also controls the equilibrium size of the compact native state due to the formation of a dangling leg extruding away from the compact hydrophobic core when large P block lengths are present. Moreover, our results suggest that a chain that forms a small final equilibrium compact size tends to have a lower total collapse time, indicating that the size of the native compact structure also has an influence on the dynamics of folding.

- Numerical data obtained from simulations of a homopolymer shows that the critical Weissenberg number at which coil-stretch transition occurs in poor solvents strongly depends on the molecular weight of the chain. The results indicate that the value of Weissenberg number at the coil-stretch transition increases with increasing chain length. It is found that the occurrence of the coil-stretch transition is delayed to significantly higher Weissenberg numbers in a poor solvent relative to that in theta or good solvents. Furthermore, the width of the coil-stretch hysteresis window is increased by at least an order of magnitude in poor solvents compared to that in good or theta solvents.
- Diblock copolymers are found to exhibit a fascinatingly complex behavior in extensional flow. With increasing extension rate, the P block gets fully stretched while the H block remains coiled. Ultimately, a threshold value is reached at which the H block begins to unravel, and the copolymer undergoes a coil-stretch transition. For sufficiently different interaction potentials for the two blocks, it is predicted that a dual coil-stretch hysteresis window may be observed for chains with sufficiently large molecular weight such that there is a coil-stretch hysteresis window for each individual block.

Although the dynamics of collapse and the conformational coil-stretch hysteresis of a single polymer chain in a poor solvent has been studied in great detail in this thesis via BD simulations, several additional features can be implemented into the model to further improve the predictions of a polymer chain's dynamical behavior.

- In practice, a real protein chain is not only composed of hydrophobic and hydrophilic molecules but also contains charged molecules. Thus it would be worthwhile incorporating long range electrostatic interactions into our current model in order to mimic the true physical behavior of a real protein [169]. Inclusion of long range attractive electrostatic interactions due to the presence of oppositely charged molecules might lead to a chain with has faster dynamics of collapse as well as a more compact final equilibrium state compared to that for a neutral chain. Moreover, it remains interesting to see whether the dynamics of collapse is still controlled by the P block size when long range electrostatic interactions are incorporated.

- Although our results indicate that the value of critical Weissenberg number for the occurrence of a coil-stretch transition in a poor solvent increases with increasing chain length, the molecular weight scaling of this critical Weissenberg number has not been attempted due to limited number of chain lengths and dimensionless strain rates used in this study. Detailed study of the molecular weight scaling of critical Weissenberg number may help clarify this observation. Further, the exact scaling law obtained from such study can also be used to compare with existing results for good and theta solvents.
- Since our results suggest that a dual coil-stretch hysteresis window may be observed for a diblock copolymer in a poor solvent, it may even be possible to observe a triple or multiple coil-stretch hysteresis windows in a block copolymer provided that different interaction potentials between each of the blocks are tuned appropriately. Further, the addition of long range electrostatic interactions would lead to completely new and unforeseeable effects on coil-stretch hysteresis.

Bibliography

[1] Abkevich, V. I., Gutin, A. M., and Shakhnovich, E. I. (1994). Free-energy landscape for protein-folding kinetics - intermediates, traps, and multiple pathways in theory and lattice model simulations. *J. Chem. Phys.*, 101(7):6052–6062.

[2] Abrams, C. F., Lee, N. K., and Obukhov, S. P. (2002). Collapse dynamics of a polymer chain: Theory and simulation. *Europhys. Lett.*, 59(3):391–397.

[3] Adhikari, R., Stratford, K., Cates, M. E., and Wagner, A. J. (2005). Fluctuating lattice Boltzmann. *Europhys. Lett.*, 71(3):473 – 9.

[4] Agarwal, U. S. (2000). Effect of initial conformation, flow strength, and hydrodynamic interaction on polymer molecules in extensional flows. *J. Chem. Phys.*, 113(8):3397–3403.

[5] Agarwal, U. S., Bhargava, R., and Mashelkar, R. A. (1998). Brownian dynamics simulation of a polymer molecule in solution under elongational flow. *J. Chem. Phys.*, 108(4):1610–1617.

[6] Ahlrichs, P. and Dünweg, B. (1998). Lattice Boltzmann simulation of polymer-solvent systems. *Int. J. Mod. Phys. C*, 9(8):1429–1438.

[7] Ahlrichs, P. and Dünweg, B. (1999). Simulation of a single polymer chain in solution by combining lattice Boltzmann and molecular dynamics. *J. Chem. Phys.*, 111(17):8225–8239.

[8] Ahlrichs, P., Everaers, R., and Dünweg, B. (2001). Screening of hydrodynamic interactions in semidilute polymer solutions: A computer simulation study. *Phys. Rev. E*, 64(4, Part 1).

[9] Allison, S. A. and McCammon, J. A. (1984). Multistep Brownian dynamics - Application to short wormlike chains. *Biopolymers*, 23(2):363–375.

[10] Andrews, N. C., Doufas, A. K., and McHugh, A. J. (1998). Effect of solvent quality on the rheological and rheooptical properties of flexible polymer solutions. *Macromolecules*, 31(9):3104–3108.

[11] Anfinsen, C. B. (1973). Principles that govern folding of protein chains. *Science*, 181:223–230.

[12] Anfinsen, C. B., Haber, E., Sela, M., and White, F. H. (1961). Kinetics of formation of native ribonuclease during oxidation of reduced polypeptide chain. *Proc. Natl. Acad. Sci. USA*, 47(9):1309–&.

[13] Auton, M. and Bolen, D. W. (2007). Application of the transfer model to understand how naturally occuring osmolytes affect protein stability. *Methods Enzymol.*, 428:397–418.

[14] Baldwin, R. L. (1994). Matching speed and stability. *Nature*, 369:183–184.

[15] Baldwin, R. L. (1995). The nature of protein folding pathways: The classical versus the new view. *J. Biomolec. NMR*, 5:103–109.

[16] Banchio, A. and Brady, J. (2003). Accelerated Stokesian dynamics: Brownian motion. *J. Chem. Phys.*, 118(12):10323 – 32.

[17] Beck, V. A. and Shaqfeh, E. S. G. (2006). Ergodicity breaking and conformational hysteresis in the dynamics of a polymer tethered at a surface stagnation point. *J. Chem. Phys.*, 124(9):094902–1–16.

[18] Beck, V. A. and Shaqfeh, E. S. G. (2007). Ergodicity-breaking and the unraveling dynamics of a polymer in linear and nonlinear extensional flows. *J. Rheol.*, 51(3):561–574.

[19] Benzi, R., Succi, S., and Vergassola, M. (1992). The Lattice Boltzmann equation: theory and applications. *Phys. Rep.*, 222(3):145 – 97.

[20] Binder, K. (1995). *Monte Carlo and Molecular Dynamics Simulation in Polymer Science*. Clarendon, Oxford.

[21] Bird, R. B., Armstrong, R. C., and Hassager, O. (1987a). *Dynamics of Polymeric Liquids - Volume 1: Fluid Mechanics*. John Wiley, New York, second edition.

[22] Bird, R. B., Curtiss, C. F., Armstrong, R. C., and Hassager, O. (1987b). *Dynamics of Polymeric Liquids - Volume 2: Kinetic Theory*. John Wiley, New York, second edition.

[23] Bird, R. B., Saab, H. H., Dotson, P. J., and Fan, X. J. (1983). Macromolecular extension in flow-fields. *J. Chem. Phys.*, 79(11):5729–5730.

[24] Bratko, D. and Dawson, K. A. (1993). A mean field approach to the structure of polyelectrolytes. *J. Chem. Phys.*, 99(7):5352 – 5361.

[25] Buguin, A., Wyart, F. B., and deGennes, P. G. (1996). Collapse of a flexible coil in a poor solvent. *C. R. Acad. Sci., Ser. IIb: Mec., Phys., Chim., Astron.*, 322(10):741–746.

[26] Byrne, A., Kiernan, P., Green, D., and Dawson, K. A. (1995). Kinetics of homopolymer collapse. *J. Chem. Phys.*, 102(1):573–577.

[27] Camacho, C. J. and Thirumalai, D. (1993a). Kinetics and thermodynamics of folding in model proteins. *Proc. Natl. Acad. Sci. USA*, 90(13):6369–6372.

[28] Camacho, C. J. and Thirumalai, D. (1993b). Minimum energy compact structures of random sequences of heteropolymers. *Phys. Rev. Lett.*, 71(15):2505–2508.

[29] Cathey, C. A. and Fuller, G. G. (1990). The optical and mechanical response of flexible polymer-solutions to extensional flow. *J. Non-Newtonian Fluid Mech.*, 34(1):63–88.

[30] Chan, H. S. and Dill, K. A. (1991). Polymer principles in protein-structure and stability. *Annu. Rev. Biophys. Chem.*, 20:447–490.

[31] Chan, H. S. and Dill, K. A. (1994). Transition states and folding dynamics of proteins and heteropolymers. *J. Chem. Phys.*, 100.

[32] Chan, H. S. and Dill, K. A. (1996). Comparing folding codes for proteins and polymers. *Proteins-Structure Function And Bioinformatics*, 24(3):335–344.

[33] Chang, R. and Yethiraj, A. (2001). Solvent effects on the collapse dynamics of polymers. *J. Chem. Phys.*, 114(17):7688–7699.

[34] Chen, S. and Doolen, G. D. (1998). Lattice boltzmann method for fluid flows. *Annu. Rev. Fluid Mech.*, 30:329–364.

[35] Chen, Y.-L., Ma, H., Graham, M. D., and Pablo, J. J. D. (2007). Modeling dna in confinement: A comparison between the Brownian dynamics and lattice Boltzmann method. *Macromolecules*, 40(16):5978 – 5984.

[36] Chu, B., Ying, Q., and Grosberg, A. Y. (1995). Two-stage kinetics of single-chain collapse. polystyrene in cyclohexane. *Macromolecules*, 28(1):180–189.

[37] Cieplak, M. and Niewieczerzal, S. (2009). Hydrodynamic interactions in protein folding. *J. Chem. Phys.*, 130(12):124906 (R).

[38] Cifre, J. G. H. and de la Torre, J. G. (1999). Steady-state behaviour of dilute polymers in elongational flow. Dependence of the critical elongational rate on chain length, hydrodynamic interaction, and excluded volume. *J. Rheol.*, 43(2):339–358.

[39] Cohen, A. (1991). A pade approximant to the inverse langevin function. *Rheol. Acta*, 30(3):270 – 272.

[40] Cooke, I. R. and Williams, D. R. M. (2003). Collapse dynamics of block copolymers in selective solvents: Micelle formation and the effect of chain sequencee. *Macromolecules*, 36(6):2149–2157.

[41] Creigton, T. E. (1994). *Protein Folding.* Freeman, New York.

[42] Dasmahapatra, A. K., Kumaraswamy, G., and Nanavati, H. (2006). Collapse transition in random copolymer solutions. *Macromolecules*, 39(26):9621–9629.

[43] de Gennes, P.-G. (1974). Coil-stretch transition of dilute flexible polymers under ultrahigh velocity gradients. *J. Chem. Phys.*, 60:5030–5042.

[44] de Gennes, P.-G. (1979). *Scaling concepts in polymer physics.* Cornell University Press, Ithaca.

[45] de Gennes, P.-G. (1985). Kinetics of collapse for a flexible coil. *Phys. Rev. Lett.*, 46(14):639 – 642.

[46] des Cloizeaux, J. and Jannink, G. (1990). *Polymer in solution.* Clarendon Press, Oxford, New York.

[47] Dill, K. A. (1985). Theory for the folding and stability of globular-proteins. *Biochemistry*, 24(6):1501–1509.

[48] Dill, K. A. and Chan, H. S. (1997). From Levinthal to pathways to funnels. *Nature Struct. Biol.*, 4(1):10–19.

[49] Dittrich, P. S. and Manz, A. (2005). Single-molecule fluorescence detection in microfluidic channels - the Holy Grail in μtas? *Anal. Bioanal. Chem.*, 382(8):1771–1782.

[50] Doi, M. and Edwards, S. F. (1986). *The Theory of Polymer Dynamics.* Clarendon Press, Oxford, New York.

[51] Doyle, P. S. and Shaqfeh, E. S. G. (1998). Dynamic simulations of freely draining, flexible bead-rod chains: Start-up of extensional and shear flow. *J. Non-Newtonian Fluid Mech.*, 76:43–78.

[52] Doyle, P. S., Shaqfeh, E. S. G., and Gast, A. P. (1997). Dynamic simulation of freely draining flexible polymers in steady linear flows. *J. Fluid Mech.*, 334:251–291.

[53] Dünweg, B. and Kremer, K. (1993). Molecular dynamics simulation of a polymer chain in solution. *J. Chem. Phys.*, 99(9):6983–6997.

[Dünweg and Ladd] Dünweg, B. and Ladd, A. J. C. Lattice Boltzmann simulations of soft matter systems. *Cond. Mat. Archive cond-mat/0803.2826v1, 2008.*

[54] Dünweg, B., Schiller, U. D., and Ladd, A. J. C. (2007). Statistical mechanics of the fluctuating lattice Boltzmann equation. *Phys. Rev. E*, 76(3):036704.

[55] Ermak, D. L. and McCammon, J. A. (1978). Brownian dynamics with hydrodynamic interactions. *J. Chem. Phys.*, 69:1352–1360.

[56] Espanol, P. (1998). Stochastic differential equations for non-linear hydrodynamics. *Physica A*, 248(1-2):77 – 96.

[57] Espanol, P. and Warren, P. (1995). Statistical mechanics of dissipative particle dynamics. *Europhys. Lett.*, 30(4):191 – 6.

[58] Fan, X. J., Bird, R. B., and Renardy, M. (1985). Configuration-dependent friction coefficients and elastic dumbbell rheology. *J. Non-Newtonian Fluid Mech.*

[59] Farrell, C. J., Keller, A., Miles, M. J., and Pope, D. P. (1980). Conformational relaxation-time in polymer-solutions by elongational flow experiments .1. Determination of extensional relaxation-time and its molecular-weight dependence. *Polymer.*

[60] Fersht, A. R. (1995). Optimization of rates of protein-folding: The nucleation-condensation mechanism and its implications. *Proc. Natl. Acad. Sci. USA*.

[61] Fixman, M. (1978). Simulation of polymer dynamics .1. General theory. *J. Chem. Phys.*, 69(4):1527–1537.

[62] Fixman, M. (1981). Inclusion of hydrodynamic interaction in polymer dynamical simulations. *Macromolecules*, 14(6):1710–1717.

[63] Fixman, M. (1983). Effects of fluctuating hydrodynamic interaction. *J. Chem. Phys.*, 78(3):1594–1599.

[64] Fixman, M. (1986). Construction of Langevin forces in the simulation of hydrodynamic interaction. *Macromolecules*, 19:1204–1207.

[65] Flory, P. J. (1988). *Statistical Mechanics of Chain Molecules.* Oxford University, New York.

[66] Frembgen-Kesner, T. and Elcock, A. H. (2009). Striking effects of hydrodynamic interactions on the simulated diffusion and folding of proteins. *J. Chem. Theo. Comp.*, 5(2):242–256.

[67] Fuller, G. G. and Leal, L. G. (1980). Flow birefringence of dilute polymer-solutions in two-dimensional flows. *Rheol. Acta*, 19(5):580–600.

[68] Fuller, G. G. and Leal, L. G. (1981). The effects of conformation-dependent friction and internal viscosity on the dynamics of the non-linear dumbbell model for a dilute polymer-solution. *J. Non-Newtonian Fluid Mech.*, 8(3-4):271–310.

[69] Ganazzoli, F. (2000). Globular state of random copolymers with arbitrary amphiphilicity. *J. Chem. Phys.*, 112(3):1547–1553.

[70] Ghosh, I., McKinley, G. H., Brown, R. A., and Armstrong, R. C. (2001). Deficiencies of FENE dumbbell models in describing the rapid stretching of dilute polymer solutions. *J. Rheol.*, 45(3):721–758.

[71] Go, N. and Taketomi, H. (1978). Respective roles of short-range and long-range interactions in protein folding. *Proc. Natl. Acad. Sci. USA*, 75(2):559–563.

[72] Gompper, G., Ihle, T., Kroll, D. M., and Winkler, R. G. (2009). Multi-particle collision dynamics: A particle-based mesoscale simulation approach to the hydrodynamics of complex fluids. *Adv. Polym. Sci.*, 221:1–87.

[73] Grassberger, P. (1997). Pruned-enriched Rosenbluth method: Simulations of theta polymers of chain length up to 1,000,000. *Phys. Rev. E*, 56(3):3682–3693.

[74] Groot, R. and Warren, P. (1997). Dissipative particle dynamics: Bridging the gap between atomistic and mesoscopic simulation. *J. Chem. Phys.*, 107(11):4423 – 4435.

[75] Grosberg, A. Y., Nechaev, S. K., and Shakhnovich, E. I. (1988). The role of topological constraints in the kinetics of collapse of macromolecules. *J. Phys. (Paris)*, 49(12):2095–2100.

[76] Gutin, A. M., Abkevich, V. I., and I., S. E. (1995a). Evolution-like selection of fast-folding model proteins. 92(5):1282–1286.

[77] Gutin, A. M., Abkevich, V. I., and I., S. E. (1995b). Is burst hydrophobic collapse necessary for protein-folding. *Proc. Natl. Acad. Sci. USA*, 34(9):3066–3076.

[78] Hagen, S. J., Hofrichter, J., Szabo, A., and Eaton, W. A. (1996). Diffusion-limited contact formation in unfolded cytochrome c: Estimating the maximum rate of protein folding. *Proc. Natl. Acad. Sci. USA*, 93(21):11615 – 11617.

[79] Halperin, A. (1991). On the collapse of multiblock copolymers. *Macromolecules*, 24(6):1418–1419.

[80] Halperin, A. and Goldbart, P. M. (1999). Early stages of homopolymer collapse. *Phys. Rev. E*, 60(5):2111–2124.

[81] Hayes, B. (1998). Prototeins. *American Scientist*, 86(3):216–221.

[82] Hernandez-Ortiz, J. P., de Pablo, J. J., and Graham, M. D. (2007). Fast computation of many-particle hydrodynamic and electrostatic interactions in a confined geometry. *Phys. Rev. Lett.*, 98(14):140602 – 1.

[83] Hinch, E. J. (1974). *Proceedings of Colloques Internationaux du C.N.R.S. on "Polymeres et Lubrification"*. CNRS, Paris, Vol. 233, p. 241.

[84] Hinch, E. J. (1977). Mechanical models of dilute polymer-solutions in strong flows. *Phys. Fluids*, 20(10):S22–S30.

[85] Hinch, E. J. (1994). Brownian-motion with stiff bonds and rigid constraints. *J. Fluid Mech.*, 271:219–234.

[86] Hoogerbrugge, P. J. and Koelman, J. M. V. A. (1992). Simulating microscopic hydrodynamic phenomena with dissipative particle dynamics. *Europhys. Lett.*, 19(3):155 – 60.

[87] Hsieh, C.-C., Jain, S., and Larson, R. G. (2006). Brownian dynamics simulations with stiff finitely extensible nonlinear elastic-fraenkel springs as approximations to rods in bead-rod models. *J. Chem. Phys.*, 124:044911.

[88] Hsieh, C.-C. and Larson, R. G. (2004). Modeling hydrodynamic interaction in Brownian dynamics: Simulations of extensional and shear flows of dilute solutions of high molecular weight polystyrene. *J. Rheol.*, 48:995–1021.

[89] Hsieh, C.-C. and Larson, R. G. (2005). Prediction of coil-stretch hysteresis for dilute polystyrene molecules in extensional flow. *J. Rheol.*, 49(5):1081–1089.

[90] Hsieh, C.-C., Li, L., and Larson, R. G. (2003). Modeling hydrodynamic interaction in Brownian dynamics: Simulations of extensional flows of dilute solutions of DNA and polystyrene. *J. Non-Newtonian Fluid Mech.*, 113:147–191.

[91] Huang, G. S. and Oas, T. G. (1995). Submillisecond folding of monomeric λ repressor. *Proc. Natl. Acad. Sci. USA*, 92(15):6878–6882.

[92] Hur, J. S., Shaqfeh, E. S. G., and Larson, R. G. (2000). Brownian dynamics simulations of single DNA molecules in shear flow. *J. Rheol.*, 44:713–742.

[93] Ikai, A. and Tanford, C. (1971). Kinetic evidence for incorrectly folded intermediate states in refolding of denatured proteins. *Nature*, 230(5289):100–&.

[94] Jackson, S. E. (1998). How do small single-domain proteins fold? *Fold. Des.*, 3(4):R81–R91.

[95] Jackson, S. E. and Fersht, A. R. (1991). Folding of chymotrypsin inhibitor-2 .1. Evidence for a 2-state transition. *Biochemistry*, 30(43):10428–10435.

[96] Jendrejack, R. M., de Pablo, J. J., and Graham, M. D. (2002). Stochastic simulations of DNA in flow: Dynamics and the effects of hydrodynamic interactions. *J. Chem. Phys.*, 116:7752–7759.

[97] Jiang, W., Huang, J., Wang, Y., and Laradji, M. (2007). Hydrodynamic interaction in polymer solutions simulated with dissipative particle dynamics. *J. Chem. Phys.*, 126(4):44901 – 1.

[98] Kayaman, N., Gürel, E. E., Baysal, B. M., and Karasz, F. E. (1999). Kinetics of coil-globule collapse in poly(methyl methacrylate) in dilute solutions below θ temperatures. *Macromolecules*, 32(25):8399–8403.

[99] Keller, A. and Odell, J. A. (1985). The extensibility of macromolecules in solution - A new focus for macromolecular science. *Colloid Polym. Sci.*, 263(3):181–201.

[100] Keunings, R. (2001). Advances in the computer modeling of the flow of polymeric liquids. *Comp. Fluid Dyn. J.*, 9:449–458.

[101] Khokhlov, A. R. and Khalatur, P. G. (1998). Protein-like copolymers: Computer simulation. *Physica A*, 249(1-4):253–261.

[102] Khokhlov, A. R. and Khalatur, P. G. (1999). Conformation-dependent sequence design (engineering) of AB copolymers. *Phys. Rev. Lett.*, 82(17):3456–3459.

[103] Kikuchi, N., Gent, A., and Yeomans, J. M. (2002). Polymer collapse in the presence of hydrodynamic interactions. *Eur. Phys. J. E*, 9(1):63–66.

[104] Kikuchi, N., Ryder, J. F., Pooley, C. M., and Yeomans, J. M. (2005). Kinetics of the polymer collapse transition: The role of hydrodynamics. *Phys. Rev. E*, 71(6):61804 – 1.

[105] Kirkwood, J. G. (1954). The general theory of irreversible processes in solutions of macromolecules. *J. Polym. Sci.*, 12(67):1–14.

[106] Kirkwood, J. G. and Riseman, J. (1948). The intrinsic viscosities and diffusion constants of flexible macromolecules in solution. *J. Chem. Phys.*, 16(6):565–573.

[107] Klushin, L. I. (1998). Kinetics of a homopolymer collapse: Beyond the Rouse-Zimm scaling. *J. Chem. Phys.*, 108(18):7917–7920.

[108] Knudsen, K. D., de la Torre, J. G., and Elgsaeter, A. (1996). Gaussian chains with excluded volume and hydrodynamic interaction: Shear rate dependence of radius of gyration, intrinsic viscosity and flow birefringence. *Polymer*, 37(8):1317–1322.

[109] Kopf, A., Duenweg, B., and Paul, W. (1997). Dynamics of polymer 'isotope' mixtures: molecular dynamics simulation and Rouse model analysis. *J. Chem. Phys.*, 107(17):6945 – 6955.

[110] Kramers, A. H. (1946). The behavior of macromolecules in inhomogeneous flow. *J. Chem. Phys.*, 14(7):415–424.

[111] Kremer, K. and Grest, G. S. (1990). Dynamics of entangled linear polymer melts: a molecular-dynamics simulation. *J. Chem. Phys.*, 92(8):5057 – 5086.

[112] Kumar, K. S. and Prakash, J. R. (2003). Equilibrium swelling and universal ratios in dilute polymer solutions: Exact Brownian dynamics simulations for a delta function excluded volume potential. *Macromolecules*, 36:7842–7856.

[113] Kumar, K. S. and Prakash, J. R. (2004). Universal consequences of the presence of excluded volume interactions in dilute polymer solutions undergoing shear flow. *J. Chem. Phys.*, 121:3886–3897.

[114] Kuznetsov, Y. A., Timoshenko, E. G., and Dawson, K. A. (1995). Kinetics at the collapse transition of homopolymers and random copolymers. *J. Chem. Phys.*, 103(11):4807–4818.

[115] Kuznetsov, Y. A., Timoshenko, E. G., and Dawson, K. A. (1996). Kinetic laws at the collapse transition of a homopolymer. *J. Chem. Phys.*, 104(9):3338–3347.

[116] Ladd, A. J. C. (1994a). Numerical simulations of particulate suspensions via a discretized Boltzmann equation. 1. Theoretical foundation. *J. Fluid Mech.*, 271:285 – 309.

[117] Ladd, A. J. C. (1994b). Numerical simulations of particulate suspensions via a discretized Boltzmann equation. 2. Numerical results. *J. Fluid Mech.*, 271:311 – 339.

[118] Ladd, A. J. C. and Verberg, R. (2001). Lattice-Boltzmann simulations of particle-fluid suspensions. *J. Stat. Phys.*, 104:1191–1251.

[119] Larson, R. G. (2005). The rheology of dilute solutions of flexible polymers: Progress and problems. *J. Rheol.*, 49(5):1–70.

[120] Larson, R. G., Hu, H., Smith, D. E., and Chu, S. (1999). Brownian dynamics simulations of a DNA molecule in an extensional flow field. *J. Rheol.*, 43(2):267–304.

[121] Larson, R. G., Perkins, T. T., Smith, D. E., and Chu, S. (1997). Hydrodynamics of a DNA molecule in a flow field. *Phys. Rev. E*, 55(2):1794–1797.

[122] Lau, K. F. and Dill, K. A. (1989). A lattice statistical-mechanics model of the conformational and sequence-spaces of proteins. *Macromolecules*, 22(10):3986–3997.

[123] Lee, S. H. and Kapral, R. (2006). Mesoscopic description of solvent effects on polymer dynamics. *J. Chem. Phys.*, 124(21):214901.

[124] Levinthal, C. (1968). Are there pathways for protein folding. *J. Chim. Phys.*, 65(1):44–45.

[125] Li, L. and Larson, R. G. (2000). Excluded volume effects on the birefringence and stress of dilute polymer solutions in extensional flow. *Rheol. Acta*, 39:419–427.

[126] Li, L., Larson, R. G., and Shridhar, T. (2000). Brownian dynamics simulations of dilute polystyrene solutions. *J. Rheol.*, 44:291–322.

[127] Lifshitz, I. M., Grosberg, A. Y., and Khokhlov, A. R. (1978). Some problems of statistical physics of polymer-chains with volume interaction. *Rev. Mod. Phys.*, 50(3):683–713.

[128] Liu, B. and Dünweg, B. (2003). Translational diffusion of polymer chains with excluded volume and hydrodynamic interactions by Brownian dynamics simulation. *J. Chem. Phys.*, 118(17):8061–8072.

[129] Liu, S., Ashok, B., and Muthukumar, M. (2004). Brownian dynamics simulations of bead-rod-chain in simple shear flow and elongational flow. *Polymer*, 45:1383–1389.

[130] Liu, T. W. (1989). Flexible polymer-chain dynamics and rheological properties in steady flows. *J. Chem. Phys.*, 90(10):5826–5842.

[131] Lyulin, A. V., Dünweg, B., Borisov, O. V., and Darinskii, A. A. (1999). Computer simulation studies of a single polyelectrolyte chain in poor solvent. *Macromolecules*, 32(10):3264–3278.

[132] Magda, J. J., Larson, R. G., and Mackay, M. E. (1988). Deformation-dependent hydrodynamic interaction in flows of dilute polymer solutions. *J. Chem. Phys.*, 89(4):2504–2513.

[133] Malevanets, A. and Kapral, R. (1999). Mesoscopic model for solvent dynamics. *J. Chem. Phys.*, 110(17):8605 – 13.

[134] Marko, J. F. and Siggia, E. D. (1995). Stretching DNA. *Macromolecules*, 28:8759–8770.

[135] Marsh, C. A., Backx, G., and Ernst, M. H. (1997). Fokker-Planck-Boltzmann equation for dissipative particle dynamics. *Europhys. Lett.*, 38(6):411 – 15.

[136] Martinez, D. O., Matthaeus, W. H., Chen, S., and Montgomery, D. C. (1994). Comparison of spectral method and lattice Boltzmann simulations of two-dimensional hydrodynamics. *Phys. Fluids*, 6(3):1285 – 98.

[137] McPhie, M. G., Daivis, P. J., and Snook, I. K. (2006). Viscosity of a binary mixture: Approach to the hydrodynamic limit. *Phys. Rev. E*, 74(3):31201 – 31213.

[138] Menasveta, M. J. and Hoagland, D. A. (1991). Light-scattering from dilute poly(styrene) solutions in uniaxial elongational flow. *Macromolecules*, 24(11):3427–3433.

[139] Menasveta, M. J. and Hoagland, D. A. (1992). Molecular-weight dependence of the critical strain rate for flexible polymer-solutions in elongational flow. *Macromolecules*, 25(25):7060–7062.

[140] Miranker, A. D. and Dobson, C. M. (1996). Collapse and cooperativity in protein folding. *Curr. Opin. Struct. Biol.*, 6(1):31–42.

[141] Miyazawa, S. and Jernigan, R. L. (1985). Estimation of effective interresidue contact energies from protein crystal-structures - quasi-chemical approximation. *Macromolecules*, 18(3):534–552.

[142] Montesi, A., Morse, D. C., and Pasquali, M. (2005). Brownian dynamics algorithm for bead-rod semiflexible chain with anisotropic friction. *J. Chem. Phys.*, 122(8).

[143] Nakata, M. and Nakagawa, T. (1999). Kinetics of coil-globule transition of poly(methyl methacrylate) in isoamyl acetate. *J. Chem. Phys.*, 110(5):2703 – 10.

[144] Narh, K. A., Odell, J. A., and Keller, A. (1992). Temperature-dependence of the conformational relaxation-time of polymer-molecules in elongational flow - Invariance of the molecular-weight exponent. *J. Polym. Sci., Polym. Phys.*, 30(4):335–340.

[145] Navarro, S., Martinez, M. C. L., and de la Torre, J. G. (1995). Relaxation times in transient electric birefringence and electric-field light scattering of flexible polymer chains. *J. Chem. Phys.*, 103(17):7631–7639.

[146] Neelov, I. M., Adolf, D. B., Davies, G. R., Darinskii, A. A., Niemela, S., Skrifvars, M., and Sundholm, F. (2003). Computer simulations of stretching and collapse of polymer molecules in solution. *Macromol. Symp.*, 191:41–50.

[147] Neelov, I. M., Adolf, D. B., Lyulin, A. V., and Davies, G. R. (2002). Brownian dynamics simulation of linear polymers under elongational flow: Bead rod model with hydrodynamic interactions. *J. Chem. Phys.*, 117(8):4030–4041.

[148] Nishio, I., Sun, S. T., Swislow, G., and Tanaka, T. (1979). First observation of the coil-globule transition in a single polymer chain. *Nature*, 281(5728):208–209.

[149] Odell, J. A., Keller, A., and Miles, M. J. (1985). Assessment of molecular connectedness in semi-dilute polymer-solutions by elongational flow. *Polymer*, 26(8):1219–1226.

[150] Ohta, T., Oono, Y., and Freed, K. F. (1982). Static-coherent-scattering function for a single polymer-chain - Conformational space renormalization of polymers .5. *Phys. Rev. A*, 25(5):2801–2811.

[151] Ostrovsky, B. and Baryam, Y. (1997). Irreversible polymer collapse in 2 and 3 dimensions. *Europhys. Lett.*, 25(6):409–414.

[152] Öttinger, H. C. (1987). Translational diffusivity from the Zimm model. *J. Chem. Phys.*, 87(5):3156–3165.

[153] Öttinger, H. C. (1989). Renormalization-group calculation of excluded-volume effects on the viscometric functions of dilute polymer solutions. *Phys. Rev. A*, 40(5):2664–2671.

[154] Öttinger, H. C. (1994). Brownian dynamics of rigid polymer-chains with hydrodynamic interactions. *Phys. Rev. E*, 50(4):2696–2701.

[155] Öttinger, H. C. (1996). *Stochastic Processes in Polymeric Fluids.* Springer, Berlin.

[156] Pagonabarraga, I., Hagen, M. H. J., and Frenkel, D. (1998). Self-consistent dissipative particle dynamics algorithm. *Europhys. Lett.*, 42(4):377 – 82.

[157] Petera, D. and Muthukumar, M. (1999). Brownian dynamics simulation of bead-rod chains under shear with hydrodynamic interaction. *J. Chem. Phys.*, 111:7614–7623.

[158] Pham, T. T., Bajaj, M., and Prakash, J. R. (2008). Brownian dynamics simulation of polymer collapse in a poor solvent: Influence of implicit hydrodynamic interactions. *Soft Matter*, 4(6):1196–1207.

[159] Pierleoni, C. and Ryckaert, J.-P. (1992). Molecular dynamics investigation of dynamic scaling for dilute polymer solutions in good solvent conditions. *J. Chem. Phys.*, 96(11):8539 – 8551.

[160] Pitard, E. (1999). Influence of hydrodynamics on the dynamics of a homopolymer. *Eur. Phys. J. B*, 7(4):665–673.

[161] Pitard, E. and Orland, H. (1998). Dynamics of the swelling or collapse of a homopolymer. *Europhys. Lett.*, 41(4):467–472.

[162] Polson, J. M. and Moore, N. E. (2005). Simulation study of the coil-globule transition of a polymer in solvent. *J. Chem. Phys.*, 122(2):024905.

[163] Polson, J. M. and Zuckermann, M. J. (2000). Simulation of heteropolymer collapse with an explicit solvent in two dimensions. *J. Chem. Phys.*, 113(3):1283–1293.

[164] Polson, J. M. and Zuckermann, M. J. (2002). Simulation of short-chain polymer collapse with an explicit solvent. *J. Chem. Phys.*, 116(16):7244–7254.

[165] Prabhakar, R. and Prakash, J. R. (2004). Multiplicative separation of the influences of excluded volume, hydrodynamic interactions and finite extensibility on the rheological properties of dilute polymer solutions. *J. Non-Newtonian Fluid Mech.*, 116:163–182.

[166] Prabhakar, R., Prakash, J. R., and Sridhar, T. (2004). A successive fine-graining scheme for predicting the rheological properties of dilute polymer solutions. *J. Rheol.*, 48:1251–1278.

[167] Prakash, J. R. (2001). Rouse chains with excluded volume interactions: Linear viscoelasticity. *Macromolecules*, 34(10):3396–3411.

[168] Prakash, J. R. (2002). Rouse chains with excluded volume interactions in steady simple shear flow. *J. Rheol.*, 46(2):1353–1380.

[169] Qin, S. and Zhou, H.-X. (2009). Dissection of the high rate constant for the binding of a ribotoxin to the ribosome. *Proc. Natl. Acad. Sci. USA*, 106(17):6974–6979.

[170] Raos, G. and Allegra, G. (1996). A cluster of chains can be smaller than a single chain: New interpretation of kinetics of collapse experiments. *Macromolecules*, 29(26):8565–8567.

[171] Reddy, G. and Yethiraj, A. (2006). Implicit and explicit solvent models for the simulation of dilute polymer solutions. *Macromolecules*, 39(24):8536–8542.

[172] Rey, A., Freire, J. J., and Delatorre, J. G. (1991). Translational diffusion, relaxation-times, and quasi-elastic scattering of flexible chains with excluded volume and fluctuating hydrodynamic interactions - A Brownian dynamics study. *Macromolecules*, 24(16):4666–4672.

[173] Rotne, J. and Prager, S. (1969). Variational treatment of hydrodynamic interaction in polymers. *J. Chem. Phys.*, 50:4831–4837.

[174] Saintillan, D., Darve, E., and Shaqfeh, E. S. G. (2005). A smooth particle-mesh Ewald algorithm for Stokes suspension simulations: the sedimentation of fibers. *Macromolecules*, 17(3):33301 – 1.

[175] Sali, A., Shakhnovich, E., and Karplus, M. (1994). How does a protein fold? *Nature*, 369(6477):248–251.

[176] Schäfer, L. (1999). *Excluded Volume Effects in Polymer Solutions*. Springer-Verlag, Berlin.

[177] Schindler, T., Herrler, M., Marahiel, M. A., and Schmid, F. X. (1995). Extremely rapid protein-folding in the absence of intermediates. *Nature Struct. Biol.*, 2(8):663–673.

[178] Schlijper, A. G., Hoogerbrugge, P. J., and Manke, C. W. (1995). Computer simulation of dilute polymer solutions with the dissipative particle dynamics method. *J. Rheol.*, 39(3):567 –.

[179] Schroeder, C. M., Babcock, H. P., Shaqfeh, E. S. G., and Chu, S. (2003). Observation of polymer conformation hysteresis in extensional flow. *Science*, 301(5639):1515–1519.

[180] Schroeder, C. M., Shaqfeh, E. S. G., and Chu, S. (2004). Effect of hydrodynamic interactions on dna dynamics in extensional flow: Simulation and single molecule experiment. *Macromolecules*, 37(24):9242–9256.

[181] Sevick, E. M., Monson, P. A., and Ottino, J. M. (1988). Monte Carlo calculations of cluster statistics in continuum models of composite morphology. *J. Chem. Phys.*, 88(2):1198 – 1206.

[182] Shakhnovich, E. I. (1994). Proteins with selected sequences fold into unique native conformation. *Phys. Rev. Lett.*, 72(24):3907–3910.

[183] Shakhnovich, E. I., Farztdinov, G., Gutin, A. M., and Karplus, M. (1991). Protein folding bottlenecks: A Monte Carlo simulation. *Phys. Rev. Lett.*, 67.

[184] Shakhnovich, E. I. and Gutin, A. M. (1993a). Engineering of stable and fast-folding sequences of model proteins. *Proc. Natl. Acad. Sci. USA*, 90(15):7195–7199.

[185] Shakhnovich, E. I. and Gutin, A. M. (1993b). A new approach to the design of stable proteins. *Protein Engineering*, 6(8):793–800.

[186] Shaqfeh, E. S. G. (2005). The dynamics of single-molecule DNA in flow. *J. Non-Newtonian Fluid Mech.*, 130(1):1–28.

[187] Smith, W. and Rapaport, D. C. (1992). Molecular-dynamics simulation of linear-polymers in a solvent. *Mol. Simul.*, 9:25–39.

[188] Socci, N. D. and Onuchic, J. N. (1995). Kinetic and thermodynamic analysis of proteinlike heteropolymers - Monte-Carlo histogram technique. *J. Chem. Phys.*, 103(11):4732–4744.

[189] Sosnick, T. R., Mayne, L., Hiller, R., and Englander, S. W. (1994). The barriers in protein-folding. *Nature Struct. Biol.*, 1(3):149–156.

[190] Sosnick, T. R., Mayne, L., Hiller, R., and Englander, S. W. (1996). Molecular collapse: The rate-limiting step in two-state cytochrome c folding. *Proteins: Struct. Func. Genet.*, 24(4):413–426.

[191] Sridhar, T., Nguyen, D. A., Prabhakar, R., and Prakash, J. R. (2007). Rheological observation of glassy dynamics of dilute polymer solutions near the coil-stretch transition in elongational flows. *Phys. Rev. Lett.*, 98(16):167801.

[192] Succi, S. (2001). *The Lattice Boltzmann Equation for Fluid Dynamics and Beyond*. Oxford University, Oxford.

[193] Sunthar, P., Nguyen, D. A., Dubbelboer, R., Prakash, J. R., and Sridhar, T. (2005). Measurement and prediction of the elongational stress growth in a dilute solution of DNA molecules. *Macromolecules*, 38(24):10200–10209.

[194] Sunthar, P. and Prakash, J. R. (2005). Parameter free prediction of DNA conformations in elongational flow by successive fine graining. *Macromolecules*, 38:617–640.

[195] Sunthar, P. and Prakash, J. R. (2006). Dynamic scaling in dilute polymer solutions: The importance of dynamic correlations. *Europhys. Lett.*, 75(1):77–83.

[196] Taketomi, H., Ueda, Y., and Go, N. (1975). Studies on protein folding, unfolding and fluctuations by computer-simulation .1. Effect of specific amino-acid sequence represented by specific inter-unit interactions. *Int. J. Pept. Proteins Res.*, 7(6):445–459.

[197] Tanaka, G. and Mattice, W. L. (1995). Chain collapse by atomistic simulation. *Macromolecules*, 28(4):1049–1059.

[198] Tanner, R. I. (1975). Stresses in dilute-solutions of bead-nonlinear-spring macromolecules .2. Unsteady flows and approximate constitutive relations. *Trans. Soc. Rheol.*, 19(1):37–65.

[199] Thirumalai, D. (1994). Theoretical perspectives on in-vitro and in-vivo protein-folding. In *Statistical mechanics, protein structure, and protein substrate interactions*, volume 325, pages 115–134.

[200] Thirumalai, D. (1995). From minimal models to real proteins: Time scales for protein folding kinetics. *J. Phys. I*, 5(11):1457 – 67.

[201] Timoshenko, E. G. and Dawson, K. A. (1995). Equilibrium properties of polymers from the Langevin equation - Gaussian self-consistent approach. *Phys. Rev. E*, 51(1):492–498.

[202] Timoshenko, E. G., Kuznetsov, Y. A., and Dawson, K. A. (1995). Kinetics at the collapse transition Gaussian self-consistent approach. *J. Chem. Phys.*, 102(4):1816–1823.

[203] Timoshenko, E. G., Kuznetsov, Y. A., and Dawson, K. A. (1996). Gaussian self-consistent method for the kinetics of heteropolymers: A direction in studying the protein folding problem. *Phys. Rev. E*, 53(4):3886–3899.

[204] Timoshenko, E. G., Kuznetsov, Y. A., and Dawson, K. A. (1998). Conformational transitions of heteropolymers in dilute solutions. *Phys. Rev. E*, 57(6):6801–6814.

[205] Tsong, T. Y., Baldwin, R. L., and Elson, E. L. (1971). The sequential unfolding of ribonuclease A - Detection of a fast initial phase in kinetics of unfolding. *Proc. Natl. Acad. Sci. USA*, 68(11):2712–2715.

[206] Underhill, P. T. and Doyle, P. S. (2004). On the coarse-graining of polymers into bead-spring chains. *J. Non-Newtonian Fluid Mech.*, 122(1-3):3–31.

[207] Villeneuve, C., Guo, H., and Zuckermann, M. J. (1997). Relaxational dynamics of a random heteropolymer. *Macromolecules*, 30(10):3066–3074.

[208] Wang, Z., Yu, J., and Chu, B. (1992). Kinetic study of coil-to-globule transition. *Macromolecules*, 25(5):1618–1620.

[209] Warner, H. R. (1972). Kinetic-theory and rheology of dilute suspensions of finitely extendible dumbbells. *Ind. Eng. Chem. Fund.*, 11(3):379.

[210] Wetlaufer, D. B. (1973). Nucleation, rapid folding, and globular intrachain regions in proteins. *Proc. Natl. Acad. Sci. USA*, 70(3):697–701.

[211] White, S. H. and Jacobs, R. E. (1993). The evolution of proteins from random amino-acid-sequences .1. Evidence from the lengthwise distribution of amino-acids in modern protein sequences. *J. Mol. Evol.*, 36(1):79–95.

[212] Wiest, J. M., Wedgewood, L. E., and Bird, R. B. (1989). On coil-stretch transitions in dilute polymer-solutions. *J. Chem. Phys.*, 90(1):587–594.

[213] Yamakawa, H. (1971). *Modern Theory of Polymer Solutions.* Harper and Row, New York.

[214] Zhu, P. W. and Napper, D. H. (1997). The longer time collapse kinetics of interfacial poly(n-isopropylacrylamide) in water. *J. Chem. Phys.*, 106(15):6492 – 8.

[215] Zimm, B. H. (1956). Dynamics of polymer molecules in dilute solution: Viscoelasticity, flow birefringence and dielectric loss. *J. Chem. Phys.*, 24(2):269–281.

[216] Ziv, G., Thirumalai, D., and Haran, G. (2009). Collapse transition in proteins. *Phys. Chem. Chem. Phys.*, 11(1):83–93.

[217] Zwanzig, R., Szabo, A., and Bagchi, B. (1992). Levinthal's paradox. *Proc. Natl. Acad. Sci. USA*, 89(1):20–22.

[218] Zylka, W. and Öttinger, H. C. (1991). Calculation of various universal properties for dilute polymer solutions undergoing shear flow. *Macromolecules*, 24(2):484–494.

List of publications forming part of, and arising from the thesis

Journal articles

1. T. T. Pham, P. Sunthar and J. R. Prakash (2008), "An alternative to the bead-rod model: Bead-spring chains with successive fine graining", *J. Non-Newtonian Fluid Mech.*, 149 (1-3), pp. 9-19.

2. T. T. Pham, M. Bajaj and J. R. Prakash (2008), "Brownian dynamics simulation of polymer collapse in a poor solvent: Influence of implicit hydrodynamic interactions", *Soft Matter*, 4 (6), pp. 1196-1207.

3. T. T. Pham, U. D. Schiller, J. R. Prakash and B. Dünweg (March, 2009), "Implicit and explicit solvent models for the simulation of a single polymer chain in solution: Lattice Boltzmann vs Brownian dynamics", submitted to *J. Chem. Phys.* .

4. T. T. Pham, B. Dünweg and J. R. Prakash (May, 2009), " Collapse dynamics of copolymers in a poor solvent: Influence of hydrodynamic interactions and chain sequence", submitted to *Soft Matter*.

Conference proceedings

1. T. T. Pham, P. Sunthar and J. R. Prakash, "Comparison of Bead-Spring and Bead-Rod Models for Dilute Polymer Solutions: Validation of the Successive Fine Graining Method", *CHEMECA*, Auckland, New Zealand, 17–20 Sept., 2006.

2. T. T. Pham and J. R. Prakash, "Collapse dynamics of homo-polymers in a poor solvent: Influence of hydrodynamic interactions", *CHEMECA*, Melbourne, Australia, 23–26 Sept., 2007.

Presentations at other international conferences

1. T. T. Pham, B. Dünweg and J. R. Prakash, "Collapse dynamics of a homopolymer: Influence of hydrodynamic interactions and quench depth ", *Mainz Materials Simulation Days*, Mainz, Germany, 13–15 June, 2007.

2. T. T. Pham, B. Dünweg and J. R. Prakash, “Collapse dynamics of a homopolymer: Non-monotonous effect of hydrodynamic interactions at large quench depth”, *The 23th International Conference on Statistical Physics*, Genova, Italy, 9–13 July, 2007.

3. T. T. Pham, B. Dünweg and J. R. Prakash, “Collapse dynamics of homopolymers and copolymers in a poor solvent: Influence of hydrodynamic interactions, quench depth and chain sequence”, *Molecular Modelling*, Melbourne, Australia, 27–30 Nov., 2007.

4. T. T. Pham, U. D. Schiller, J. R. Prakash and B. B. Dünweg, “Implicit and explicit solvent models for the simulation of a single polymer chain in solution: Lattice Boltzmann vs Brownian dynamics”, *Seventh Liquid Matter Conference*, Lund, Sweden, 27 June – 1 July, 2008.